Croissance catalysée de nanofils de ZnSe avec boîtes quantiques de CdSe

Miryam Elouneg-Jamroz

UNIVERSITÉ DE GRENOBLE

THÈSE

Pour obtenir le grade de

DOCTEUR DE L'UNIVERSITÉ DE GRENOBLE

Spécialité : **Nanophysique**

Arrêté ministériel : 7 août 2006

Présentée par

Miryam ELOUNEG-JAMROZ

Thèse dirigée par **Serge TATARENKO**

préparée au sein de

L'Institut Néel

L'Institut Nanosciences et Cryogénie

Croissance Catalysée de Nanofils de ZnSe avec Boîtes Quantiques de CdSe

Thèse soutenue publiquement le **16 Octobre 2013**

devant le jury composé de :

Monsieur Henri Mariette

Directeur de recherche CNRS, Institut Néel de Grenoble, Président

Monsieur Michel Gendry

Directeur de recherche à l'École Centrale de Lyon, Rapporteur

Monsieur Victor Etgens

Professeur à l'Université de Versailles Saint-Quentin en Yveline, Rapporteur

Madame Chantal Fontaine

Directeur de recherche CNRS, LAAS de Toulouse, Examinateur

Monsieur Serge Tatarenko

Directeur de recherche CNRS, Institut Néel de Grenoble, Directeur

Monsieur Yong Zhang

Professeur, University of North Carolina in Charlotte, Invité

Acknowledgments

First and foremost I would like to thank Serge Tatarenko, Edith Bellet-Amalric and Henri Mariette for giving me the opportunity to work on the subject of ZnSe nanowires with CdSe quantum dots. It has been a very enriching experience.

Next I would like to thank the Jury for their critical review of the thesis and useful feedback.

I would like to additionally thank the following people for important and useful scientific discussions: Olivier Landré, Joël Cibert and Ivan-Christophe Robin.

The TEM data was the result of exceptionally dedicated work done especially by Martien den Hertog, and also by Catherine Bougerol. This thesis would have been much less rich without their crucial contribution.

For providing all the optical results, as part of their work but also often upon special requests, I would like to thank Samir Bounouar, Peter Stepanov, Adrien Delga and Claudius Morchutt, along with Kuntheak Kheng and Jean-Phillipe Poisat.

The following people were key in providing expert technical support for the growth experiments: Yann Genuist and Yoann Curé.

I would also like to acknowledge the immense support from and good times shared with the following people: O L., Binze, Steph M., Steph P., Los Tíos, Maela B., Robert K., Alex W., Sybilla R., Cécilia D., Megan C., Gabriel T., Champignon, Lionel G., Damien S., Daniel B., Colin H., Irina G., Vanessa E.-S., Calvin W., Sirona F., Aurélie P., Erin Y., Périne J., Claire L., Emmanuel D., Sandeep A., Nitin M., Prem K., Mom.

Finally a special thanks goes to *La Fondation Nanoscience* for providing financial support, for following the progress of the thesis and for providing help in making my transition to France as smooth as possible.

Table of Contents

Chapter 1

General Introduction

Contents

1.1 Motivation

We know that the subject of nanowire growth has been studied since Wagner and Ellis famously presented their gold catalysed Si whiskers in 1964 [1] and presented their vapour-liquid-solid (VLS) interpretation for the growth mechanism. From early on a lot of hope was placed on this type of bottom-up assembly of nanowires, in the prospect that one day such self-assembly would be integral in the manufacturing of ultra-small electronics. Indeed the concept of nanowire growth is nowadays exploited with the most common semiconductors, including Si[2], Ge[3], GaN[4], GaAs[5], InAs[6], InP[7], ZnSe[8], ZnTe[9], all of which have demonstrated the possibility of yielding perfect crystalline quality in nanowire form. Yet, nanowires until today have not made their grand entrance into any marketable sector, and remain objects studied in laboratory. Controlling where they grow and how they grow are still areas of intense research, and sometimes debate.

It is not surprising that ZnSe nanowires are studied primarly for their optical properties [10, 11, 12, 13, 14, 15]. ZnSe is an important semiconductor with a wide bandgap of 2.67 eV at room temperature. It has been investigated for short wavelength optolelectronic devices, like for instance blue laser diodes [16], light emitting diodes [17], blue-ultraviolet photodetectors [18] or white light emitting diodes with low consumption [19].

ZnSe has been used as a large bandgap barrier for confining carriers in the smaller bandgap material CdSe (1.7 eV) in the quantum well geometry [20]. The large lattice mismatch between ZnSe and CdSe has also been exploited to grow CdSe Stranski-Krastanov (SK) quantum dots on ZnSe surfaces, with good photoluminescent properties. It is a fact that the group "Nano-physique et Semiconducteurs (NPSC)", where this thesis was conducted, has gathered extensive knowledge on the latter subject, including the development of precise growth procedures by molecular beam epitaxy [21], the study of strain relaxation [22] and investigation of the involved quantum optics [23].

It was a natural step for our group to try to grow ZnSe/CdSe heterostructures in nanowire form. More precisely it was sought to grow ZnSe nanowires with a short CdSe heterostructure to act as a photo-emitting quantum dot. This geometry promised to offer two big advantages over the SK quantum dots. Firstly, strain due to lattice mismatch could relax, to a certain extent, through sidewall elastic deformation, which would allow more freedom in choosing the quantum dot height for the purpose of tuning the emission wavelength. Secondly, the nanowire geometry eliminates the problem of the wetting layer, which in SK quantum dots represents an efficient thermal escape route for the confined carriers. These advantages are also offered by colloidal nanocrystals, but they usually suffer from photobleaching [24] due to a large unpacivated surface. Compared to nanocrystals, quantum dots in nanowires have an unpacivated surface limited to that exposed at the nanowire sidewalls. Furthermore, epitaxially grown nanowires can be probed directly on their substrates, and their density and location can be controlled by patterning the catalyst.

In 2007 the first study in our team of ZnSe nanowires grown with a gold catalyst demonstrated that their diameter was quite small, between 5 and 30 nm [25]. This meant that the nanowires were small enough the confine the CdSe exciton of ~11 nm Bohr diameter, at least in the radial direction. Indeed in 2008, the team reported the single photon emission of CdSe quantum dots in ZnSe nanowires up to 220 K [26]. This was an important proof of concept. Nevertheless, because the nanowires had been grown on an amorphous SiO_2 surface, they grew in the form of a thick carpet and in random

orientations. This made it difficult to isolate individual nanowires for optical observations, and the study couldn't be further complemented with a TEM observation of the CdSe segment. In order to try and obtain oriented nanowires, a new approach was taken, that of conducting the homoepitaxy of ZnSe nanowires on a crystalline ZnSe surface. This is where this thesis began.

This thesis presents a study of the MBE growth of gold-catalysed ZnSe nanowires on a ZnSe surface. Since the main motivation is to use ZnSe nanowires as a vehicle for CdSe quantum dots, this thesis also presents the structural and optical observations of CdSe grown as short heterostructure segments in the ZnSe nanowires. This concept is sketched in figure 1.1.

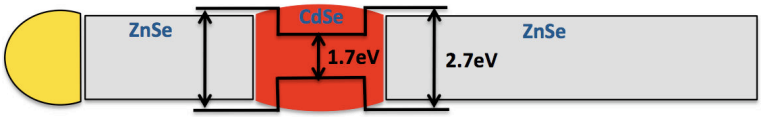

Figure 1.1: ZnSe nanowire containing a CdSe quantum dot as a heterostructure segment. Bandgap energies are for room temperature condition.

In Chapter 2 we present the experimental tools used during this thesis. Chapter 3 goes over the synthesis of the ZnSe surface and over the preparation of the gold catalyst. Chapter 4 presents a systematic study of ZnSe nanowire growth under selected growth conditions. In chapter 5 we'll discuss observations of the catalyst and also of ZnSe/CdSe heterojunctions in the nanowires for hints of their growth mechanism. Finally chapter 6 presents an optical study of short CdSe heterostructure quantum dots, but also their observation by TEM giving their crystalline structure and, to some extent, their chemical composition. Finally chapter 7 gives an outlook of where future studies of these structures might be headed.

1.2 ZnSe Nanowire Growth: State of the Art

The group of N. Wang at the Hong Kong University of Science and Technology is probably the group with the most sustained research in the field of ZnSe nanowire growth by MBE. Their reported work extends from 2003 until 2008 [27, 8, 28, 29], and their results pertain to nanowire synthesis, study of crystallography and development of a growth model. The group of Wang focused solely on growth performed directly on crystalline surface, either GaP or GaAs. Some examples are shown in figure 1.2. All their growth are performed with a ZnSe compound cell.

One of the main conclusions obtained by Wang's group was that ZnSe nanowires could grow epitaxially on GaP or on GaAs, along ⟨111⟩, ⟨112⟩ and ⟨110⟩ directions on the same substrate (see figure 1.2). Many substrate orientations were tested: (001), (111) and (011). Ultrathin nanowires with a diameter smaller than 10 nm grew mainly along the ⟨110⟩ direction on all substrates, and for that reason they grew vertically on (011) substrates. Nanowires with diameters <20 nm contained very few defects. Thicker nanowires with diameters >20 nm preferred growing along the ⟨111⟩ directions. These thicker nanowires always had stacking faults. Nanowires with diameters 10–20 nm grew along either ⟨110⟩ or ⟨112⟩ directions.

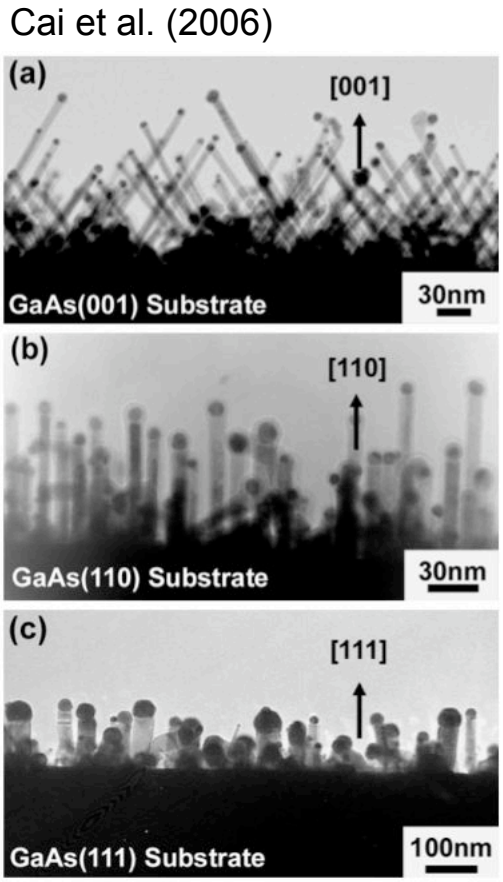

Figure 1.2: ZnSe nanowires grown by Cai et al. [28]. Thin nanowires (d>10 nm) prefer the ⟨110⟩ growth orientation while thick nanowires (d>20 nm) prefer the ⟨111⟩ orientation. By choosing the substrate appropriately vertical nanowires were produced.

To explain these growth orientations, Cai et al. [29] postulated that the nanowires will tend to grow in the direction that minimizes their total energy. Nanowires are considered as columns with an interface with the catalyst and side facets corresponding to a hexagonal nanowire cross section (see figure 1.3c). Since the bulk energy is independent of the crystal structure and only dependent on the volume, and since nanowires exhibit a high surface to volume ratio, only the surface and interface energies need to be considered to deduce their preferred orientation. Cai also observes that from the least energetic to the most, the facets rank as follows: (111)B < (100) < (311)< (111)A < (110).

The ⟨111⟩ direction is preferential for growth when the nanowires are short and therefore when most of the surface area is at the catalyst interface. When the nanowire grow taller and the sidewalls become the dominant surface, it becomes advantageous for the nanowires to grow in the ⟨110⟩ direction, in order to expose mostly (111) surfaces at the side walls. Wether or not the nanowires will actually change their growth direction to minimize their surface energy at a critical height will depend, according to Cai, on the thickness L_c of the nearly-molten ZnSe region sandwiched between the ZnSe nanowire crystal and the liquid catalyst. This region is where the atoms in the crystal can rearrange easily to change growth direction and therefore it is argued that this is the only section where energy needs to be minimized. The thickness of the nearly-molten region is proportional to temperature. Therefore this explains why at high temperature nanowires will rearrange to grow in a ⟨110⟩ direction, but remain in a ⟨111⟩ direction at low temperature.

Colli et al. [30] from the University of Cambridge also report the MBE growth of ZnSe nanowires but with separate effusion cells of Zn and Se, with a Se-rich constituent flux. Since Colli conducted the growths on an amorphous SiO_2 surface, the nanowires are randomly oriented and the results are difficult to compare to those of Wang's group. The growth observations are actually closely related to those obtained in our team by Aichele et al. [25]. Colli reports that straight nanowires, with a small diameter around 10 nm grow at T> 400°C, whereas tapered nanowires grow at T~ 300°C. Aichele additionally reports that nanowires will be tapered if grown under Zn-rich constituent flux (see figure 1.4).

Here is a concise summary of ZnSe nanowires grown by MBE based on Refs [27, 29, 8, 28, 30, 25, 31]:

i)Except for one case where Fe is used as catalyst [31], Au is always the catalyst used for the MBE growth of ZnSe nanowires. The thickness of Au used varies from 0.3 to 4.8 nm. An annealing procedure to produce Au nanoparticles is not always reported. The range of Au particle sizes and related nanowires diameters is from 9 to 80 nm, with the large majority between 10 and 30 nm.

ii) Growth on SiO_2 surface produces randomely oriented nanowires, whereas growth on deoxydized substrates including GaAs and GaP encourages oriented nanowire growth. Furthermore it is possible to produce vertical nanowires by choosing a substrate orientation wisely - (111) for thick nanowires, (110) for thin ones.

iii) Growth under excess of Zn tends to create tapered nanowires. Under HRTEM investigation, these nanowires also show a polycrystalline nature, created by multiple occurrences of twin boundaries. The same happens when nanowires are grown at a lower temperature around 300°C. On the other hand growth under excess of Se and at higher temperatures > 400°C tends to create straight nanowires with uniform diameter throughout and equivalent to the diameter of the catalyst.

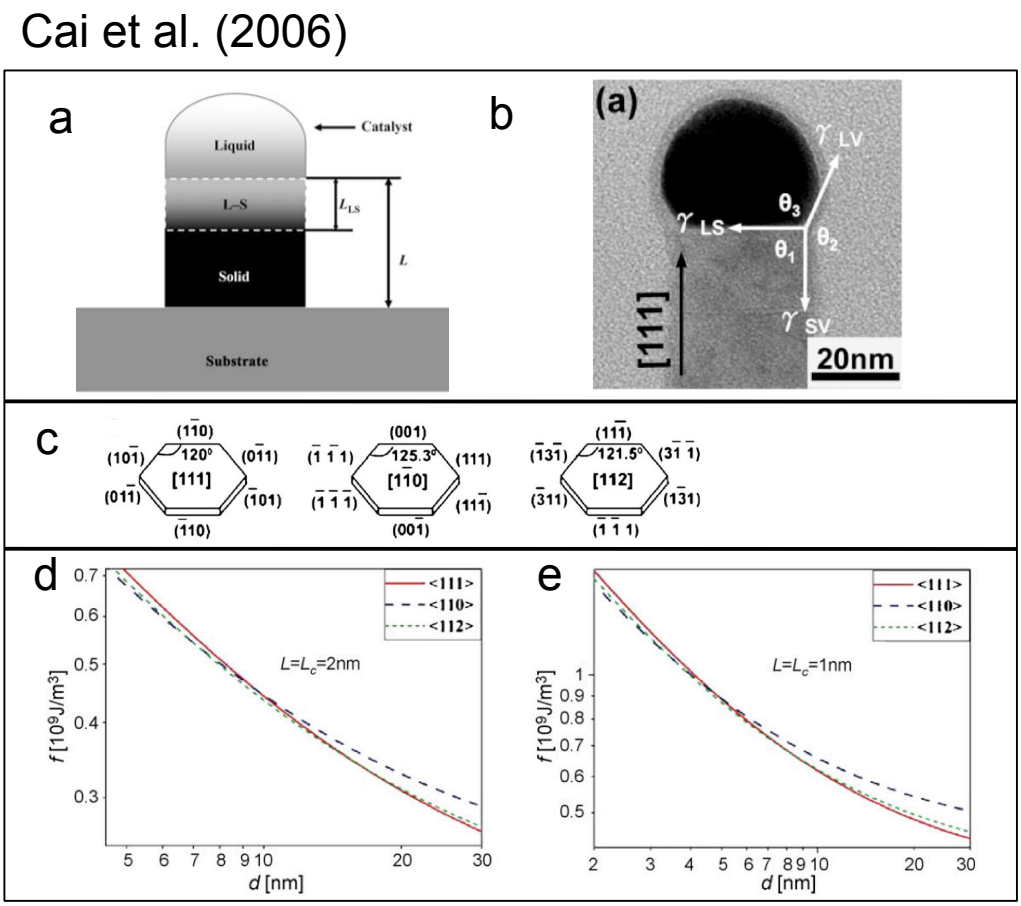

Figure 1.3: (a) Cai et al. [29] consider that the nanowire is only able to minimize its energy at a ZnSe semi-molten phase, sandwiched between the solid crystal, and the liquid catalyst and where the crystal is loose enough to be rearranged. (b) Surface energies can be deduced using the contact angles at the triple phase point (liquid (L), solid (S), vapor (V)) in the Young-Dupre relationship $\frac{\gamma_{LV}}{\sin\theta_1} = \frac{\gamma_{LS}}{\sin\theta_2} = \frac{\gamma_{SV}}{\sin\theta 1}$. (c) Hexagonal shape approximation of differently oriented nanowire cross-sections showing orientation of side facets. (d)-(e) Nanowire total surface and interface energy (f) vs. nanowire diameter at the semi-molten critical lengths (d) L_c = 2nm and (e) L_c = 1nm (L_c is equivalent to L_s in (a)) showing that small diameter nanowires favor the $\langle 110 \rangle$ growth orientation and larger diameter nanowires favor the $\langle 111 \rangle$ orientation.

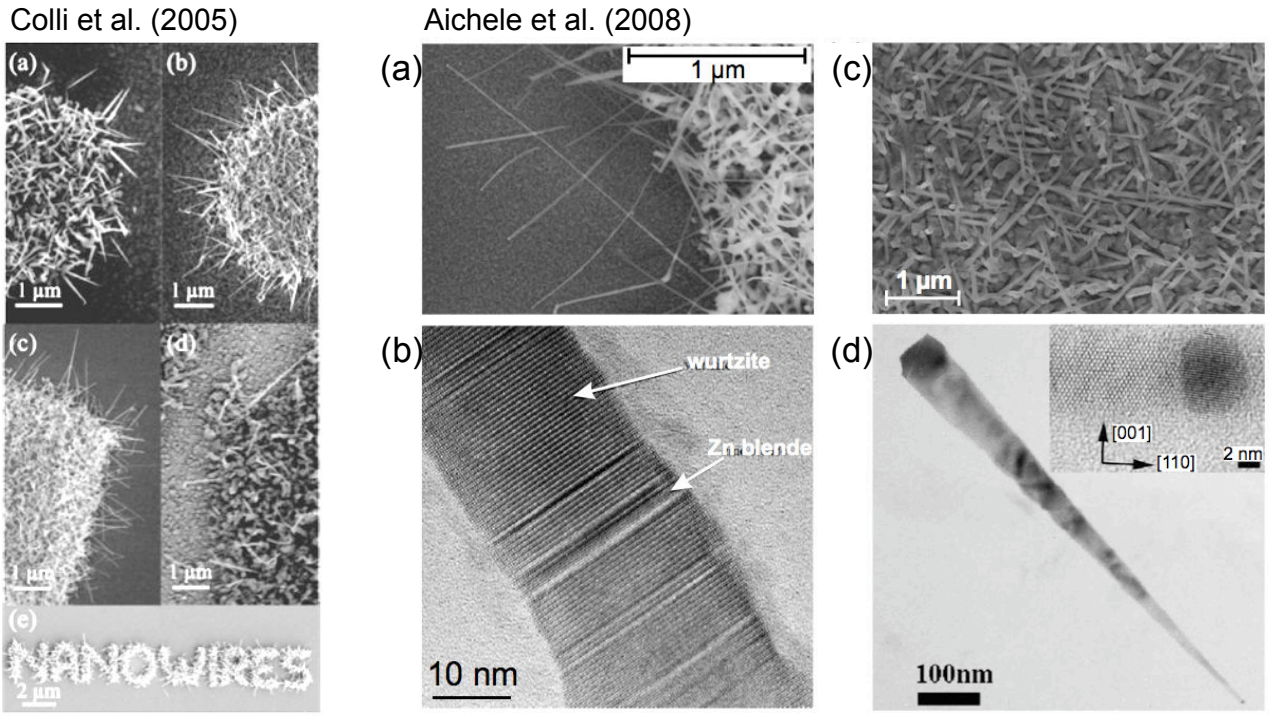

Figure 1.4: *Left* - ZnSe nanowires grown by Colli et al. [30]. Plan-view SEM image of ZnSe nanostructures showing the boundary region between the Au-pattern and the bare SiO_2/Si substrate. Growth tempreatures are (a)300°C, (b)400°C, (c)450°C, (d)550°C. (e) Demonstration of process selectivity at 450°C. *Right* - ZnSe nanowires grown by Aichele et al. [25] on SiO_2. (a) SEM image of an as-grown sample grown at 400°C under Se-rich condition. (b) TEM image showing a single nanowire from (a) with wurtzite and Zn-blende zones. (c) Nanoneedles (tapered nanowires) grown at 300°C under Se-rich condition. (b) TEM image of a needle in (c), the base containing disoriented defects while the tip is hexagonal without defects (inset).

iv) The crystal structure is usually cubic with a crystal orientation equivalent to the orientation of the nanowires when they bear an epitaxial relationship with the substrate. Sometimes ultrathin nanowires with diameters <10 nm have a hexagonal-c crystal.

v) The VSS mechanism is usually accepted, on the basis that growth of the ZnSe nanowires can occur well below the lowest eutectic temperature of AuZn, i.e. below 684°C.

1.3 II-VI Compounds for Photoluminescence

1.3.1 The Band Structure

II-VI semiconductors are systems of alloys where element II is either Mg, Zn, Cd, Pb or Hg, and element VI is either Se or Te. Element II has two valence electrons on its highest s-shell and element VI has six valence electrons, two on an s-shell and four on a p-shell. II and VI elements fill their valence shells by covalently bonding into sp3-type molecular orbitals. Element II is considered as the cation and element VI is the anion. Interaction through the formation of these orbitals arranges the alloy into a periodic crystal structure that is usually either zinc blende (ZB) or wurtzite (WZ) (see figure 1.5). For instance bulk ZnSe, CdTe and ZnTe adopt the ZB structure while bulk CdSe is WZ.

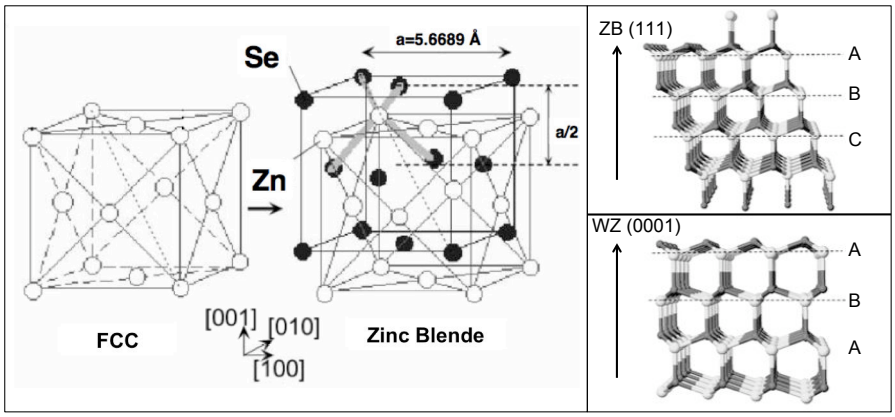

Figure 1.5: (a) The ZnSe zinc blende structure is built from two FCC structures, one for the Zn atoms and the other for the Se atoms, translated by one quarter of the main diagonal vector. (b) The zinc blende (ZB) and wurtzite (WZ) structures differ in their stacking sequence.

A picture drawn by linear combination of atomic orbitals (LCAO) can be used to understand the formation of energy bands, which give the II-VI materials their semiconducting properties (see figure 1.6).

In CdSe, the confining material in our study, we can think of the cadmium atom, the cation (II), as donating two electrons to the selenium atom, anion (VI) to complete the selenium symmetric p-shell. The selenium p-shell acts as the filled valence band of the alloy and the depleted anti-symmetric cadmium s-shell becomes the conduction band. As a general rule, changing the alloy anion or cation will therefore affect the energy level, respectively, of the valence or the conduction band. It follows from the above picture that the conduction band is twice degenerate and that its carriers (or electrons

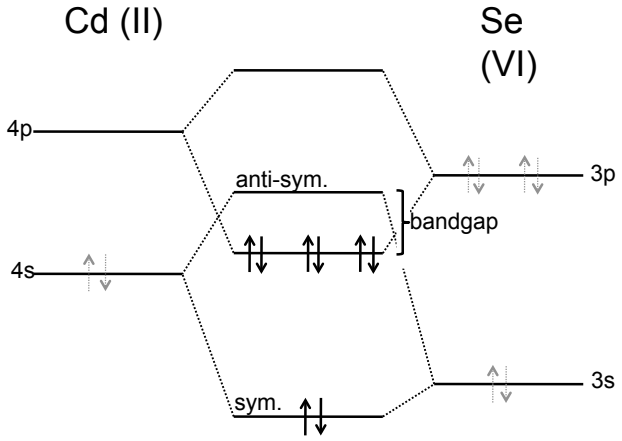

Figure 1.6: Linear combination of atomic orbitals (LCAO) of Cd and Se, forming the energy bands of CdSe.

thereafter) have a total angular momentum $J = 1/2$ due to the electronic spin (s); it also follows that carriers in the valence band (or holes thereafter) have a total angular $J = 3/2$ or $1/2$, due to the electronic spin and to the p-shell angular momentum $l = 1$ ($J_{max} = |l + s|$ and $J_{min} = |l - s|$). The spin-orbit interaction introduces a large energy splitting between the $J = 1/2$ and $J = 3/2$ bands (e.g., Δ_{so} ~420 meV in cubic CdSe at $k = 0$), and the latter band which lies at a higher energy becomes for all practical purposes the true valence band that we'll be referring to in this thesis work. The valence band is therefore four times degenerate at $k = 0$, separated into a doubly degenerate band of light holes with $J_z = \pm 1/2$, and the doubly degenerate band of heavy holes with $J_z = \pm 3/2$, distinguishing the light or heavy hole character of the carriers in the effective mass approximation of the crystal potential. For bulk materials, Schrodinger's equation in its usual form reads

$$-\frac{\hbar}{2m}\nabla^2\Psi(r) + V(r)\Psi(r) = E\Psi(r) \tag{1.1}$$

and can be approximated by

$$-\frac{\hbar}{2m*}\nabla^2\Psi(r) = E\Psi(r), \tag{1.2}$$

a simplified version that takes the form of the kinetic term with a modified, or effective, mass m^* of the carrier to approximate the potential energy of the lattice. In this case the wavefuntion solutions take the form of plane waves:

$$\Psi(r) \propto e^{ik.r}, \tag{1.3}$$

with energy solutions

$$E = \frac{\hbar^2|k|^2}{2m^*}. \tag{1.4}$$

In this approximation the dispersion relation is parabolic and fits the bands very well around $k = 0$.

The effective masses can be deduced from the experimental band diagram of the materials where Γ_6 is the electron conduction band and the valence band Γ_8 is split between light holes and heavy holes. The bandgap energy E_{gap} defines the minimum energy between the top of the valence band and the bottom of the conduction band, at $k = 0$.

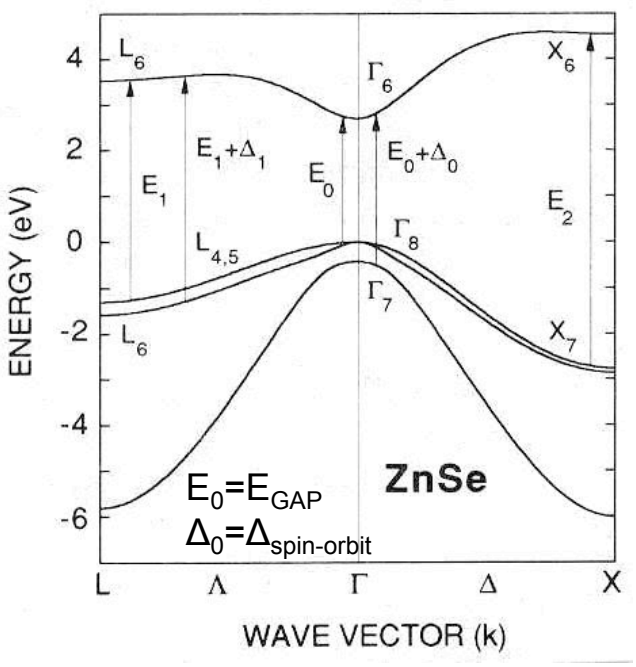

Figure 1.7: Typical energy band diagram for II-VI semiconductor materials centered at the Brioullin zone (Γ), i.e. $k = 0$. The bands are parabolic close to $k = 0$.

1.3.2 The 3D Exciton

Electrons and holes are created in pairs in a semiconductor when it is excited by absorption of photons of energies larger than the bandgap. These pairs then relax their excess energy via phonons, until they reach the lowest energy level on their respective bands, where they finally recombine. In semiconductors the lowest energy level is the exciton state, that is, an electron-hole pair bound together by their coulomb interaction much like the electron and the proton in the hydrogen atom. The exciton recombination creates a photon of energy $\hbar\omega = E_G - E_x$, where E_x is the exciton binding energy.

The exciton binding energy and its Bohr radius can be found by analogy with the hydrogen atom energy levels. The fundamental energy level E_0 and Bohr radius a_0 of the hydrogen atom are: $E_0 = \frac{m_e e^4}{8\epsilon_0^2 h^2} = -13.6$ eV and $a_0 = \epsilon_0 h^2 \pi m_e e^2 = 0.529$Å.

For the exciton (X) the effective masses m_h^* of the hole and m_e^* of the electron are of the same order of magnitude, and so we must take into account the reduced mass μ, such that $\frac{1}{\mu} = \frac{1}{m_h^*} + \frac{1}{m_e^*}$. The exciton energy is therefore:

$$E_x = \frac{\mu e^4}{8\epsilon_r \epsilon_0^2 h^2} \tag{1.5}$$

and the exciton Bohr radius is

$$a_0 = \epsilon_r \epsilon_0 h^2 \pi \mu e^2 \tag{1.6}$$

where ϵ_r is the dielectric constant of the semiconductor. In table 1.1 we summarize near bandgap energies including exciton energies for different semiconductors.

Table 1.1: Material properties common II-VI and III-V semiconductors.

Material	E_g at T=0K(eV)	a_0 (Å)	m_e (m_0)	m_{hh} (m_0)	E_x (eV)
ZnSe	2.83	5.668	0.60	0.21	-0.017
CdSe	1.85	6.078	0.45	0.13	-0.015
GaAs	1.52	5.654	0.063	0.51	-0.004
InAs	0.43	6.058	0.023	0.41	-0.002

We further develop the model of confinement in quantum dots and photoluminescence due to exciton recombination in chapter 6.

1.4 Stranski-Krastanov Quantum Dots

1.4.1 Stranski-Krastanov Growth Mode

A classical self-organization of materials into small dimensional objects is obtained through the Stranski-Krastanov (SK) growth mode. SK quantum dots have the advantage of being grown directly onto a semiconducting substrate, making them easy to implement into electrically driven devices.

The SK growth mode consists in epitaxial growth of a material that is lattice mismatched to the material of the substrate. Growth is performed until the strain built up in the deposited layer relaxes through the formation of three-dimensional islands. This happens upon reaching a critical thickness of the deposited layer. The appearance of additional surface on top of the islands can accomodate the lattice deformation elastically. The first few epitaxial layers deposited before the material relaxes into islands form the wetting layer, and the point when the wetting layer relaxes into three-dimensional islands is called the SK transition.

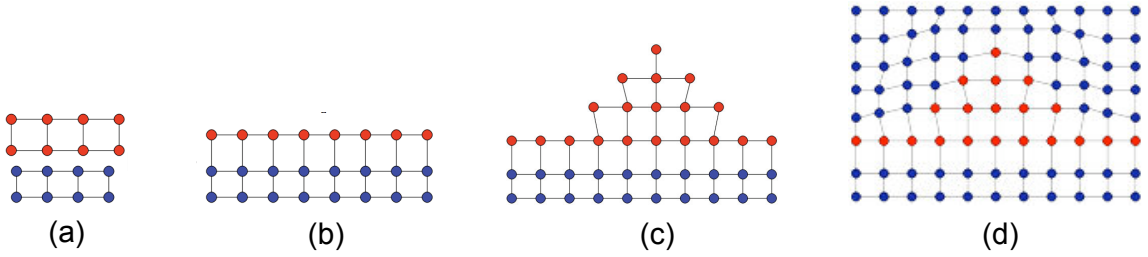

Figure 1.8: Stranski-Krastanov Growth Mode. (a) Choice of two latticed mismatched materials. (b) Initial deposited layer is strained. (c) Upon reaching a critical thickness the layer relaxes the strain energy by the formation of self-assembled islands QDs. (d) QDs are encapsulated for efficient 3D confinement.

SK quantum dots assemble into short truncated cones with a nanometer size height and a quasi-circular base with a diameter in the tens of nanometers. Their density on the substrate is between 10^9 and 10^{10} per cm^2. The confining dimension is the height, and because it is closely related to the critical thickness of the wetting layer, tuning the emission wavelength of SK quantum dots is limited.

Photoemission of SK quantum dots suffers the specific drawback that it quenches rapidly as the temperature is elevated. This is explained by the presence of the residual wetting layer of around 1 ML thickness that lies at the base of the QDs. The wetting layer comprises a continuum of 2D states (quantum well) that lie at an intermediate energy between the QDs and the matrix. As such it represents an efficient thermally activated escape route for carriers confined in the QDs. For this reason photoemission of SK QDs is often limited to temperatures below 200K [32, 33].

SK quantum dots show a random in-plane distribution and their individual location cannot be predetermined. They are also quite densely packed (several hundreds per μm^2), making individual QDs difficult to isolate for optical studies of single-photon emission, for instance. Regarding the issue of positioning, stacking quantum dots one on top of the other has been developed [34] by taking advantage of residual strain above each quantum dot to favor the positioning of another one in the next layer (see figure 1.9a). But it does not guarantee that the stacked quantum dots will all be of identical size and shape, which would be desirable say for optical coupling experiments.

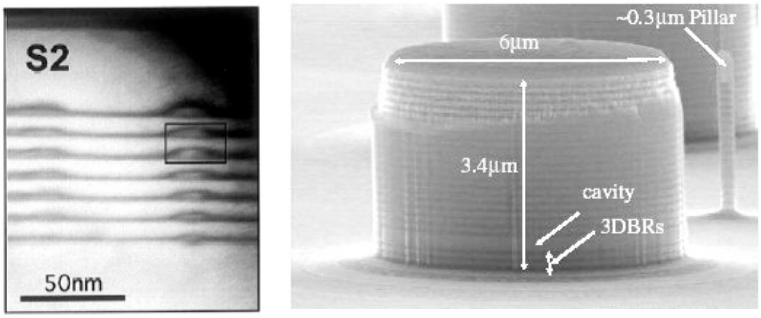

Figure 1.9: (a) TEM image of vertically self-alligned self-assembled InGaAs QDs. Taken from [34]. (b) Photonic cavity with InGaAs self-assembled QDs embedded between AlAs/GaAs Distributed Bragg Reflections (DBRs). Taken from [35].

Addressing a single quantum dot remains a non-trivial challenge. This can be done by using opaque masks that cover most of the QD sample except for isolated regions [36]; or by etching mesas (pillar shaped structures) post-growth in the substrate to isolate a few quantum dots at time [32]. Another way is to process optical microcavities on the quantum dot sample and study those quantum dots with emission wavelengths that couple best to the microcavity modes [37].

1.4.2 Elastic vs Plastic Relaxation in SK CdSe/ZnSe Heterostructures

When a 2D layer of CdSe is grown on ZnSe (001), it adopts the same crystal structure as ZnSe, i.e. zinc-blende, even if CdSe grown independently will have a wurtzite structure. Examining the lattice

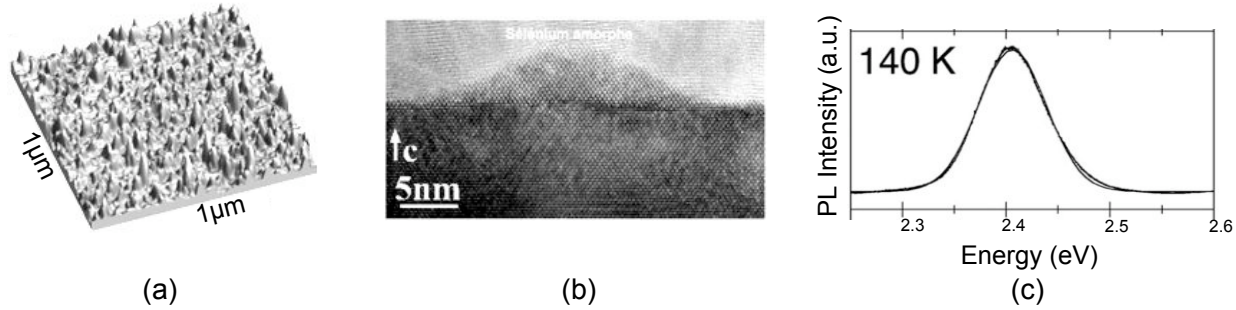

Figure 1.10: (a) AFM image of QD ensemble on substrate; density 10^{10} cm^{-2}. (b) HRTEM image of CdSe self-assembled (SK) QD. 2D to 3D transition obtained with a treatment under amorphous Se; with amorphous Se capping layer (from [38]).(c) Photoluminescence of QD ensemble. Modified from Ref. [23].

constants of CdSe and ZnSe reveals a lattice mismatch of ξ_0=6.35% calculated as

$$\xi_0 = \frac{a_{CdSe} - a_{ZnSe}}{a_{CdSe}}. \tag{1.7}$$

Under 2D growth, CdSe initially deforms elastically to adopts the ZnSe in-plane lattice parameter. Being of larger lattice constant, the CdSe layer is under compression in the plane and under extension in the growth direction. Elastic strain energy accumulates as the layer is grown thicker. This energy can dissipate through two relaxation mechanisms: elastic relaxation with surface formation of self-assembled islands, or plastic relaxation with the advent of misfit dislocations (MDs) at the interface of the two materials. The point at which the strain energy will start to relax and which relaxation venue will be favored can be modeled by taking into consideration the total energy of each state [39].

Tinjod et al. [22] define four states for a 2D epitaxial layer on a lattice mismatched substrate: (1) 2D-coherent, (2) SK-coherent with the formation of dislocation-free self-assembled islands, (3) 2D-MD which is a 2D layer with misfit dislocations, and (4) SK-MD with both self-assembled islands and misfit dislocations. Tinjod modeled the energy for each of these states of the epitaxial layer as a function of layer thickness, taking into account the layer surface energy, the elastic strain energy and the misfit dislocation energy. For states (2) and (4) the model accounts for the energy reduction in accommodating the layer's strain through the formation of the partly relaxed self-assembled islands and also the energy cost of creating the sides facets (additional surface) of the islands; for states (3) and (4) the model adjusts the periodicity of a square grid of MDs to minimize the total energy by also taking into account all elastic energy reduction from the related lowering of the lattice mismatch.

Figure 1.11a shows that for an epitaxial layer of CdSe on ZnSe, the 2D-coherent and the 2D-MD states will have identical energies until 5.2 monoloyers (ML), or 1.6nm, when the 2D-MD state becomes clearly more energetically favorable. The SK transition is unfavorable for all layer thicknesses. But according to the model an SK-coherent state can be favored if the surface energy is lowered, as can be seen in figure 1.11b. In practice it was achieved by capping exactly 3ML (0.91nm) of CdSe with amorphous selenium below room temperature followed by sublimation of the cap at 250° [21].

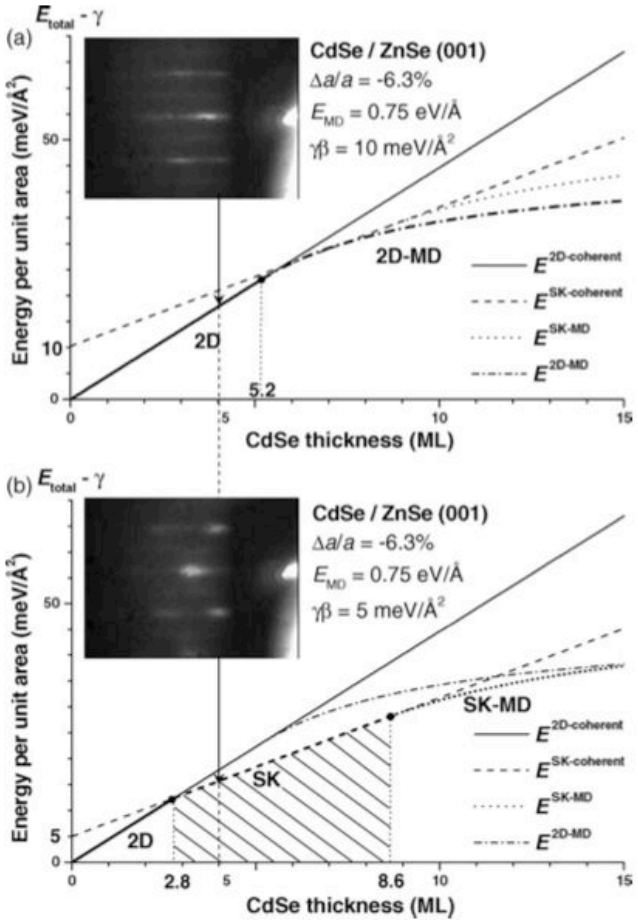

Figure 1.11: CdSe energy when grown on ZnSe (001). (a) 2D coherent growth occurs until 5.2ML at which point plastic relaxation is favored over the SK transition. (b) Sublimation of amorphous Se cap layer diminishes the surface energy. The SK-coherent transition is energetically favored from 2.8ML. Taken from Ref. [22].

But at 2.5 ML of CdSe, the same process would only lead to the appearance of strong undulations.

This illustrates the difficulty of forming CdSe SK quantum dots on ZnSe. The same is also true for the system of CdTe on ZnTe. It tells us that these systems don't tolerate strain easily and favor plastic relaxation. This is in part due to a high surface energy on the (001) surface. In part it is because they are relatively more malleable with a low value of the Young modulus E, compared with other systems in which the SK transition occurs spontaneously under vacuum. This is the case for instance of InAs/GaAs where the SK transition spontaneously occurs under vacuum at a critical thickness of 1.7 to 1.8 ML of InAs on GaAs [40, 41].

1.5 Elastic vs Plastic Relaxation in ZnSe/CdSe/ZnSe QD-in-NW

So how much is a plastic relaxation mechanism going to hinder the crystalline quality of a heterostructure in a nanowire? In contrast to an infinite 2D system, the strain accumulated at the heterostructure in a nanowire can relax through a deformation of the crystal at the nanowire sidewalls.

Glas [42] investigated the case where a lattice mismatched heterostructure with misfit ξ_0 is grown on top of a cylindrical nanowire, with a heterostructure of larger lattice constant. The nanowire radius is r_0, the heterostructure layer has a height h, giving an aspect ratio between these variables of $\rho = \frac{h}{2r_0}$.

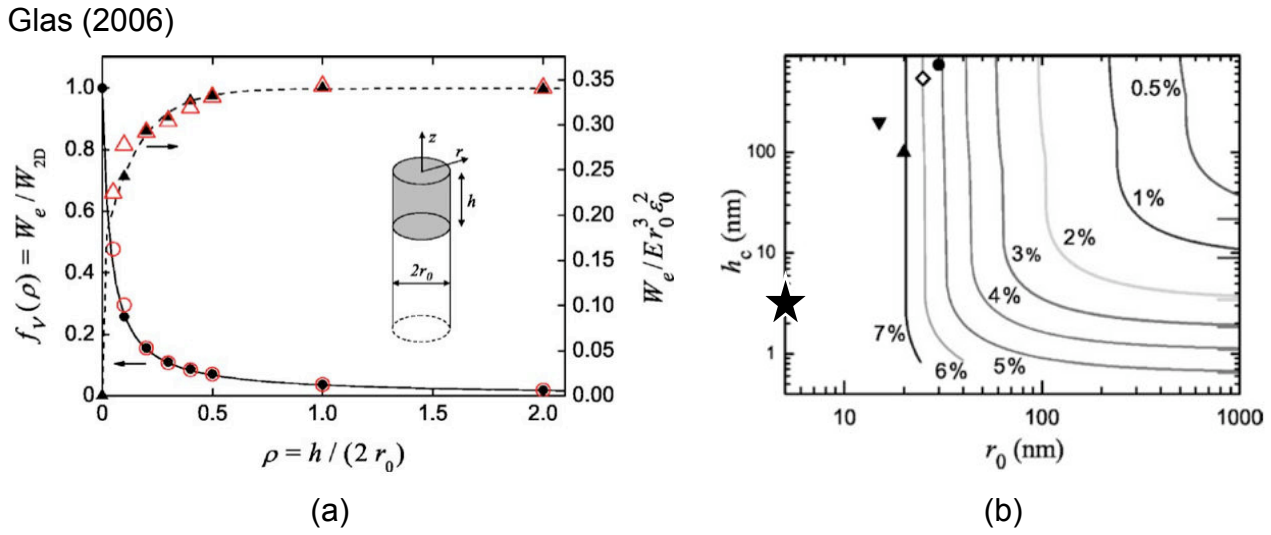

Figure 1.12: Nanowhisker with a misfitting top layer. (a) *Dashed line* Variation with the layer aspect ratio of the total elastic energy of the system. *Solid line* Ratio of the total elastic strain energy of a misfitting heterostructure in the nanowhisker over that of an equivalent volume of a 2D strained layer of CdSe coherently grown on a semi-infinite substrate. (b)Critical thickness of a misfitting layer grown on top of a nanowire as a function of wire radius for various values of misfit. For each curve, the region left and below the curve are the dislocation-free states; to the right and above each curve are the states containing dislocations. The case of the ZnSe nanowires with CdSe heterostructures that we will encounter in the present thesis are indicated by a $\star$ on the graph. They are located well inside the dislocation-free region for our misfit ξ_0=6.35%. Taken from Ref. [42].

Figure 1.12a graphs the variation with aspect ratio of the fraction $\frac{W_e}{W_{2D}}$, where W_e is the elastic energy stored in the layer of height h on the nanowire, and W_{2D} is the elastic energy stored in the same volume cut in a 2D strained layer coherently grown on a semi-infinite susbtrate with the same misfit. It is assumed that all strain is relaxed elastically.

In figure 1.12a we see that the total elastic strain energy in the nanowire heterostructure (solid line) increases until ρ=1, that is when the height of the layer becomes equivalent to the nanowire diameter $2r_0$. At that point the elastic energy is essentially saturated and no longer increases as the layer is grown thicker. In other words, the misfitting layer has almost completely relaxed through sidewall deformation. In comparison, the elastic energy in a 2D semi-infinite layer, We_{2D}, continues to accumulate with the misfitting layer height ($W_{2D} \propto h$).

In figure 1.12b Glas also considers the onset of plastic deformation from an energetic stand point. In the figure, the curves are essentially the boundaries between the states with (above and to the right of the curves) and without (below and to the left of the curves) misfit dislocations. Given that the ZnSe/CdSe system we will encounter in this thesis has a 6.35% misfit, r_0=5nm and a CdSe layer height of ~3nm, we can locate our state well within the dislocation-free region for our misfit. In fact this model predicts that for any nanowire radius up to r_0 ~25nm we can grow an arbitrary height CdSe layer without ever favoring plastic deformation. It follows, by symmetry, that an arbitrary height of CdSe can comprise a segment of inside a ZnSe nanowires without ever favoring plastic deformation (the curves in figure 1.12b are independant of the Young's modulus E in the material system).

1.6 Quantum Dot in a Nanowire: State of the Art

Several material combination have been used so far to grow nanowires with a photoemitting quantum dot. Here are a few examples.

Generally only one single quantum dot is inserted in the nanowires which allows µ-photoluminescence studies to probe single quantum dots. Tchernycheva et al. [43] grew two InAsP QDs of different lengths (~32 nm) in single InP nanowire, and these QDs show well resolvable emission (~7 meV separation).

Wojnar et al. [44] demonstrates high linear polarization, between 75% and 95%, of the emission of CdTe QDs in ZnTe nanowires. Tribu et al. [26] from our research team also reported a 90% linear polarization of light emission of CdSe QD in ZnSe nanowires. A strong linear polarization is expected to be caused by the large contrast of the dielectric constant between the nanowire material and the surrounding [45]. Nanowires are usually removed from the growth substrate and measured from the side because the spontaneous emission from thin NWs is strongly attenuated for photons polarized perpendicular to the NW axis when $\lambda \gg$diameter [46]. This strongly hinders the chances to probe the QD emission with top down measurements in free-standing, vertical, nanowires. Heinrich et al. [47] circumvented this drawback by growing a 100 nm diameter thick shell of AlGaAs/GaAs around a small 10 nm diameter GaAs emitter of $\lambda \sim 725$ nm. This strategy allowed to obtain efficient coupling of the emission with the photonic nanowire, and allowed top down photoluminescence measurements directly on the growth substrate.

Heinrich and also Dorenbos et al. [48] who grew InAsP in InP nanowires, both have demonstrated control in the nanowire positioning by growing them into arrays defined using e-beam lithography techniques. Heinrich chose a 10 µm square pitch positioning, not only to be able to isolate individual nanowires in µ-photoluminescence measurements, but also to demonstrate the absence of luminescence from the substrate areas between the nanowires that could originate from SK QDs. The concern for this parasitic luminescence was also brought up in other publications. Wojnar, for instance, made a point to demonstrate linear polarization of the QD emission in order to disambiguously attibute it as originating from a nanowire; Panev et al. [49] who grew InAs QDs in GaAs nanowires with a 2 µm interwire distance, would only show emission from nanowires which had been tranferred to another (non-emitting) substrate and seen by SEM to guarantee that the measurements originated from the nanowires and not from the original substrate.

Most of the studies cited above (and including the study of Borgstrom et al. [50], who grew GaAsP QDs in GaP NWs, show auto-correlation functions at low temperature with clear antibunching behaviors of their emitters. Tribu additionnally shows a temperature study of the antibunching and demonstrates single photon emission up to 220K. We summarize these results along with the general properties of the NW QD systems mentionned above in table 1.2. We also add the results from our publication from Bounouar et al.[51].

Table 1.2: NWs with QDs and their reported properties - from literature. X and XX stand for the exciton and the biexiton, τ stands for the lifetime; the second order autocorrelation value $g^{(2)}(0)$ is indicated for the raw measurement and also corrected for background light in brackets. All values are for low temperature measurements, unless otherwise indicated.

Year Ref.	NW QD	NW diameter QD height	X XX	FWHM$_X$ FWHM$_{XX}$	τ_X τ_{XX}	$g^{(2)}(0)$
2003 [49]	GaAs InGaAs	40-120 nm <50 nm	~1.41 eV –	200 µeV –	– –	–
2005 [50]	GaP GaAsP	20-31 nm 60-80 nm	1.86 eV X-2.9 meV	0.2-3.0 meV –	0.42–0.53 ns 0.28 ns	< 0.5
2007 [43]	InP InAsP	26-32 nm 27 nm	0.80-1.03 eV –	~0.120 meV –	– –	– –
2008 [26]	ZnSe CdSe	10 nm 10 nm	2.25-2.48 eV X-22 meV	– –	0.500 ns –	0.07(0.05), 4K 0.36(0.11), 220K
2010 [47]	GaAs AlGaAs	168-309 nm –	1.61-1.77 eV X-0.005 eV	0.1-0.5 meV –	290 ns –	0.46(0.28)
2010 [48]	InP InAsP	60-80 nm 10 nm	1.025 eV 1.023 eV	0.046 meV –	1.24-2.8 ns 0.34-0.87 ns	0.2(0.12)
2011 [44]	ZnTe CdTe	30-70 nm –	2.0-2.25 eV X-0.012 eV	2 meV –	– –	(0.29)
2012 [51]	ZnSe CdSe	10 nm 2.4-4 nm	XX+0.017 eV ~2.3 eV	– 0.9 meV	– 0.300 ns	0.09(0.05), 4K 0.48(0.22), 300K

Chapter 2

Experimental tools

Contents

2.1 Material Deposition Setup

2.1.1 Molecular Beam Epitaxy (MBE)

For our research we opted to work on GaAs substrates. We justified that choice because the lattice parameter of GaAs closely matches that of ZnSe (lattice mismatch of only 0.25%), and also because our laboratory has many years of experience in the growth of ZnSe on GaAs.

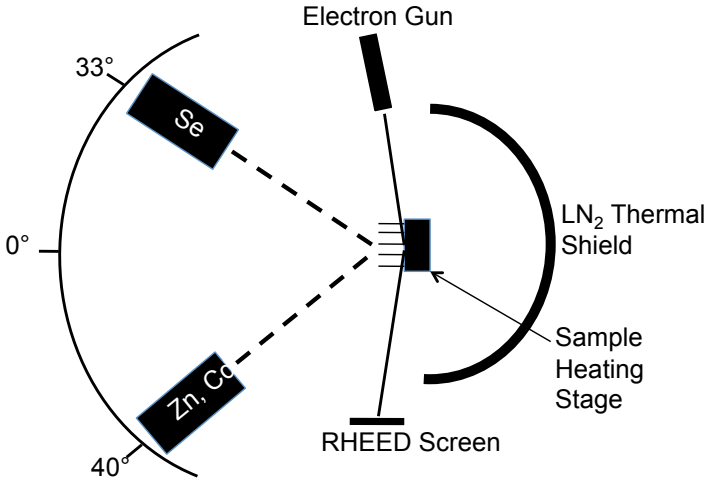

Figure 2.1: Schematic showing the II-VI MBE chamber configuration.

We performed material deposition in three separate UHV chambers. A Riber 32P MBE system is dedicated to the growth of II-VI materials (selenides and tellurides) as well as their doping (N, Al). It is equipped with a RHEED monitoring system (30 keV). The RHEED diffraction images, which appear on a fluorescent screen mounted at a viewport, are captured remotely by a CCD camera. An in-house developped RHEED program allows us to follow thin film growth rates by means of RHEED oscillation measurements. The quality and composition of the residual vacuum (in the 10^{-10} torr range) is followed by using a quadrupole mass spectrometer.

A second custom-made MECA2000 MBE system is dedicated to the growth of III-V materials including GaAs, and this chamber is equipped with a RHEED monitoring system, which allows us to observe the deoxidation of GaAs substrates and to monitor the growth of GaAs buffer layers.

Materials used in the II-VI chamber (Zn, Cd and Se) and in the III-V chamber (Ga and As) are of 6N grade purity.

A third regular chamber, without cooling shields, was used for Au deposition from an effusion cell.

All three chambers are interconnected by UHV transfer modules, which allowed us to perform all the growth steps without ever risking oxidation of the samples. Samples were mounted on molybdenum sample-holders (called moliblocs) by using molten indium. The low temperatures used for our MBE growths (280°C to 640°C) make it difficult to use a pyrometer for determination of sample temperatures. Therefore, the sample temperatures were measured by a thermocouple in direct contact with the molibloc.

In the II-VI chamber molecular beam fluxes were measured carefully before and after growths by using an ion gauge which we positioned at the sample location for readings. The fluxes were therefore measured in beam equivalent pressure, or BPR. We took care to always use the same flux reading procedure in order to obtain reproducible flux measurements.

The sketch in figure **??** shows the setup of the II-VI MBE chamber, noting specifically the angles of the effusion cells with respect to the sample normal for the elements that we deposited in our studies, i.e. Zn, Se and Cd. Because the effusion cells are tilted with respect to the sample normal, the nanowires can shadow the flux beams. This explains the importance of rotating the sample holder during the growth of the nanowires.

2.1.2 Reflection High Energy Electron Diffraction (RHEED)

RHEED is a powerful tool for surface characterization. Because a high energy electron beam is used, this characterization technique can be used in the UHV environment of the MBE chamber, but it cannot be used in other surface deposition setups like PVD or CVD. When using RHEED a monoenergetic electron beam at 30 keV is reflected at a grazing incidence (typically < 1°) from the substrate or epilayer structures (islands or nanowires) onto a fluorescent screen. At 30 keV ,the electron wavelength is below 0.1 Åand therefore it can resolve the ZnSe crystalline lattice (interatomic distances ~ 2 Å). The glancing incidence used in RHEED limits the penetration of the beam electrons to the top few monolayers of the surface under investigation. The electron beam images the reciprocal lattice of the substrate surface. A smooth crystalline surface is imaged as rods perpendicular to the surface; 3D structures lying on the substrate surface and having a finite height and finite width will be imaged as dots.

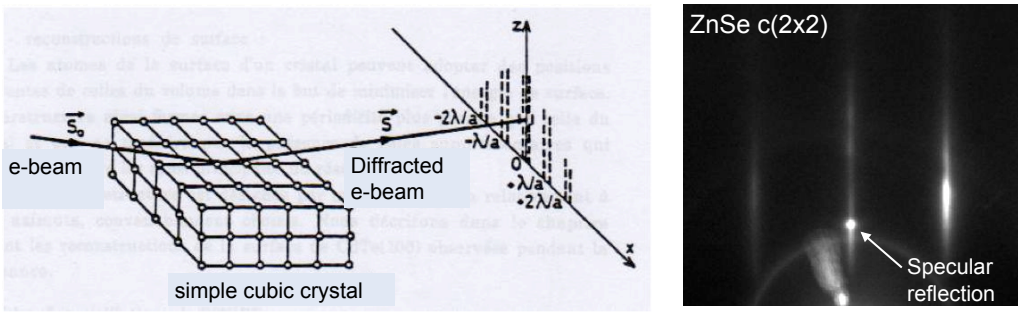

Figure 2.2: (a) Schematic illustrating the principle of RHEED diffraction. (b) RHEED showing the c(2x2) ZnSe surface.

For our measurements, we used a CCD camera to film the RHEED fluorescent screen and also to take picture snapshots.

In section 3.2.2 we use RHEED oscillations (time intensity variation of the surface specular reflection of the electron beam) to monitor ZnSe surface growth rates. The principle is simple and is illustrated in figure 2.3. The surface crystal grows one monolayer at a time and it is smoothest when a monolayer is completed. As an additional monolayer is grown, the appearance of a large number

of small monolayer terraces cause an increase of the surface roughness and decrease the specular reflection intensity. When the monolayer is completed upon the merger of new terraces, the specular reflection returns to its maximum intensity. Thus the time separating two maxima of the specular reflection corresponds to the growth of one complete monolayer.

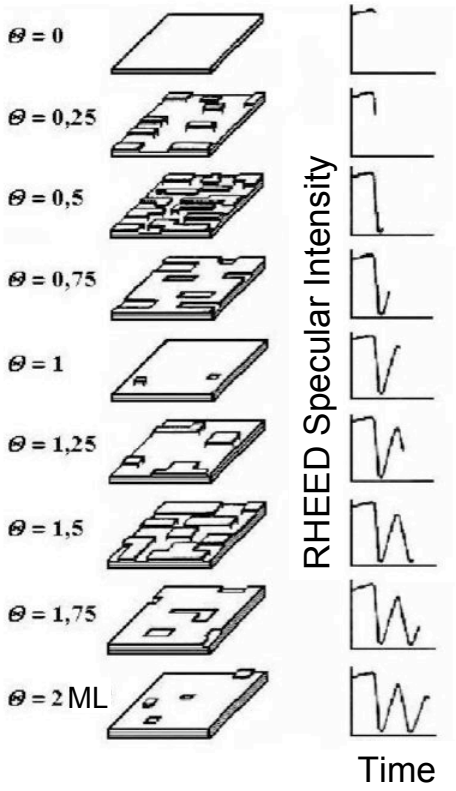

Figure 2.3: Schematic illustrating the principle of RHEED oscillations for the measurement of 2D crystal growth.

In section 3.3 and 5.2.5 we compare the separation distance between 1st order diffraction features from gold nanoparticles and 1st order diffraction features from the ZnSe surface in a direction parallel to the surface to find the lattice parameter of gold (the distance seperating 1st order features is proportional to the reciprocal of the lattice constant, following Bragg's law of diffraction.)

2.2 Scanning Electron Microscopy (SEM)

The SEM is a microscopy device that allowed us to rapidly image our samples with nanowires and nanoparticles. Investigation of SEM images of nanowires were essential to a large number of studies conducted in this thesis, and especially the ones presented in chapters 3 and 4. Most of the SEM images were produced at MINATEC on a Zeiss Ultra 55 SEM. The theoretical resolution of this SEM is < 1.5 nm, at the accelerating voltage 5-10 kV which we used to produce our images.

Because our nanowire diameters are typically ~10 nm, optical microscopy is not an available option because it is fundamentally limited to a resolution around 200 nm. We can reach a better

resolution when accelerating electrons at high voltages to obtain lower probing wavelengths (~0.01 nm).

SEM topographical imaging is conducted as follows The high energy focused electron beam is scanned over the sample. Secondary electrons produced at each scanned location are collected to produce an image. The secondary electrons are produced as the electron beam ionizes the surfaces by transferring kinetic energy to conduction electrons. These secondary electrons have a very low energy (~50 eV), and therefore only those electrons produced sufficiently close to the surfaces (within a depth of ~10 nm) can be detected before being reabsorbed. As the focal point of the e-beam scan a sample surface, any change in roughness is efficiently accompanied by a change in the number of secondary electrons produced, and therefore a very good likeness of the topography can be rendered. When imaging with secondary, electrons the contrast is mostly linked to topography, but it can also translate a chemical contrast in the case of large changes in atomic number (like for instance in ZnSe nanowires, with Z_{Zn}=30 and Z_{Se}=34, appear with a different contrast than the gold catalyst, with Z_{Au}=79).

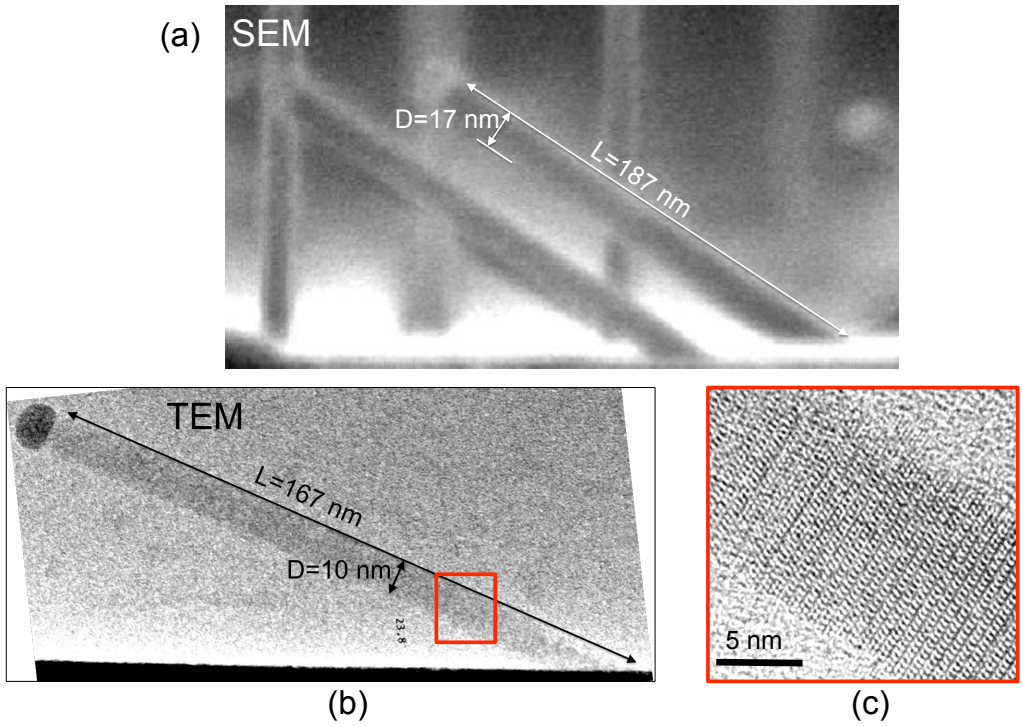

Figure 2.4: Typical nanowires originating from the same sample imaged by two techniques: (a) SEM and (b) HRTEM. Nanowire diameters appear consistently larger on the SEM images compared with TEM measurements. (c) Close-up of area boxed in (b), showing a sharp image of the crystal that allows a more accurate measurement of the diameter to be made. The nanowire total lengths is nevertheless consistent between both techniques.

In figure 2.4, we show two nanowires originating from the same sample and imaged by SEM and by TEM. We notice that the nanowire sidewall edges on the SEM image do not appear as sharp as on the TEM image. For the sample in figure 2.4, nanowire diameters measured on the SEM images were consistently ~1.5 times larger than on TEM measurements (this comparison springs

from the comparison of 3 more sets of nanowires). For this reason, we did not measure diameters on SEM images, but relied instead on the more precise TEM images. This limit in resolution does not significantly affect the total nanowire length measurements.

2.3 Transmission Electron Microscopy (TEM)

2.3.1 Instruments and Sample Preparation

In order to obtain crystallographic information on our nanowires, we needed to rely on TEM measurements. All the measurements were performed in our group by Martien Den Hertog and Catherine Bougerol.

X-ray diffraction measurements could not be used to produce crystallographic information because of the small volume of nanowires obtained on each sample, the overwhelming background due to the substrate, and the impossibility to efficiently separate the nanowires from the substrate for powder-type measurements. Although RHEED also produced diffraction patterns, it was not in our power to interpret them for crystallographic information on the nanowires (the accurate interpretation of complex RHEED patterns is not routinely done in growth experiments and would require a separate study with diffraction simulations).

TEM is a unique and powerful tool in that it can give a range of information on a nanometric scale like the crystal structure and crystal orientation, the types of defects (dislocations, twin boundaries, stacking faults), and their locations. TEM can also provide information on chemical composition of materials on a nanometric scale with the use of electron energy loss spectroscopy (EELS), High Angle Annular Dark Field Scanning TEM (HAADF-STEM or Z-Contrast Imaging) and Energy Dispersive X-Ray Spectroscopy (EDX).

Like for every instrument, the use of TEM has it's drawbacks. Although TEM is a very versatile tool, the measurements are time consuming and the sample preparation is very delicate. Many more nanowire samples could be produced by MBE than could be measured by TEM. Also, because TEM uses a tightly focused and very powerful electron beam (with up to 400 kV tension in our case), our nanowires were easily damaged under the beam, as is evidenced in figure 2.5.

The High Resolution TEM (HRTEM) images were realized on a JEOL 4000 EX microscope, operated at 400 kV and equipped with a GATAN 2 K CCD camera. A JEOL 3010 microscope operated at 300 kV was used for HRTEM and Energy Filtered (EFTEM) imaging, equipped with a GATAN 1K x 1K CCD camera. HAADF STEM images and EDX spectra were obtained on a probe C_s corrected FEI TITAN TEM operated at 300 kV, and also on a Hitachi S 5500 SEM microscope operated at 30 kV. The EDX spectra were fitted and corrected using the Cliff-Lorimer method to obtain a composition profile along the NWs.

TEM samples were prepared by three different methods:

- cleaving method [52];
- classical mechanical polishing followed by Ar^+ ion milling using a GATAN PIPS;
- dispersion of the nanowires on a holey carbon grid by direct contact with the sample.

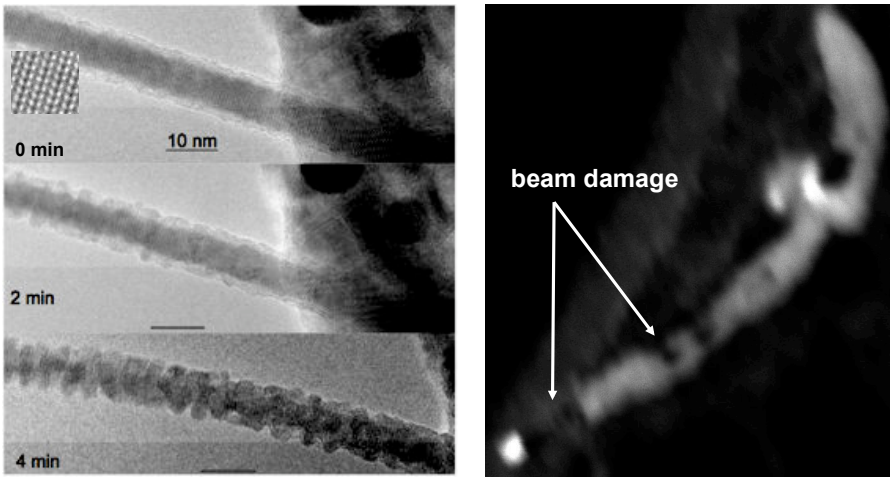

Figure 2.5: Damage to 10 nm diameter ZnSe nanowires caused by TEM beam during measurements. (a) Heating is believed to cause the nanowire structure to go from being single crystal to being amorphous over a period of 4 minutes. (b) The TEM beam can also completely vaporize the material and leave holes in the investigated specimen.

A thin carbon layer (5-10 nm) was deposited on the dispersed and cleaved nanowire samples to reduce movement of the nanowires and to protect them from beam damage.

HRTEM was useful in this thesis project for finding out about the crystal structure of the nanowires. HAADF-STEM, a specimen mapping technique relating image contrast to atomic number Z, was also used less extensively for locating ZnCdSe heterostructures grown in ZnSe nanowires. Some examples are shown in figure 2.6.

Next we briefly describe two more TEM techniques which were used for investigations of heterostructures in this thesis, but which are less commonly used in nanowire investigations found in the literature.

2.3.2 Geometrical Phase Analysis (GPA)

GPA is a simple and efficient method for measuring variation in lattice spacing in periodic type images and especially HRTEM images. In a few steps GPA averages and fits the best lattice spacing in a given region and in a chosen direction. The detection limit on interplanar separation is 0.1 pm for interplanar spacing of 0.2 nm when analyzed on a 9×9 nm^2 area [53].

We used GPA analysis on HRTEM images of nanowires to locate CdSe heterostructures. The nanowire images we used for GPA analysis showed a hexagonal (0001) or cubic (111) structure along the growth axis. Since the CdSe (0001) interplanar spacing (0.350 nm) is larger than the ZnSe interplanar spacing (0.327 nm), GPA can be used to locate the CdSe segment and to reveal its extent. The area of the nanowire analysed by GPA exceeds the area probed in Ref. [53] so we can also expect a good resolution and an accurate variation of interplanar spacing (see figure 2.7.

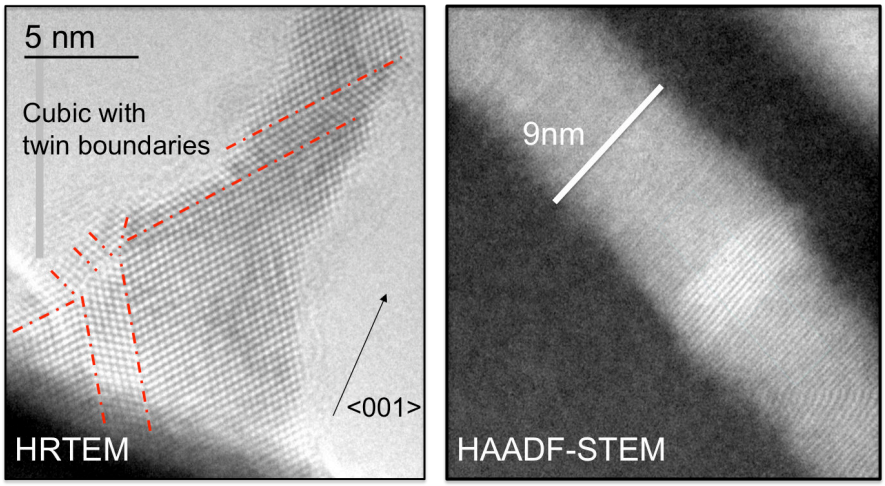

Figure 2.6: (a) Base of a ZnSe nanowire imaged in HRTEM. (b) ZnSe nanowire with a CdSe heterostructure segment imaged by HAADF-STEM: the CdSe segment appears brighter because Cd has a larger atomic number than Zn (Z_{Cd}=48 , Z_{Zn}=30).

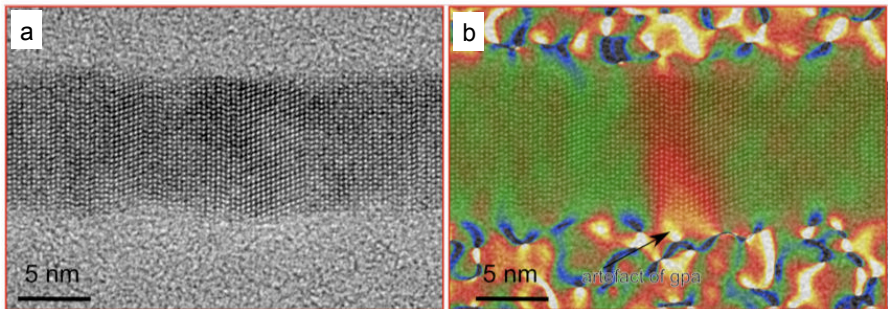

Figure 2.7: (a) HRTEM image of a nanowire at the location where a lattice parameter variation has been found. (b) GPA analysis of the image in (a) showing the cartography of lattice spacing.

2.3.3 Energy Filtered Transmission Electron Microscopy (EFTEM)

EFTEM is a technique for chemical mapping that relies on Electron Energy Loss Spectroscopy (EELS) of electrons transmitted through the sample. In EELS, spectra specific electron energy loss edges appear as peeks, and they can be compared with documented ionization edges to identify the presence of specific atoms. When we are only interested in finding out about the presence of one atom in particular, then a map of EELS spectra can be collected over the specimen with the energy window fixed at the energy threshold associated with the atom of interest. For each map location the EELS spectra are fitted to reveal the relative abundance of the atom at that location. Since three spectra (2 pre-edge and 1 post-edge) need to be collected at each map location, a good chemical map resolution requires a long exposure of the sample to the TEM beam, which usually causes contamination and damage to the specimen. The nanowires investigated by EFTEM were indeed very easily damaged. Examples of EFTEM chemical maps are presented in figure 2.8.

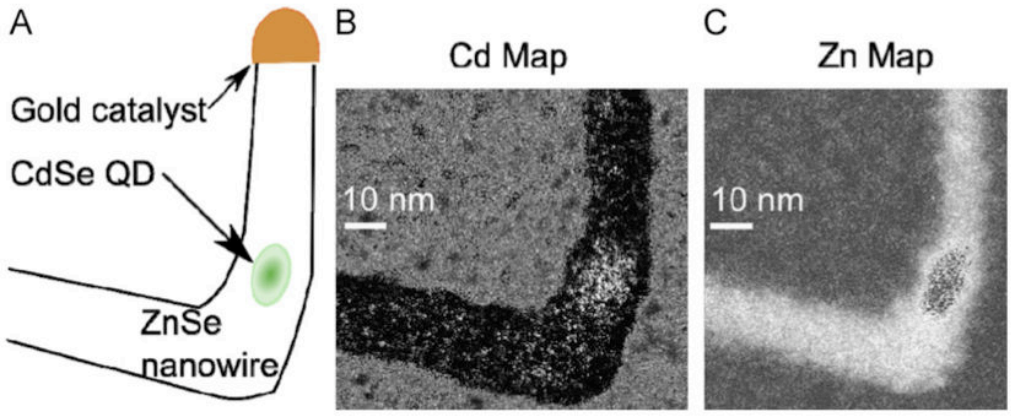

Figure 2.8: Composition maps of Cd and Zn obtained by using EFTEM on a ZnSe NW containing a CdSe QD. Bright contrast indicates the presence of the atom of interest. (A) Schematic of the investigated NW; (B) Cd composition map (using the Cd M edge at 404 eV), and (C) Zn composition map (using the Zn L edge at 1020 eV). A thin shell (2 nm) of ZnSe is visible around the QD. Taken from Ref. [54].

2.4 Photoluminescence Spectroscopy

Photoluminescence mesurements were performed in our group for the most part by Samir Bounouar, but also by Peter Stepanov and Claudius Morchutt. The measurements were aimed at investigating the nanowires. The nanowires were observed either on their original substrate or detached onto patterned Si substrates by direct mechanical contact with the growth substrate. In all cases, the measurements were done in µ-photoluminescence mode with a laser excitation focused to around 1 µm in diameter on the specimen, with an objective NA=0.4 chosen for it's working distance.

Three different lasers were available for the experiments: a continuous 405 nm blue diode laser, a 475 nm monomode laser, and a near infra-red Ti-Sa laser. For pulsed excitations (eg. for triggered photon emission measurements), the Ti-Sa laser could be used in pulsed regime with 1 ps pulses

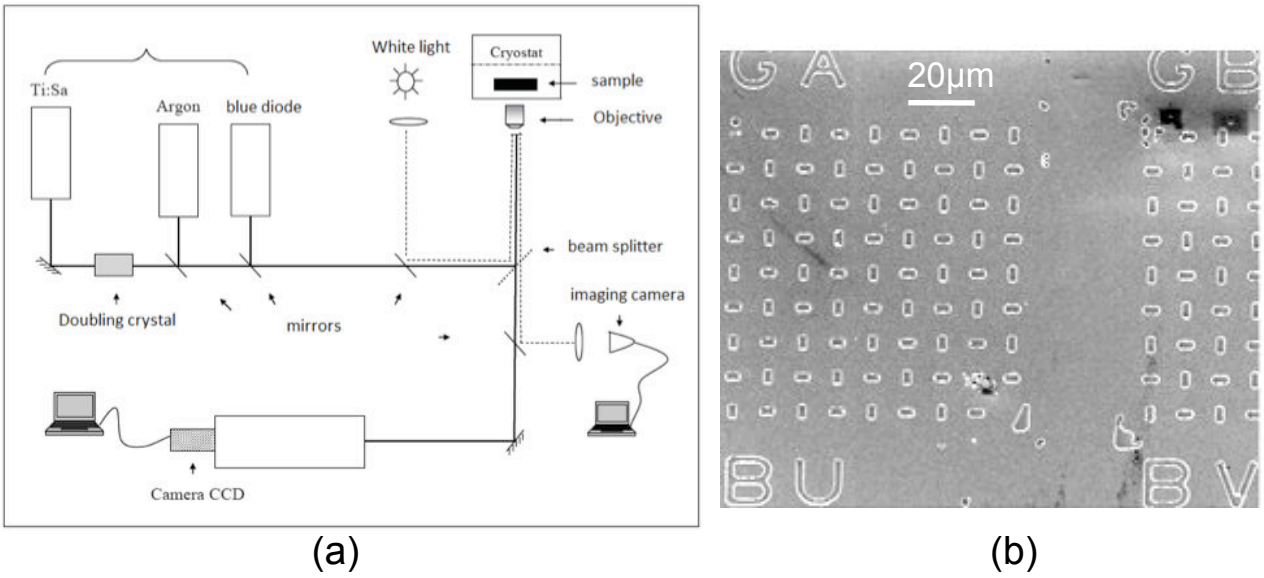

Figure 2.9: (a) Basic photoluminescence setup. (b) Patterned Si waffer.

and at an 80 MHz repetition rate. The Ti-Sa could provide a pumping wavelength with sharp band excitation tunable from 400 nm to 500 nm.

Because the laser emission as well as the nanowires are linearly polarized, $\lambda/2$ polarizers were placed in the excitation and detection paths to optimize the excitation and detection efficiencies. Furthermore, precise control of the excitation power was achievable with an additional $\lambda/2$ polarizer coupled to a polarization selector placed on the excitation path. Otherwise, optical densities were used for rough power tuning.

The photoluminescence measurements were performed at variable temperatures in a He circulation cryostat with high mechanical and temperature stability crucial for experiments requiring long integration times, including at room temperature. To allow rough displacement of the specimen around the excitation focus, the cryostat was mounted on micrometer stages. For fine position optimization piezoelectric controls were also implemented. The spectrometer setup mounted with CCD cameras could reach a resolution ~ 200 µeV.

Chapter 3

Au Catalyst Preparation on ZnSe Surface

Contents

3.1 Chapter Introduction

In catalyst-assisted nanowire growth on semiconductor substrate, the catalyst seed is responsible for determining the size and location of the nanowires. It is therefore interesting to pay attention to the the catalyst preparation.

E-beam lithography was used by some research groups to prepare metal catalysts in array patterns [55, 56] and diameters as low as 10 nm were achieved [47]. This is probably the best technique to achieve utimate control over the nanowire diameter and location. But one needs to have the tool at its disposal and the technology needs to be compatible with the substrate used. In general two other options are available for preparing the catalyst: coating a substrate with metal colloidals in solution, or dewetting a metallic thin film. The use of colloidals allows one to choose the catalyst size (colloidal solutions are commercially available with specified diameters); furthermore by diluting the colloidal solution one can achieve a range of catalyst surface densities on the substrate. This technique can be tricky if the colloidals don't bind properly to the substrate surface. The dewetting option is probably the most practical technique to use in nanowire synthesis requiring an ultra-high vacuum (UHV) environment because of the absence of wet chemistry. It is especially practical when the metal catalyst can be deposited directly in the growth chamber because then the entire process of catalyst preparation and nanowire growth can be achieved without the risk of pollution or oxidation. The drawback of the dewetting technique is that it offers limited control over the catalyst size and surface density. These two parameters evolve together following a ripening behavior and the details of this relationship can be specific to each metal-substrate combination.

In the current project we prepared the Au catalyst particles by dewetting an Au thin film on a ZnSe surface.

There are two reports in the literature of such gold particle generation on ZnSe, those of Chan et al. [57] and Wang et al. [58], published by the same research group. The procedure reported consists in the evaporation of a 0.3 nm thick layer of Au on a (001) oriented ZnSe surface followed by a 10 minute anneal at temperatures 500°C to 530°C. This produced gold particles 15 to 25 nm in diameter lodged at the tip of nanotrenches (see figure 3.1). These nanotrenches were up to a few hundred nanometers long and pointed exclusively in [110] and [-1-10] directions. The reports also demonstrated that the nanoparticles observed ex-situ were single-crystals with an FCC structure typical of Au. Energy dispersive x-ray measurements demonstrated that the particles were slightly alloyed with a small percentage of Zn (less than 14 at.%) when the annealing temperature exceeded 530°C, but that the gold didn't alloy for annealing temperatures closer to 500°C. Furthermore the particles were found to be approximately semi-spherical in shape. We summarize these results in figure 3.1.

In this chapter we present our studies and observations of Au nanoparticles, which we generated following the same general method as Chan et al. [57]. More particularly, our procedure consisted in evaporating a gold layer from an effusion cell on (001) ZnSe surfaces at room temperature and then annealing the gold layers under vacuum by heating the substrates. The Au evaporation took place in a dedicated UHV metal deposition chamber connected to the growth chambers by UHV modutrac tunnels for sample transfer. The thermal annealing procedures took place in the growth II-VI chamber. Various annealing temperatures were tested, as well as gold thicknesses. The Au

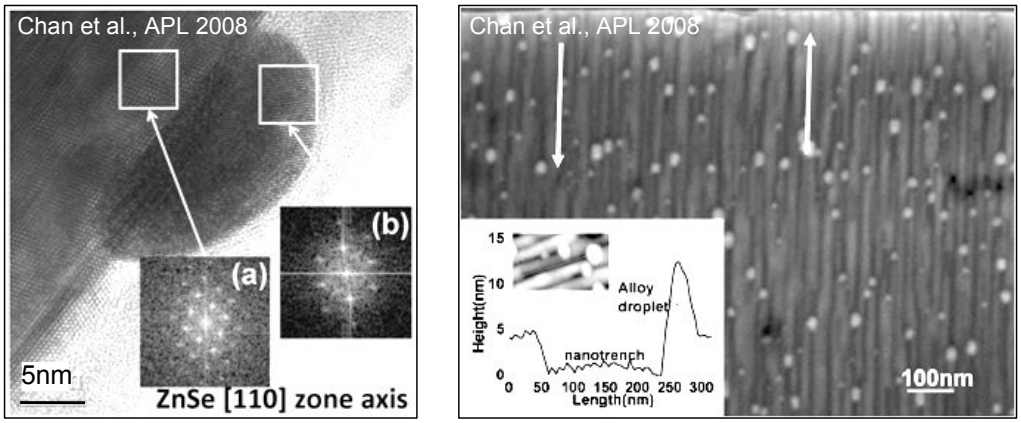

Figure 3.1: Au nanoparticle generation on ZnSe (001) observed by Chan et al. [57]. *Left* TEM of Au nanoparticle confirming its FCC structure. *Right* SEM image of nanoparticles lodged at the tip of 200 nm long nanotrenches.

particle generation process was monitored in-situ by RHEED and observed ex-situ by SEM.

We start by explaining how we obtain the ZnSe surface and we provide a cause for the appearance of the nanotrenches which complements the nanotrenches formation mechanism suggested by Chan et al. [57].

3.2 ZnSe Surface Preparation

3.2.1 Effect of GaAs Surface Preparation on ZnSe Thin Film

The ZnSe thin films were prepared on commercial GaAs (001) substrates. The GaAs substrates were prepared in two different fashions prior to the ZnSe thin film growth. In the first way we heated the substrates under vacuum by flashes (heating rapidly and for a short time) above the GaAs amorphous oxide sublimation temperature of 580°C in order to remove the oxide layer. We interrupted the cycle of flashes upon the appearance of a two-dimensional RHEED diffraction from the exposed crystalline GaAs surface. This procedure has the disadvantage of yielding a low quality surface with an rms roughness of 1.86 nm due to many pits and unusual surface structuration, as was revealed by AFM (see figure 3.2a). The ZnSe thin film epitaxially grown on this GaAs surface showed structural defects after it was annealed above 500°C: elongated nanotrenches directed in [110]/[-1-10], as well as pits were visible on the surface by SEM (figure 3.2b). This is due probably to a creep of the ZnSe material when heated, to conform to the morphology of the GaAs surface underneath.

To obtain a smoother ZnSe thin film, it was preferable to start by producing a high quality GaAs epilayer in a dedicated III-V MBE chamber. This was done by first deoxidizing the GaAs substrate above 620°C under As flux, to preserve the integrity of the crystalline surface (since As tends to desorb from the GaAs surface above 400°C); and then by growing a ~200 nm thick GaAs epitaxial layer with atomic smoothness (rms roughness of 0.30 nm – see figure 3.2c). ZnSe thin films grown on these smooth surfaces did not produce surface irregularities when annealed (figure 3.2d).

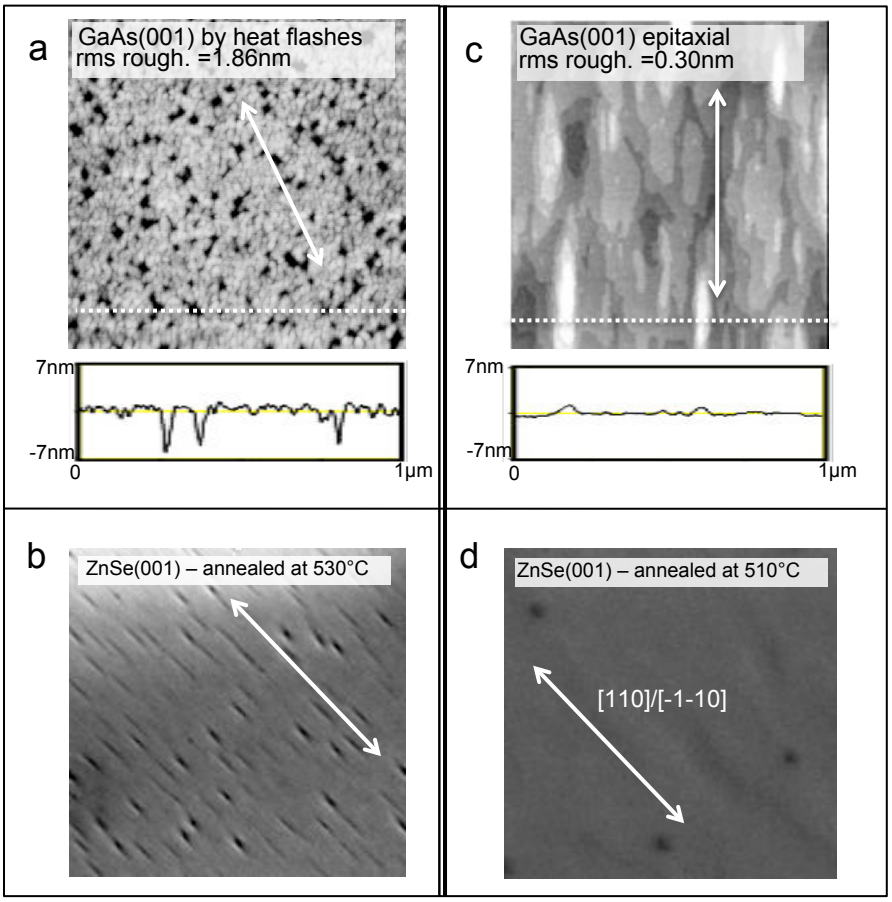

Figure 3.2: Effect of GaAs surface treatment on ZnSe epilayer observed after ZnSe layer anneal. (a) AFM topograph of GaAs substrate surface deoxidized by repeated heat flash sublimation. Line scan made along the dotted line showing rough surface with up to 7 nm deep pits; these pits are believed to be the cause of visible nanotrenches seen in the SEM scan in (b) of the annealed ZnSe surface. (c) AFM topograph of GaAs substrate deoxidized under As flux and with additional growth of GaAs epilayer with monolayer smoothness; no nanotrenches nor other visible defects are observed in SEM scan in (d) of annealed ZnSe epilayer grown on the smooth GaAs surface. Arrows show [110]/[-1-10] directions. All images are 1 µm x 1 µm. Dark spots are a result of ablation of surface lying SeO_2 islands [59].

3.2.2 ZnSe Thin Film Growth on GaAs

ZnSe and GaAs only have a 0.25% mismatch, which allows us to grow them easily in heterostructure. By using a ZnSe thin film we hoped to shield the nanowires from Ga or As impurities and to improve the epitaxial relationship between the nanowires and the substrate.

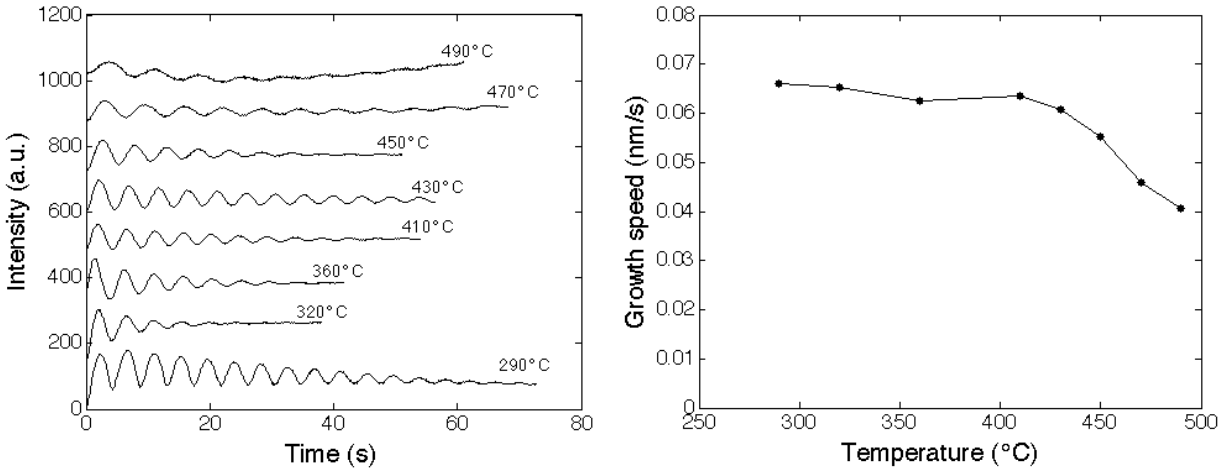

Figure 3.3: RHEED oscillations used to monitor the growth speed of ZnSe (001) thin film at various temperatures and for the same fluxes as used during NW growth experiments.

The ZnSe thin film was grown in general to a thickness of around 30 nm, below the critical thickness for plastic relaxation of ZnSe on GaAs, i.e. 150 nm [60]. The ZnSe growth was carried out at 280°C by alternating the standard MBE growth mode and atomic layer epitaxy (ALE) growth mode, which allows one to obtain a better surface smoothness [61]. The Se:Zn beam pressure ration (BPR) was 4 with a Se flux of 1e-6 Torr. The growth speed under continuous beam fluxes (MBE mode) was typically 0.06 nm/s (0.2 ML/s), as measured by RHEED oscillations.

For the sake of investigations of nanowire growths carried out at higher temperatures that will be presented in the next chapter (chapter 4), the growth speed of the ZnSe layer was also measured under continuous fluxes (MBE mode) for growth temperatures ranging from 290°C to 490°C. The results are shown in figure 3.3. Note that each oscillation period corresponds to one monolayer (1 ML) of height 0.284 nm, i.e. $\frac{a_{ZnSe}}{2}$.

3.2.3 Formation of Nanotrenches

Chan et al. [57] report that annealing a gold thin film on a ZnSe (001) layer above 530°C will create surface lying nanotrenches pointing in the [110]/[-1-10] directions. According to Wang et al. [58] these nanotrenches are v-shaped elongated grooves exposing (111)B, Se-termininated, sidewalls along their lengths, while exposing a (111)A, Zn-terminated, facet at the tip. The proposed mechanism for the formation of the nanotrenches is suggested to be a catalytic decomposition of the ZnSe at the Zn-terminated facet by gold nanoparticles, causing the vaporization of Zn and Se: $2ZnSe \xrightarrow{catalyst} 2Zn + Se_2$. According to Chan the activation energy of this reaction is around 530°C, at which point gold also alloys with Zn to produce an $AuZn_\delta$ complex with δ =0.14.

We performed the same annealing procedure as Chan with a gold layer on ZnSe surfaces and an annealing temperature of 530°C. We found different outcomes depending on the surface preparation used for the GaAs surface. When the ZnSe had been grown on rough GaAs (associated with deoxidation by flashes), we also observed nanotrenches with gold particles lying at their tips (figure 3.4b). These nanotrenches appeared sharper and deeper than the nanotrenches that appear spontaneously upon annealing ZnSe without gold (figure 3.4a). When the ZnSe had been grown on a smooth GaAs epilayer then no nanotrenches appeared and the gold particles remained on the (001) surface (figure 3.4c-d).

Wang et al. [62] also agree that the process of annealing a ZnSe epitaxial layer grown on GaAs (001) will by itself create nanotrenches pointing in the [110]/[-1-10]. Wang does not however mention which surface treatment was used on the GaAs (001) substrate surface.

It will be interesting to note that alligned nanotrenches and terminated by a gold particle have also been observed by Gosh et al. [63] on GaAs (001), following the thermal anneal of a gold thin film. Gosh insists that the depth and orientation of the nanotrenches was highly dependent on the the type of (chemical) treatment used to prepare the GaAs surface.

We conclude therefore that gold will decompose the ZnSe surface only under the condition that it is guided by elongated defects caused to the ZnSe layer by the roughness of underlying GaAs. In the absence of elongated defects the gold particles cannot easily penetrate the stoichimetric (001) surface to start a catalytic reaction on (111)A planes.

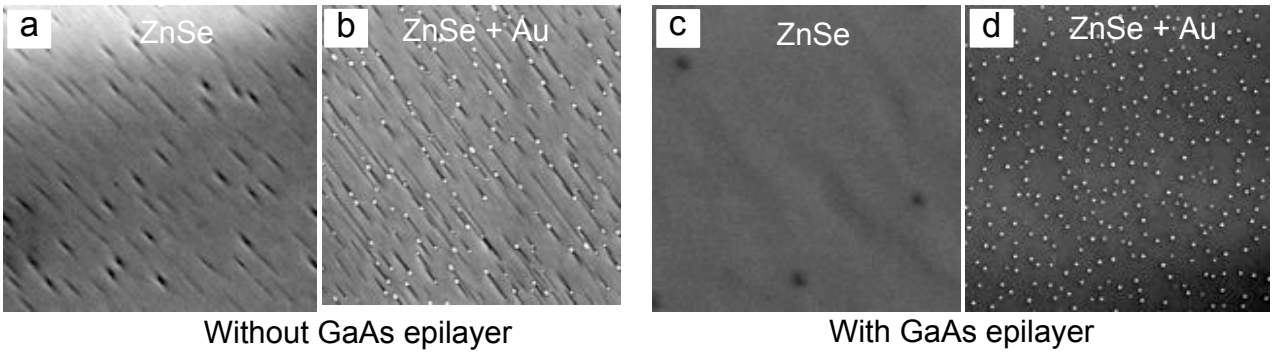

Figure 3.4: Nanotrenches in ZnSe annealed for 10 min above 500°C linked to the treatment of GaAs substrate surface. (a)-(b) ZnSe was grown on rough GaAs deoxidized by flashes; nanotrenches appear when the surface is annealed without (a) or with an Au film (b). (c)-(d) ZnSe grown on smooth GaAs epilayer; there is no evidence of nanotrenches when the surface is annealed without Au (c) or with Au (d). (Black spots in (c) appear following ablation of SeO_2 islands by SEM beam [59] - they are of no consequence to current experiments.)

For our research we have sought to avoid creating nanotrenches because we believe that they represent inhomogeneities in the adatom capture zone of the nanowires, breaking the isotropicity of the adatom flow from the substrate to the base of the nanowires. Therefore we have grown an epitaxial layer of GaAs prior to growing the ZnSe substrate, whenever possible.

3.3 RHEED Observation of Nanoparticle Nucleation

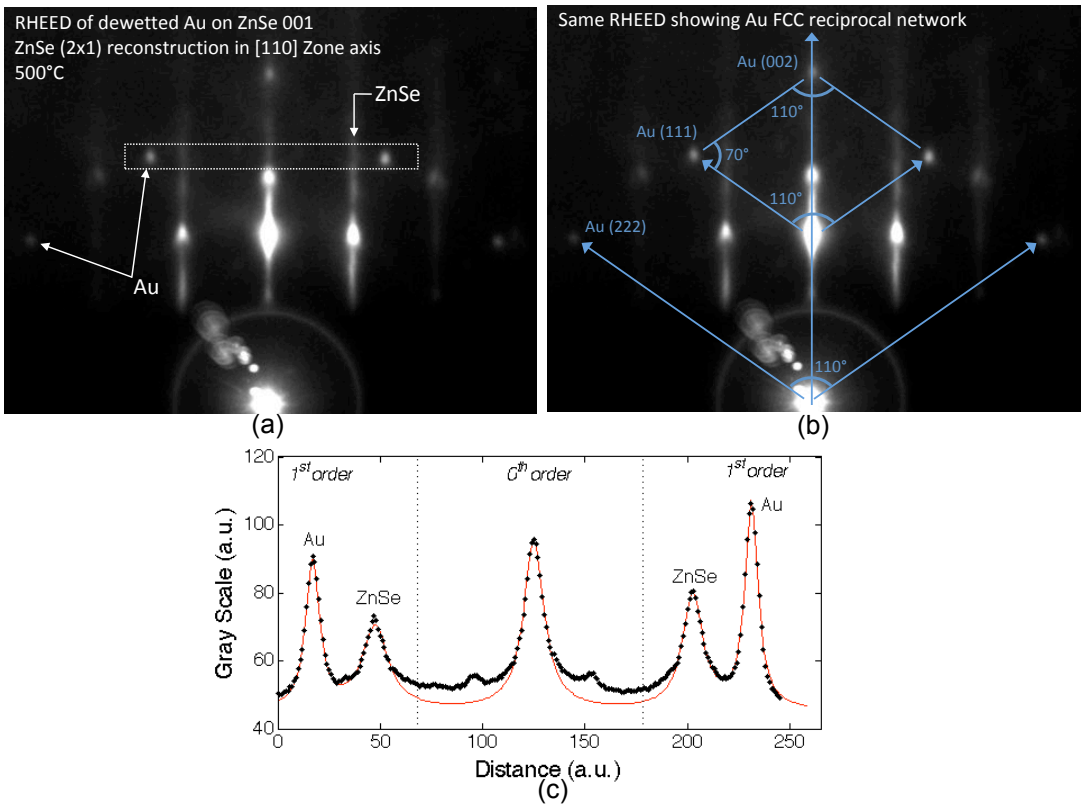

Figure 3.5: RHEED diffraction of ZnSe (001) surface in the [110] zone axis showing the ZnSe (2×1) reconstruction and crystalline FCC Au nanoparticles. The indexed spots in (b) show the type of diffraction plane. (c) Image brightness line profile in of the region inside the dotted box in (a). The brightness profile is fitted with 5 lorentzian curves; the relative separation of the ZnSe and Au diffraction features allows us to deduce a room temperature value for the Au lattice parameter $a_{Au} = 4.074 \pm 0.010$ Å, in close agreement with the reported value of 0.40786 [64].

The nanoparticle nucleation could be followed by watching the RHEED of the samples while the gold thin film was being annealed. From room temperature until 350°C only the two-dimensional RHEED pattern of the ZnSe (001) surface could be observed. Between 350°C and 400°C we could notice the appearance of additional diffraction spots, and these spots remained unchanged until annealing stopped at 500°C (figure 3.5a). These diffraction spots appear only in the presence of a gold film, and therefore we attribute them to gold diffraction. The fact that we can observe the RHEED diffraction of gold nanoparticles on the ZnSe surface gives two important indications. Firstly, we know that the gold nanoparticles are in the form of solid crystals. This behaviour is different, for instance, from the case of gold dewetting on a Si surface or on GaAs, where gold tends to form liquid eutectics with Si and Ga respectively. Secondly, the fact that the gold diffraction spots are ordered rather than in a ring pattern tells us that the gold crystals lay in a specific orientation with respect to the ZnSe substrate. This will also be demonstrated in ex-situ HRTEM images of crystalline Au catalysts on ZnSe nanowires in chapter5. Figure 3.5a shows the RHEED of the ZnSe (001) surface

in the [110] zone axis with the (2×1) surface reconstruction. On the same snapshot (reproduced in figure 3.5b) it is possible to match the fundamental FCC reciprocal network to the gold diffraction spots. This suggests that the ZnSe and Au crystals have identical orientations.

We can determine the in-plane lattice constant of Au, a_{Au}, by taking the ratio of the distance separating the two first order diffraction spots over the distance separating the two first order diffraction streaks of ZnSe, and by multiplying by ZnSe lattice constant. The precise positions of the diffraction features were obtained by fitting the image brightness profile shown in figure 3.5c with five lorentzian curves (one 0th order and four 1st order diffraction features). Since the thickness of the ZnSe layer (~30 nm) deposited on GaAs is well below the critical value for relaxation (150 nm), we consider the ZnSe lattice to be fully strained on GaAs and to adopt the GaAs in-plane lattice parameter, i.e. a_{GaAs} = 5.653 Å. Furthermore we note that the RHEED image was recorded at a sample temperature of 500°C, so we therefore take into account the linear thermal expansion of Au ($\alpha_{Au} = 13.99 \times 10^{-6}\mathrm{K}^{-1}$) and GaAs ($\alpha_{GaAs} = 5.7 \times 10^{-6}\mathrm{K}^{-1}$) to derive a_{Au} for room temperature. We obtain a room temperature value of $a_{Au} = 4.074 \pm 0.010$ Å. The referenced room temperature lattice constant of FCC gold is a_{Au} =4.0786 Å [64]. Within our measurement uncertainty of ±0.25% our value agrees perfectly well (0.11% difference) with this reported value for unalloyed gold. According to Ref. [65] Se has a negligible solid solubility in gold; however the Zn content in FCC gold can reach 27.5% above 400°C with an associated modification of the gold lattice parameter (see figure 5.3). According to data reported in Ref. [64], our experimental gold parameter value of 4.074 Åwould indicate a 2.5 at.% Zn presence. The Zn content allowed by our measurement uncertainty, i.e. for a_{Au}=4.064 to 4.0786 Å, is 0 to 8 at.%. Note that a_{Au} decreases with increasing Zn content.

The close agreement between our experimental gold lattice parameter with the referenced value demonstrates the ZnSe and Au crystal are indeed similarly oriented.

In chapter 5 we conduct a similar study of RHEED diffraction with the Au catalyst on ZnSe nanowires.

3.4 Nucleation of Au Particles vs Annealing Temperature

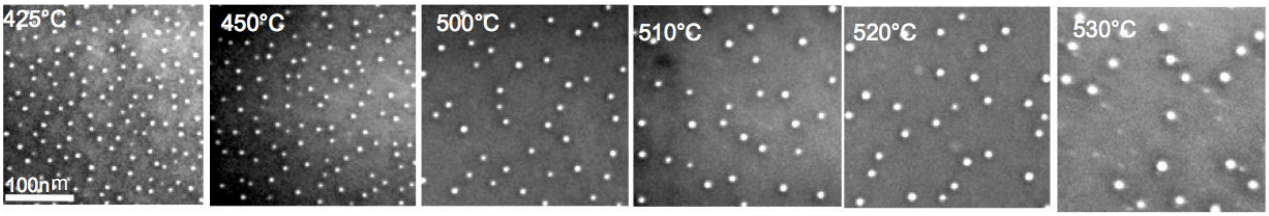

Figure 3.6: SEM image of Au nanoparticles generated on ZnSe surfaces with an initial deposition of ~0.5 ML of Au and annealed for 10 minutes at the temperatures indicated in the figure.

Here we show a study where we observe how the diameter and the surface density of the particles behave when a gold layer is annealed for 10 min at different temperatures. Six GaAs (001) substrates were prepared with epitaxial growths of GaAs followed by ZnSe, and a gold layer of equal thickness was evaporated on each substrate (20 seconds exposure to the Au flux for each sample). These samples

were annealed at six different temperatures ranging from 425°C to 530°C. The lowest temperature was chosen to be a few tens of degrees above the first appearance of gold diffraction on RHEED. Samples were then observed ex-situ by SEM and resulting images were fitted using ImageJ, an image analysis software, to obtain the visible area of each particle on the surface (see figure 3.7). It is interesting to mention that a seventh sample was annealed at 600°C, but this sample showed extensive damage to the surface caused by heat, and no visible remnants of gold could be observed.

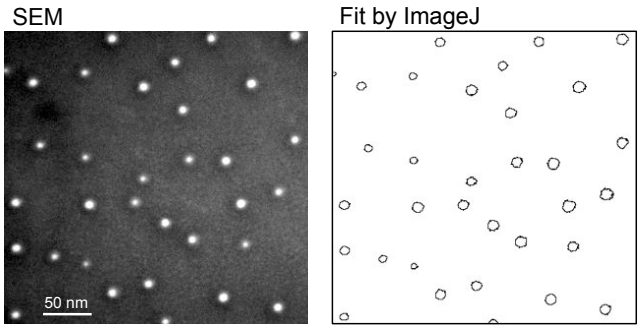

Figure 3.7: SEM image of Au nanoparticles on ZnSe surface and fit of image performed with ImageJ.

The histogram in figure 3.8 shows the distribution of particle diameters we observe at the different annealing temperatures for an area of 0.4 μm^2. The mean particle diameter increases monotonically with annealing temperature from 4.1 to 11.6 nm and we observe a standard deviation in the diameter distributions between 1.0 and 3.0 nm. We also observe a decrease of the surface density from 1600 to 300 μm^{-2} between 425 and 530°.

Given that we deposited the same volume of gold, V, on each of the six samples used in this experiment, we plot in figure 3.9 the logarithm of nanoparticle surface density σ versus the logarithm of their mean diameter d to probe for a simple relationship based on the geometry of the catalyst seeds.

The exponent from the fit tells us that a conservation of total gold volume is possible if we assume that

$$\frac{V}{A} = \sigma h \pi \left(\frac{d}{2}\right)^2 \tag{3.1}$$

or

$$\sigma = \frac{4}{\pi h}\frac{V_{Au}}{A}\frac{1}{d^2} \tag{3.2}$$

and

$$\log(\sigma) = \log\left(\frac{4}{\pi h}\frac{V}{A}\right) - 2\log(d). \tag{3.3}$$

where A is the surface area taken as A=1 μm^2. The height h needs to remain constant, meaning that the nanoparticles are discs with constant height that only vary in their diameters. We attempted to obtain the height by obtaining the AFM topography of the gold catalysts.

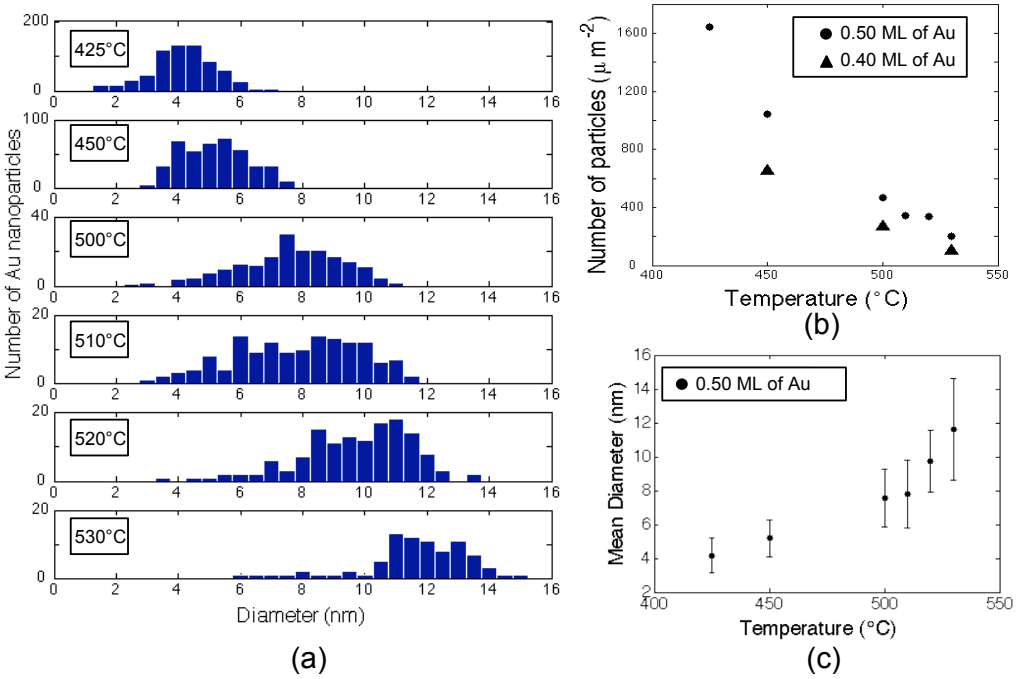

Figure 3.8: Size and surface density of Au catalyst nanoparticles observed as a function of annealing temperature for initial amount of Au=0.50 ML and anneal time of 10 min. (a) Diameter distribution for particles measured on a 0.4 μm^2 surface area for each sample. Graphs (b)-(c) extracted from the histogram in (a). (Graph (b) also shows result for initial deposition Au=0.40 ML.) The error bars represent one standard deviation.

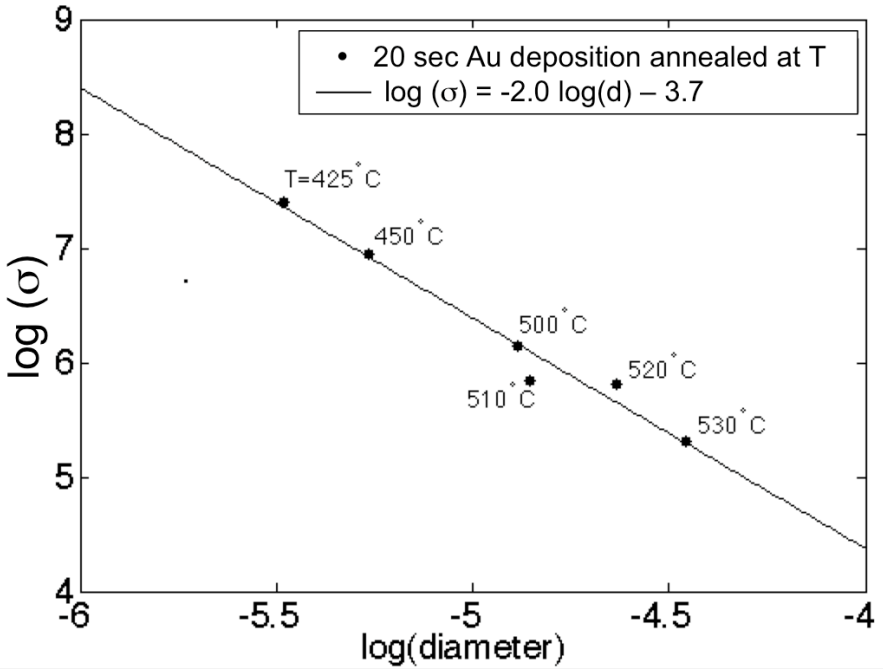

Figure 3.9: Logarithmic plot of catalyst surface density σ versus catalyst mean diameter for six samples annealed for 10 mins at different temperatures. Each sample started with an identical amount of Au on the ZnSe surface (plotted data taken from figure 3.8).

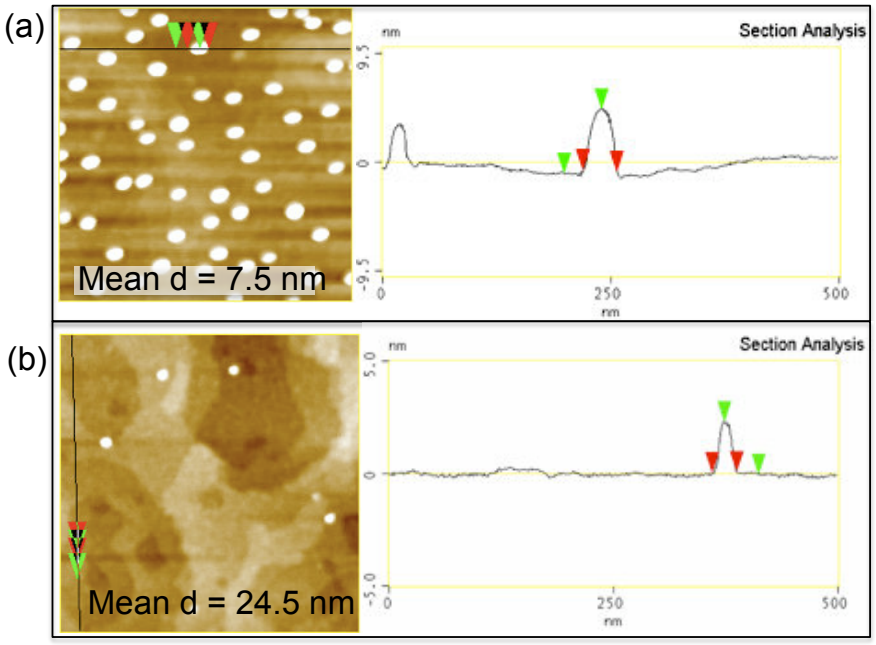

Figure 3.10: AFM images and topography line scans of two ZnSe samples covered with dewetted Au nanoparticles. The mean diameter of nanoparticles found on these samples, (a) d=7.5 nm, and (b)d=24.5 nm, were found by analyzing corresponding SEM images. The nanoparticle height appears to decrease with increasing diameter.

The samples presented in figure 3.10 were not annealed with the same amount of Au as the earlier samples (i.e not 20 sec of Au), but it would be logical to expect the constant height to be an intrinsic property of crystalline Au agglomerating on a crystalline ZnSe surface (the original samples had deteriorated due to oxidation by the time we performed the AFM study). It is not possible to obtain both the diameter and height of nanoparticles for $d < 20$ nm because we are limited by the resolution of the AFM tip, which itself has a diameter of 20 nm. But we can get the mean nanoparticle diameter corresponding to the AFM images by analyzing the corresponding SEM images (not shown). We get the graph of surface nanoparticle diameter versus surface density shown in figure 3.11.

The data is limited, yet we can tell that although the nanoparticle height doesn't remain constant. It also doesn't appear to vary significantly. The height hovers around 5 nm for particle diameters around 7-8 nm, while it measures 2.25 nm for the much larger particle diameter of 24 nm. We can use these observations to find an upper limit for the gold coverage we had in the samples of figure 3.8. We assume therefore that the constant nanoparticle height is $h = 0.0049$ µm (which corresponds to the average of the maximal nanoparticle heights in figure 3.11), in equation 3.4:

$$\log \sigma = \log\left(\frac{4}{0.0049\pi}\frac{V_{Au}}{A}\right) - 2\log(d) \tag{3.4}$$

Then by comparing this equation with the fit in figure 3.9 we get

$$-3.7 = \log\left(\frac{4}{0.0049\pi}\frac{V_{Au}}{A}\right), \qquad \frac{V_{Au}}{A} = 9.51 \times 10^{-5}\mu m. \tag{3.5}$$

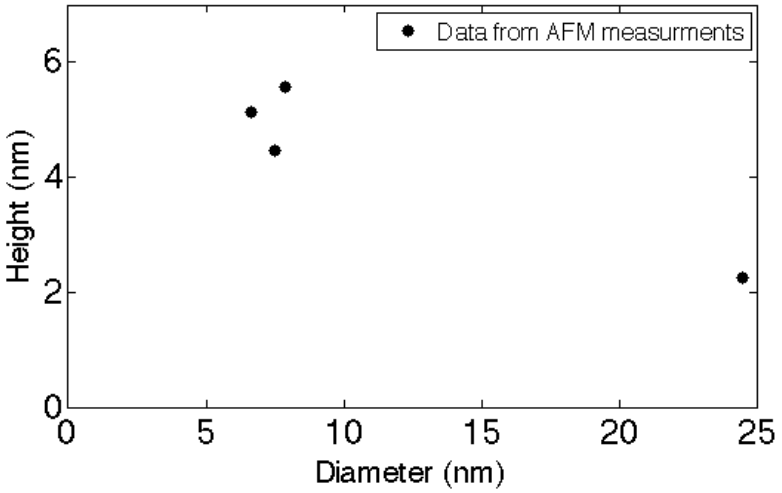

Figure 3.11: Nanoparticle height as a function of nanoparticle diameter.

And therefore the upper limit of Au coverage is 0.47 ML (1 ML=$\frac{a_{Au}}{2}$).

So here is what we can say about the temperature activated ripening of Au islands on ZnSe. Since we start with a fraction of a ML of gold it is logical that there is no wetting layer connecting the islands. The islands grow with temperature by conserving a disc, or pancake, geometry, with a rather slowly varying height with respect to the disc diameters. This contrasts with a hemispherical geometry where the height is equal to the radius. A disc geometry has a higher area to volume ratio than the hemispherical geometry. This would seem to indicate that the Au-ZnSe interface and the Au-vacuum energies are low compared to the bulk-Au energy. For the case of Au island dewetted on Si surface from a 2 ML Au thin film, Daudin et al. [66] explains that the interface energy γ_I between Au and Si is given by

$$\gamma_I = \gamma_{Si} + \gamma_{Au} - \gamma_{adh}, \tag{3.6}$$

where γ_{Si} and γ_{Au} are the surface energies of Si and Au at the interface and γ_{adh} is the adhesion energy between these surfaces. In the case of Au on ZnSe, a large value of γ_{adh} would explain the large interface area favored by the disc geometry for larger islands. In principle the Au crystal should adopt the orientation which minimizes the interface energy. Again according to Daudin et al., the adhesion energy is linearly linked with the bonding energy E_{Au-Si} at locations were Au and Si atoms vertically align at the interface to form "perfect bonds" (this depends on the crystal orientation, lattice mismatch and it may vary with temperature if the two materials have widely different thermal expansion coefficients). The adhesion energy is expressed as

$$\gamma_{adh} = \eta \frac{E_(Au - Si)}{\Omega^{2/3}}, \tag{3.7}$$

where Ω is the average atomic volume and η represents the fraction of "perfect bonds" between the two materials at the interface.

3.5 Nucleation of Au Particles vs Thickness of Au Thin Film

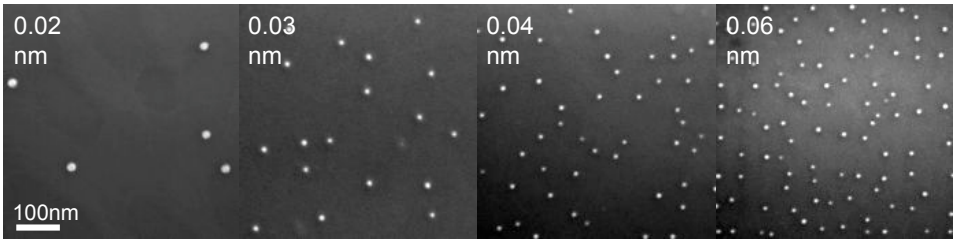

Figure 3.12: SEM images of Au nanoparticles on ZnSe surfaces for different initial amounts of gold annealed 10 min at 510°C.

In a second experiment we varied the initial amount of gold evaporated on the samples and kept the annealing temperature constant. We tested five samples with five different gold thicknesses from 0.09 to 0.5 ML. The thicknesses were deduced from the exposition time to the gold flux compared with the exposition time used in the previous experiment (section 3.4). All the samples were annealed for 10 min at 510°C, in the upper range of the temperatures probed in the previous experiment for generation of larger diameter gold particles and lower surface densities (desirable for widely spaced nanowires).

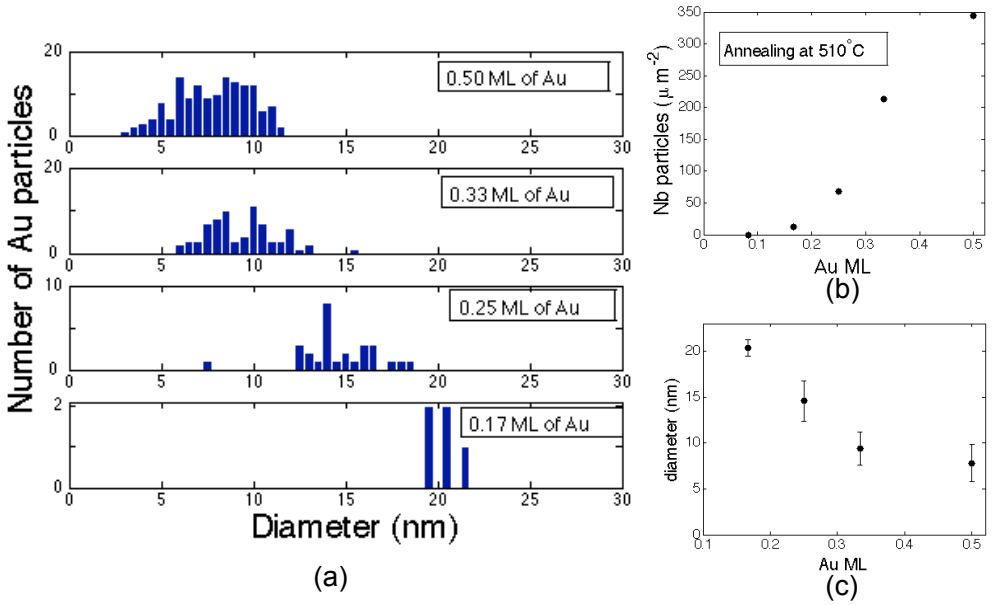

Figure 3.13: Size and surface density of Au catalyst nanoparticles observed as a function of initial amount of gold deposited for an annealing procedure lasting 10 min at 510°C. Graphs (b)-(c) are extracted from the histogram in (a). The error bars represent one standard deviation.

From the results shown in figure 3.13 we first note a significant decrease in the surface density of particles by a factor of 28 as the gold thickness is reduced by a factor of 3. At 0.17 ML of gold the surface density of particles is 12 µm^{-2}, or 12×10^{8} cm^{-2}. At the same time we note a steady increase of the particle mean diameter, reaching 20.4±0.9 nm for 0.17 ML of gold, with the smallest

standard deviation representing only 4% of the particle diameter. It is worth noting that this diameter homogeneity allows us to expect to grow nanowire with equally homogeneous diameters.

No gold particles are detected on the sample surface for a 0.09 ML of Au thickness. Linearly extrapolating the surface density of particles to find the x-intercept yields 0.018 nm, which could be interpreted as the critical gold thickness needed to favor island growth beyond the minimal size resolvable by our SEM (~2nm).

3.6 Conclusion

In conclusion we find that the the annealing temperature and the thickness of the initial gold film have an appreciable effect on the surface density of Au nanoparticles and on their mean diameter.

We also show that the appearance of nanotrenches on ZnSe surfaces annealed above 500°C depends on the type of GaAs surface preparation used.

Finally RHEED observation of crystalline diffraction of gold demonstrate that Au is solid during the nucleation process. The ZnSe and Au nanoparticle crystals are similarly oriented. From the RHEED diffraction image we extract a gold lattice constant of 4.074±0.010 Å. Within the uncertainty this value is in agreement with the reported value for pure FCC gold of 4.0786 Å. However the precise value we find indicates the presence of ~2.5% Zn in FCC gold, according to Ref. [64].

Chapter 4

Growth of ZnSe Nanowires: Experimental Results

Contents

4.1 Chapter Introduction

ZnSe nanowire growth followed after the generation of gold nanoparticles. ZnSe nanowires do not grow at the typical temperature we used for gold particle nucleation (around 500°C). For this reason, right after gold was nucleated the sample temperature was lowered and left to stabilize before the fluxes of Zn and Se were introduced. Unless otherwise indicated the nanowire growth temperature was 410°C and the fluxes were in excess of Se with a typical BPR of Se:Zn=4. All growths unless otherwise indicated took place were done on (001) oriented substrates. We investigated the influence of growth conditions on resulting nanowires by changing one growth parameter at a time and keeping all other parameters constant. In this manner we investigate the influences of nanowire surface density, growth time, substrate temperature, Se:Zn flux ratio, growth by atomic layer epitaxy (ALE) and growth on a (111)B surface.

Before exposing these different studies, we present the following mass-transport (diffusion) model for nanowire growth, which we will refer to for the interpretation of some results.

4.2 Mass-Transport Model of Nanowire Growth

Growth of a nanowire occurs as adatoms reach the growth front at the interface of the gold catalyst nanoparticle and the nanowire crystal. To quantify the growth process we choose to use the mass-diffusion model as presented by Johansson et al. [67]. This growth model was tailored for MOVPE growth, where the precursor gases impinge on all surfaces at equal rate. Therefore we will apply specific modifications which will make the model suitable for MBE growth. Refer to figure 4.1 for a sketch of the system geometry.

Johansson's mass-transport model is based on surface kinetic diffusion of adatoms impinging from the flux beam onto either the nanowire catalyst, the nanowire sidewalls or the 2D layer. For this model to be valid the following assumptions need to be made: (i) Adatom diffusion on all surfaces is at steady-state; (ii) incorporation of atoms into the nanowire crystal at the growth front is limited only by the the amount of atoms reaching the top of the nanowire and is not limited by any other process; the process within the catalyst (if there is diffusion of species through the catalyst) and / or at the catalyst-nanowire crystal interface need not be considered in detail; (iii) the interwire separation is large; (iv) the shape of the catalyst is a hemisphere. For this model we consider a cylindrical coordinate system with angular symmetry, as depicted in figure 4.1. The nanowire with length L grows in the z-direction and it has a radius r_w. In this model the catalyst-nanowire interface located at $z = L$ is treated as a sink, and as such it therefore provides the driving force for material flow. The nanowire growth rate is obtained from solving the diffusion equation for the surface concentration of adatoms at the 2D layer and at the nanowire sidewalls, with boundary conditions, as derived below [67].

First there is the surface concentration of adatoms on the 2D layer, n_s, which satisfies the following diffusion equation

$$D_s \nabla^2 n_s - \frac{n_s}{\tau_s} + R_s = \frac{\partial n_s}{\partial t} \tag{4.1}$$

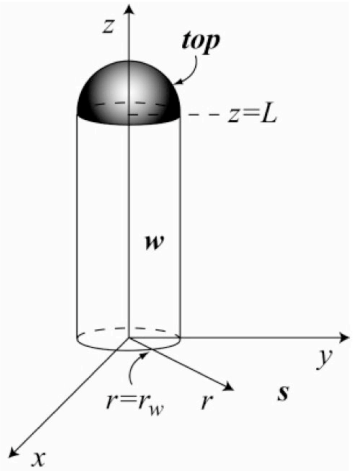

Figure 4.1: Schematic showing the coordinate system used for the mass-transport model. Taken from Johansson et al. [67].

where D_s is the surface diffusivity of adatoms on the 2D layer, τ_s is the average time an adatom diffuses on the 2D layer and R_s is the effective impingement rate of adatoms on the 2D layer. The laplacian operator in eq. 4.1 is given by $\nabla^2 = \frac{\partial^2}{\partial r^2} + \frac{1}{r}\frac{\partial}{\partial r}$, with no angular dependence because of symmetry. We set the boundary condition $n_s(r_w) = 0$ to mean that every adatom reaching the nanowire base gets captured by the nanowire. The bounded solution to eq. 4.1 is

$$n_s(r) = R_s\tau_s\left[1 - \frac{K_0(r/\lambda_s)}{K_0(r_w/\lambda_s)}\right] \tag{4.2}$$

where $K_0(x)$ is the modified Bessel function of the second kind and $\lambda_s = \sqrt{D_s\tau_s}$ is the average diffusion length on the 2D surface. Note that this solution for n_s is valid when the interwire separation is large compared to λ_s so that individual nanowires do not compete for the material available on the substrate (otherwise the term λ_s should be substituted by a function of the interwire distance).

Next there is the surface concentration of adatoms on the nanowire sidewalls, n_w which satisfies the one-dimensional diffusion equation

$$D_w\frac{\partial^2 n_w}{\partial z^2} - \frac{n_w}{\tau_w} + R_w = \frac{\partial n_w}{\partial t} \tag{4.3}$$

where z is the length coordinate along the nanowire with $z = 0$ at the nanowire base and $z = L$ at the nanowire-catalyst interface. D_w, τ_w and R_w are respectively the diffusivity, the diffusion time and the impinging rate on the nanowire sidewalls. Boundary conditions are set to demand adatom flux continuity at the nanowire base and vanishing adatom concentration at the nanowire-catalyst interface, i.e.

$$D_w\frac{\partial n_w(z=0)}{\partial z} = -D_s\frac{\partial n_s(r=r_w)}{\partial r} = Jsw \tag{4.4}$$

and

$$n_w(z = L) = 0. \tag{4.5}$$

. We get the solution for the adatom concentration on the nanowire sidewalls,

$$n_w(z) = R_w\tau_w\left[1 - \frac{\cosh(s/\lambda_s)}{\cosh(L/\lambda_w)}\right] - \frac{J_{sw}\lambda_w}{D_w}\frac{\sinh([L-z]/\lambda_w)}{\cosh(L/\lambda_w)} \tag{4.6}$$

where $\lambda_w = \sqrt{D_w\tau_w}$ is the diffusion length along the nanowire sidewalls. Furthermore

$$J_{sw} = -R_s\lambda_s\frac{K_1(r_w/\lambda_s)}{K_0(r_w\lambda_s)}. \tag{4.7}$$

There are two contributions to the nanowire growth rate $\frac{dL}{dt}$. The first comes from adatoms diffusing from the sidewalls to the growth front and is expressed as the adatom flux at $z = L$ multiplied by the nanowire circumference ($2\pi r_w$), multiplied by the atomic volume in the nanowire crystal (Ω) and divided by the cross-sectional area of the nanowire (πr_w^2). The second contribution comes from direct impingement onto the catalyst, expressed as a hemispherical area of the catalyst ($2\pi r_w^2$) multiplied by the impinging flux at the catalyst, R_{top}, multiplied by the atomic volume (Ω) and divided by the nanowire cross sectional area. That is,

$$\frac{dL}{dt} = -D_w\frac{dn_w}{dz} \times \frac{2\Omega}{r_w} + 2\Omega R_{top}. \tag{4.8}$$

Plugging the solution for n_w into eq. 4.8 gives the nanowire growth rate

$$\frac{dL}{dt} = \frac{2\Omega R_w\lambda_w}{r_w}\tanh(L/\lambda_w) - \frac{2\Omega J_{sw}}{r_w\cosh(L/\lambda_w)} + 2\Omega R_{top}. \tag{4.9}$$

In this equation, the first term gives the contribution to the growth rate due to diffusion of material deposited directly on the nanowire sides, the second term accounts for atom diffusion from the substrate surface, and the third term accounts for direct impingement on the catalyst particle. It is assumed that all atoms impinging on the catalyst will contribute to the nanowire growth. It is also assumed that the sticking coefficient is the same on all surfaces.

For growth by MOVPE, such as in the case reported by Johansson, it can be assumed that the precursors in vapor form surround the nanowires thus impinging at equal rate on both the 2D layer and on all sides of the nanowires. In that respect it is possible to set $R_w = R_s = R$, where R is proportional to the pressure of precursors in the growth chamber. This equality doesn't hold for MBE growth because in MBE the atomic flux is highly directional and impingement occurs only on surfaces exposed to the flux beam. In MBE the magnitude of R_s with respect to R depends on the angle of the flux beam with respect to the substrate surface, θ_B; the magnitude of R_w and R_{top} with respect to R additionally depend on the nanowire tilt angle θ_w and on the fact that the sample is rotated during growth about the substrate normal (see the schematic in figure 4.2a).

Let's apply geometrical factors to the impingement rates to make them applicable to the reality of a directional beam, and to make the model suitable for our MBE growth. R_s is related to R, the

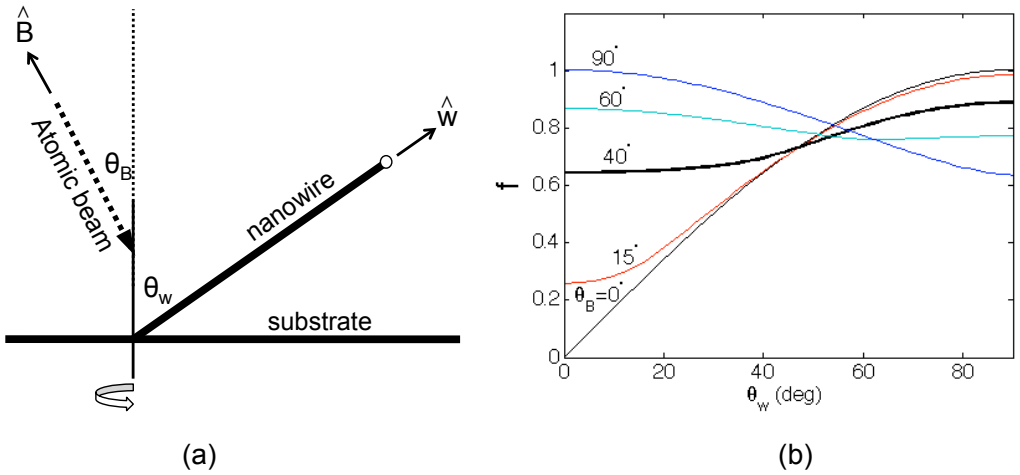

Figure 4.2: Impinging flux on tilted nanowires. (a) Schematic showing the beam flux and nanowire orientations. (b) Fraction f corresponding to the magnitude of the molecular beams intercepted by the nanowire surface; the calculation takes into account the nanowire tilt angle θ_w the flux beam angle θ_B. The factor f is furthermore averaged over a 2π rotation of the nanowire about the substrate normal. An angle $\theta_B = 40°$ corresponds to our experimental setting for the Zn effusion cell.

magnitude of the flux, through the flux angle with respect to the substrate such that $R = R_s/cos(\theta_B)$. The sidewall impingement R_w is related to total flux such that $R_w = \frac{f}{\pi}R$, where the factor f accounts for tilt with respect to the flux beam, and also for the rotation of the substrate; the factor of $\frac{1}{\pi}$ reflects the effective exposure of only the cross-section of the nanowire (cut along the height). Factor f is calculated as

$$f(\theta_B, \theta_w) = \frac{1}{2\pi}\int_0^{2\pi}\sqrt{||\hat{B}\times\hat{w}||^2}d\phi \tag{4.10}$$

where

$$\hat{B} = \Big(0, \sin(\theta_B), \cos(\theta_B)\Big), \qquad \hat{w} = \Big(\sin(\theta_w)\cos(\phi), \sin(\theta_w)\sin(\phi), \cos(\theta_w)\Big) \tag{4.11}$$

and where $\hat{B}$ and $\hat{w}$ are unit vectors pointing in the direction of the flux beam and nanowire respectively. The magnitude of f is shown in figure 4.2b. Finally we have

$$R_{top} = \frac{f(\theta_B, \frac{\pi}{2} - \theta_w)}{2}R \tag{4.12}$$

considering a catalyst cross-sectional plane normal to the nanowire sidewalls. We can synthesize the nanowire growth rate in the following form:

$$\frac{dL}{dt} = \frac{2\Omega R\lambda_w f(\theta_B, \theta_w)}{\pi r_w}\tanh(L/\lambda_w) - \frac{2\Omega J_{sw}}{r_w\cosh(L/\lambda_w)} + \Omega R f(\theta_B, \frac{\pi}{2} - \theta_w). \tag{4.13}$$

The model as it is presented depends on variables Ω, R_s, θ_B and θ_w. We can assume that the nanowire crystal is essentially zinc blende, giving us $\Omega = \frac{1}{8}a^3_{ZnSe}$. The value of θ_B is fixed by the

experimental MBE setup (in our case $\theta_B = 40°$ for the Zn effusion cell), and θ_w can be measured from SEM images of nanowire samples. Finally R_s can be directly obtained from measurements of the ZnSe 2D layer growth rate, $\frac{dH}{dt}$, such as shown in figure 3.3. We therefore have $R_s = \frac{1}{\Omega}\frac{dH}{dt}$. We assume that the sticking coefficient is the same on the nanowire sidewalls and on the substrate surface.

Note that the cylidrical coordinates are still valid in the diffusion model presented even if the nanowire is tilted as long as (i) we take into account the the proposed adjustment to R_w, with the assumption that the exposition of only one side of the nanowire does not significantly affect the requirement of surface concentration steady-state (quick diffusion of adatoms around the sidewalls); (ii) r_w is small compared with L.

4.3 Effect of Nanowire Growth on Surrounding 2D Layer

We note that all samples synthesized with exposure to continuous fluxes show depressions, or craters at the base of all nanowires. It is believed that there are two separate causes for these craters to appear. One reason is that the paths of the fluxes are inclined by 14° with respect to the sample normal, and nanowires can therefore shadow these fluxes. This affects the growth of the surrounding 2D layer at only specific angles. This effect is clearly visible in figure 4.3 with a sample that was not rotated in front of the fluxes. For our studies we tried to eliminate the shadowing, and obtain a more isotropic exposure of the samples to atomic flux by rotating the sample, whenever possible (figures 4.3b and c).

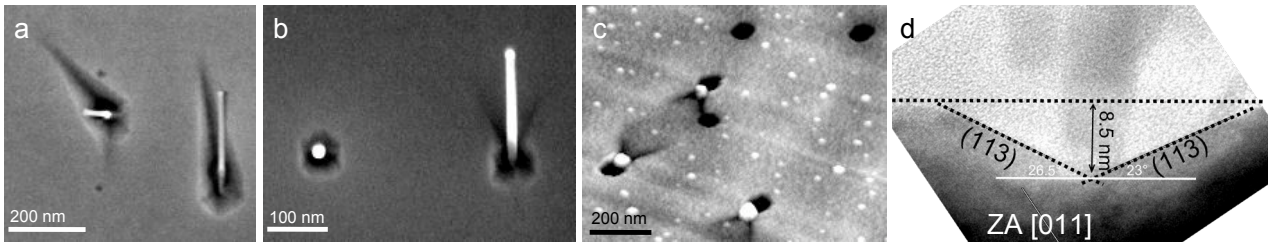

Figure 4.3: Effects observed on the 2D layer due to the presence of nanowires. (a) Top-view SEM image of elongated pits caused by a shadowing of the flux beams by nanowires in a sample not rotated in front of the flux beams. (b) Reduction or complete elimination of elongated pits when sample is rotated. Craters at the nanowire base are independant of shadowing and most likely linked to finite diffusion of species on the 2D layer. (c) AFM topograph of rotated sample in (b), further evidencing the effect of the nanowire on the 2D layer. (d) Cross-sectional TEM view of crater at nanowire base found in rotated sample at the end of 15 min of growth; the exposed facets are roughly (113) planes .

In figure 4.3b we see that for rotated samples the shadowing no longer influences the 2D surface growth around vertically growing nanowires, but it is still visible at inclined nanowires where the effect is averaged over the rotation. This is also evidenced in the AFM topograph in figure 4.3c of ZnSe 2D layer at the vicinity of nanowire sites. To produce this topograph the nanowires were removed to preserve the AFM tip.

The second cause for the craters to appear is the appearance of slow growing facets on the 2D

layer at the nanowire base. Measurements of the tilting angles of these facets by TEM indicates that they are higher indexed planes, usually (113), (114) and (115) oriented surfaces. We believe that these facets emerge because of a depletion of the adatoms on the substrate near the base of the nanowires. Adatoms migrate to the nanowire base and up the nanowire sidewalls, with a net flow of adatoms transiting up the sidewalls rather than flowing from the nanowire sidewalls to the substrate. The facets expand as the 2D layer grows thicker during nanowire synthesis, which causes the diameter of the craters to appear larger as the nanowires are grown for longer times.

Note that when the nanowires are grown in atomic layer epitaxy mode (ALE), there is no evidence of craters at the nanowire base (see section 4.9).

4.4 Influence of Nanowire Surface Density

By varying the amount of gold deposited on the surface for nucleation of catalyst nanoparticles we are able to play with the surface density of nanowires, σ_{NW}. In doing so it should be possible to modify the nanowire growth rate: when nanowires are sparse there are more adatoms from the 2D layer to be collected by each nanowire than when the nanowires are densely packed, and therefore nanowires in low density samples should grow faster than high density samples. Larger nanowire on nanowire shadowing takes place in denser samples.

When the surface density of nanowires is so high that the feeding zone of neighboring wires intersect, it is referred to as a "competitive" growth mode, and otherwise it is said to be non-competitive, or saturated. The feeding zone extends effectively by one diffusion length, λ_s, away from the nanowire base on the substrate surface. Competitive growth modes due to variation in nanowire surface densities have been demonstrated by Borgstrom et al. [56] in the MOVPE synthesis of GaP nanowires, and also by Jensen et al. [68] in the CBE synthesis of InAs nanowires. In both of these experiments, the locations and diameters of gold catalysts were defined by electron beam lithography, which helps to disambiguously attibute a variation in growth rate to variations in nanowire surface density and not to a variation in nanowire diameter. In our knowledge there is no report in the literature of competitive growth modes in nanowires synthesized by MBE.

Let's examine the results we obtained from four samples, with σ_{NW} ranging from 4.3 μm^{-2} to 167 μm^{-2}, and otherwise synthesized in identical conditions with a growth time of 15 minutes. In the SEM images in figure 4.4 we note that for the three samples with highest surface densities the nanowires are randomly oriented and are not straight, showing sometimes multiple kinks along their lengths. The craters at the base of the nanowires are not regularly shaped and they often merge with the craters of neighboring nanowires. Clearly if the craters are indicative a zone partly depleted from adatoms then the flow of adatoms collected from the substrate by nanowires in a densely packed sample will be lower than in a low density sample, and moreover it will not be isotropic and will strongly depend on the proximity and location of neighboring nanowires. In this scenario the local environment of a nanowire plays a role in determining its growth rate.

We investigated the relationship of the growth rate with respect to the nanowire surface density by measuring the length of the nanowires for each sample from the SEM images, taking into account only the nanowires that were most inclined with respect to the substrate normal, and dividing by

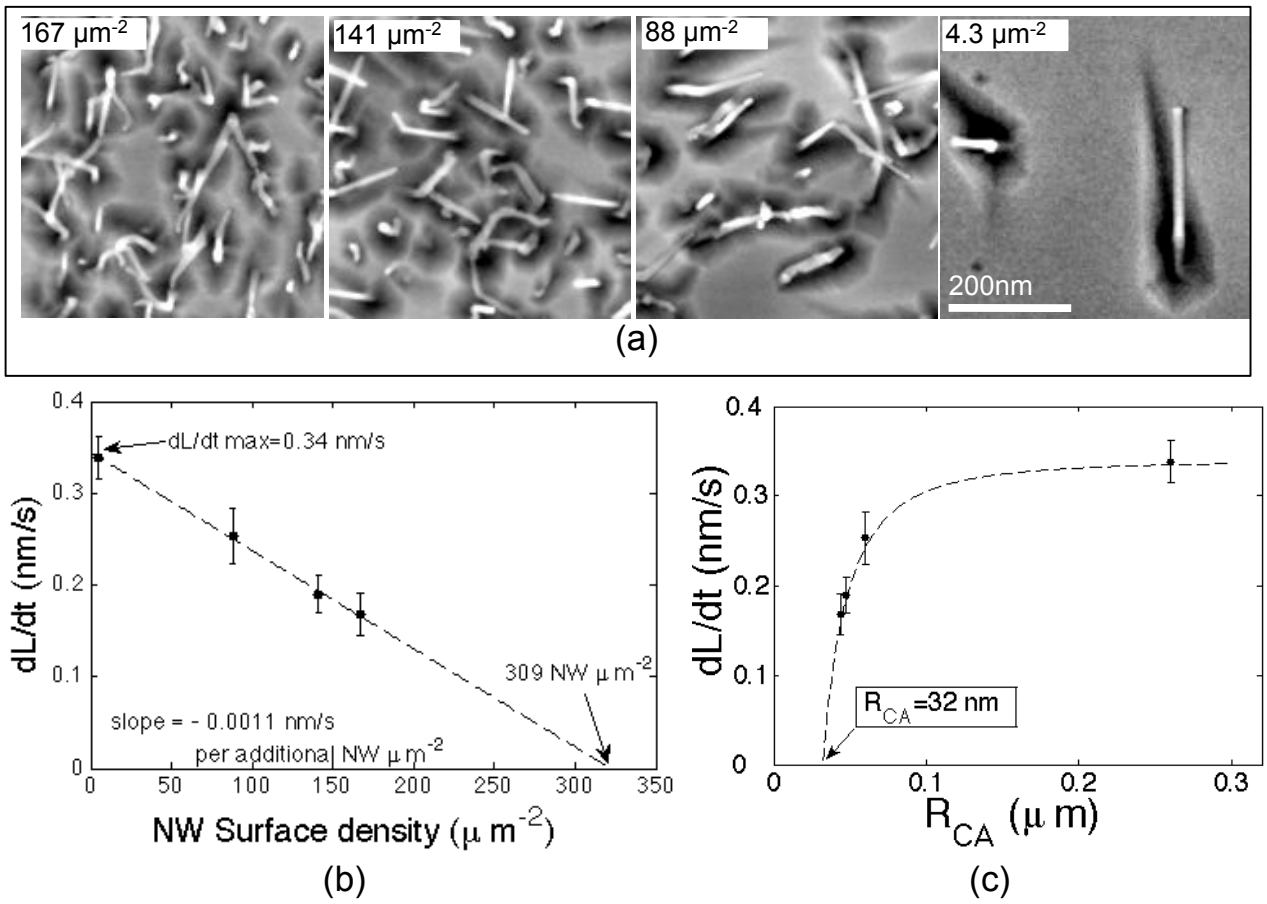

Figure 4.4: Nanowire growth rate vs surface density suggesting a competition effect. (a) Top-view SEM images of ZnSe nanowires with samples of varying nanowire surface densities (directional shadowing of the wires on the 2D layer is observed because these samples were not rotated with respect to the flux beams during growth); all images are on the same scale. (b) Average nanowire growth rate $\frac{dL}{dt}$ vs surface density of nanowires σ_{NW} from measurements on SEM top-view images of samples shown in (a). The average is over time and over observation of the lengths of many wires. (c) Same plot as (b) but with the x-axis transformed to reflect the average nanowire capture radius R_{CA} (such that the average interwire distance is equal to $2R_{CA}$).

the growth time of 15 minutes. Indeed when we measure nanowire lengths on top view images what we are really measuring is the projected length against the substrate. A total of 8 wire lengths were measured for each sample so as to find an average over nanowire lengths and length projections due to varying tilt angles. From the graph in figure 4.4a we see that $\frac{dL_{NW}}{dt}$ is proportional to σ_{NW}. The average growth rate decreases from 0.34±0.02 nm/s to 0.17±0.02 nm/s for σ_{NW} ranging from 4.3 µm^{-2} to 167 µm^{-2}, where the error indicates one standard deviation. The slope indicates a reduction in the average growth rate of 0.0011 nm/s for σ_{NW} increased by 1 µm^{-2}. The y-axis intercept indicates that $\frac{dL_{NW}}{dt}$ reaches a maximum value of 0.34 nm/s when the nanowires are infinitely separated. The x-intercept indicates that at a critical surface density σ_{NW} = 309 µm^{-2} (corresponding to an interwire distance of ~60 nm) the growth rate goes to zero. This is just an extrapolation and we lack a large surface density sample to verify the true behavior of the graph. For the sake of attempting an explanation, the intercept could be interpreted as the density at which the shadowing effect of the nanowires would become so large that it would prevent the flux from impinging on the substrate surface: if one or both of the species diffuses mainly to the nanowire growth front from the substrate surface then at this point the growth would indeed be zero (or at most equal to the 2D substrate growth).

The average surface area per nanowire is $\frac{1}{\sigma_{NW}}$, and assuming each area to be circular the collection radius for each nanowire is

$$R_{CA} = \frac{1}{\sqrt{\sigma_{NW}\pi}} \tag{4.14}$$

and therefore

$$\frac{dL}{dt} = a - \frac{b}{\pi R_{CA}^2} \tag{4.15}$$

where a = 0.34 nm/s, b = −0.0011 nm/s/µm^2 and R_{CA} is in µm. The average distance between a nanowire and any of its nearest neighbours is therefore $2R_{CA}$. We can transform the x-axis of the graph in figure 4.4b to reflect what the surface density of nanowires means in terms of collection radius. From the graph in figure 4.4c we see that the relation between $\frac{dL_{NW}}{dt}$ and R_{CA} begins to taper to reach the 0.34 nm/s assymptotic maximal growth rate at around R_{CA} = 100 nm (at σ_{NW} = 32 µm^{-2}).

Separating the nanowires beyond 200 nm (R_{CA} =~100 nm) only incrementally increases the growth rate. When the separation between neighboring nanowires is lower than 200 nm, $\frac{dL_{NW}}{dt}$ decreases rapidly and reaches zero at $R_{CA} = 32nm$, corresponding to the previously mentioned critical density of σ_{NW} = 309 µm^{-2}. A capture radius R_{CA}=100 nm could be indicative of the diffusion length λ_s of at least one of the adatom species, Zn or Se, on the substrate (001) surface. According to Gaines [69], the slowest diffusing species between Zn and Se is Zn, and he reports a diffusion length for Zn of 4 nm on the (001) surface of ZnSe for substrate temperatures below 460°C. Since this length is much lower than 100 nm, we could potentially be looking at a diffusion linked to Se.

Another possibility is that R_{CA}=100 nm is the distance away from the base of the nanowires within which the reflection of the fluxes on the flat 2D layer can be captured efficiently by the

nanowire sidewalls. In our knowledge this factor is never discussed the literature, probably because MBE is a growth technique used mainly for synthesis of thin films. In thin film growth wether or not a flux beam can get reflected off of the surface, through elastic collision for instance, is of no importance. According to Riley et al. [70] the sticking coefficient of Zn on a (001) ZnSe surface is 0.36 at 400°C, meaning that only a third of the Zn atoms striking the 2D surface will incorporate the growing crystal. A fraction of the remaining atoms in the flux beam could simply collide elastically with the surface and be reflected, or desorb from the surface in a direction other than normal to the substrate, and potentially be captured by the nanowire sidewalls.

From literature, we know that in MBE the growth rate of nanowires increases with decreasing r like $\frac{1}{r^n}$ where n is usually a number between 1 and 2. So we must pay attention to the nanowire radii as a function of σ_{NW}. As we we will see in the next section, the lower σ_{NW}, the higher the average nanowire radius. Therefore even if we assume that the nanowire growth rate is inversely proportion to r^n, the conclusion of the existence of a competitive mode still holds (in fact the graph in figure 4.4b would appear even steeper).

The observed saturation of the growth rate at low σ_{NW} could be a limitation intrinsic to the mechanism of incorporation of adatoms into the nanowire crystal at the growth front. In that scenario an increase in the flow of species to the growth front would not increase the growth rate. If this were the case then it would be difficult to differentiate from reaching a maximal value in adatom influx. A possible experiment to differentiate the two possible cases would be to observe the behavior of the saturated growth rate as a function of total flux.

Even if we are observing a limitation due to nucleation mechanism, that mechanism would be evidenced only because of an increased flow of matter to the growth front due to increased inter-wire seperation. Therefore, the experimental results that we discuss above still tend to indicate a competitive growth mode.

4.5 Nanowire Radii and Crystalline Structures

Here we present a set of TEM characterizations that inform us on both the accurate nanowire diameters and their crystalline structure.

Figure 4.5 and 4.6 shows HRTEM images of nanowires grown on samples with three different surface densities of catalyst particles, σ_{NW}. In the sample with highest surface density, 182 μm^{-2}, typical nanowires grow in random orientations and have many kinks along their lengths (figure 4.5d). All the wires characterized on this sample have a cubic crystalline structure at the base, with multiple defects. These defects can cause the wires to kink, like the example seen in figure 4.5a. Also in this figure, given the width of the elbow compared to the nanowire diameter at locations above and below the elbow, it appears likely that some of the defects could have extended along the growth direction, therefore intersecting the growth front. Further along their lengths, the wires either conserve a cubic structure through to the catalyst tip, like for instance in figure 4.5b where we note a cubic (111) crystal along the growth axis; or the wires transform to the hexagonal structure with the growth axis in the hexagonal c-direction, like in figure 4.5c. Finally, based on the characterization of six nanowires from this sample we find a mean nanowire diameter of 9.0 ± 1.1 nm, with the measurements

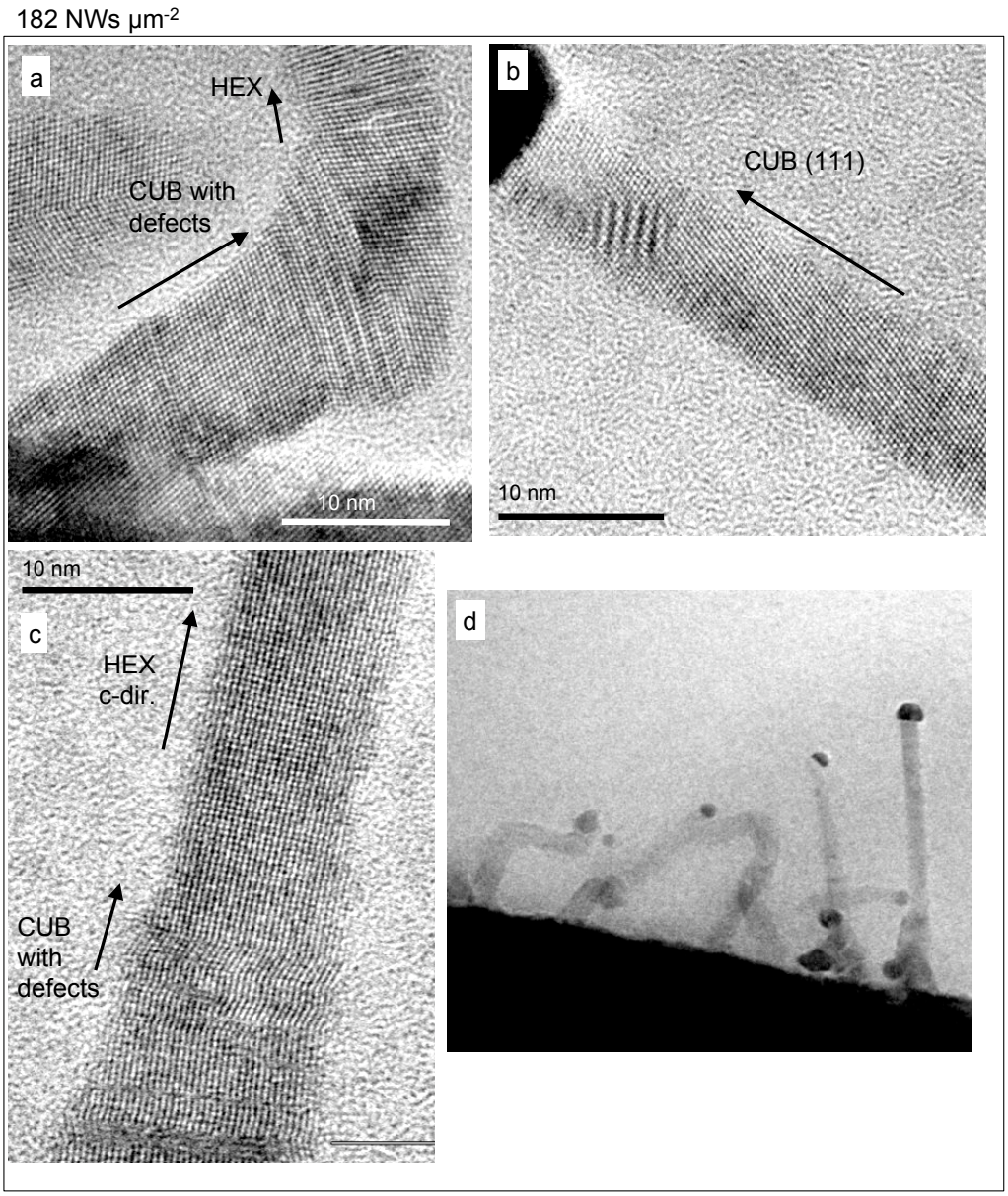

Figure 4.5: HRTEM images of ZnSe nanowires grown in identical conditions except for varying surface densities. (a)-(c) Images showing typical crystal structure characteristics found in a sample with σ_{NW} = 182 NW µm^{-2}; (d) TEM view of an ensemble of nanowires from this sample.

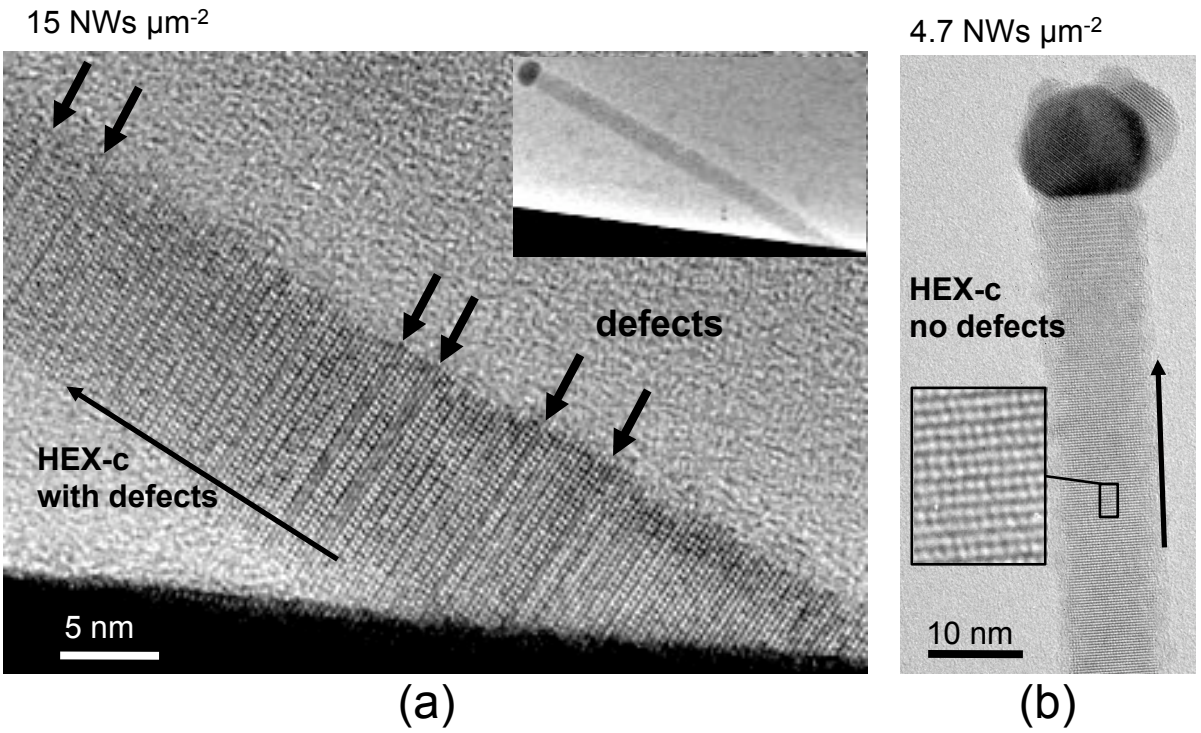

Figure 4.6: HRTEM images of ZnSe nanowires grown in identical conditions except for varying surface densities. Images showing typical crystal structure characteristics found in a sample with (a) σ_{NW} = 15 NW µm^{-2} and (b) σ_{NW} = 4.7 NW µm^{-2}.

were on straight segments of the nanowires away from elbows.

Figures 4.6 shows typical HRTEM images of nanowires in samples with lower surface densities. These nanowires are completely straight. In the case of the nanowire shown for σ_{NW} = 15 µm^{-2} in figure 4.6a, the crystal structure is over 90% hexagonal, with the growth axis along the c-direction, and the only visible defects are occasional stacking faults or short cubic (111) sections. From the inset of figure 4.6a we can note the high homogeneity in the diameter along the nanowire length, indicative of a zero radial growth rate. In the case of the nanowire shown for σ_{NW} = 4.7 µm^{-2} in figure 4.6b, the crystal structure is entirely hexagonal without defects. Based on measurements of seven and five nanowires respectively, the mean nanowire diameter is 10.0 ± 1.1 nm for the sample with σ_{NW} = 15 µm^{-2} and 12.2 ± 1.2 nm for the sample with σ_{NW} = 4.7 µm^{-2}.

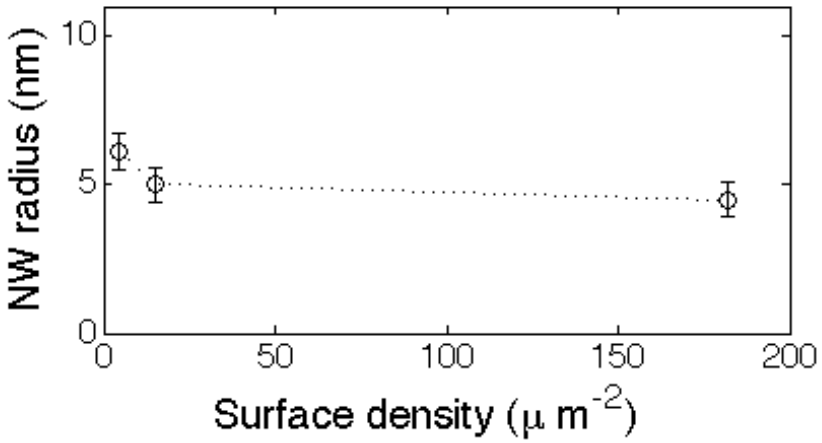

Figure 4.7: Nanowire radii vs nanowire surface density σ_{NW}. Nanowire radii measured from TEM images decrease slightly with σ_{NW}.

Figure 4.7 shows a rather weak dependence of the nanowire radii on the surface density.

4.6 Nanowire Orientation and Influence on Length

In the low surface density sample (4.7 µm^{-2}) shown in figure 4.8, the nanowires are widely separated and the depressions at their base do not merge. We notice that the nanowires are generally straight, showing two specific growth orientations with respect to the substrate. On average 65% of the nanowires grow in the direction inclined to the substrate with an orientation close to (111)B; 35% grow in a direction normal to the substrate with sometimes a slight tilt up to around 20° toward the (111)A direction. Cai et al. [29] who also grew ZnSe nanowires by MBE but directly on GaAs (001) substrates, observed wires growing in both (111)A and (111)B directions, in growth conditions similar to ours (390°C and 10 nm diameter), but by using a ZnSe compound cell. Other common growth directions observed by Cai were ⟨110⟩ and ⟨112⟩, on (001) and (011) GaAs substrates.

The SEM images in figure 4.9 are taken in the [110]/[-1-10] zone axis, perpendicular to the growth plane of the nanowires tilted towards (111)B. The images belong to two different samples grown in identical conditions, except for total growth time. Upon analyzing the images (see the summary of measurements in table 4.1 we first notice that the angle of inclined nanowires is shallower than the

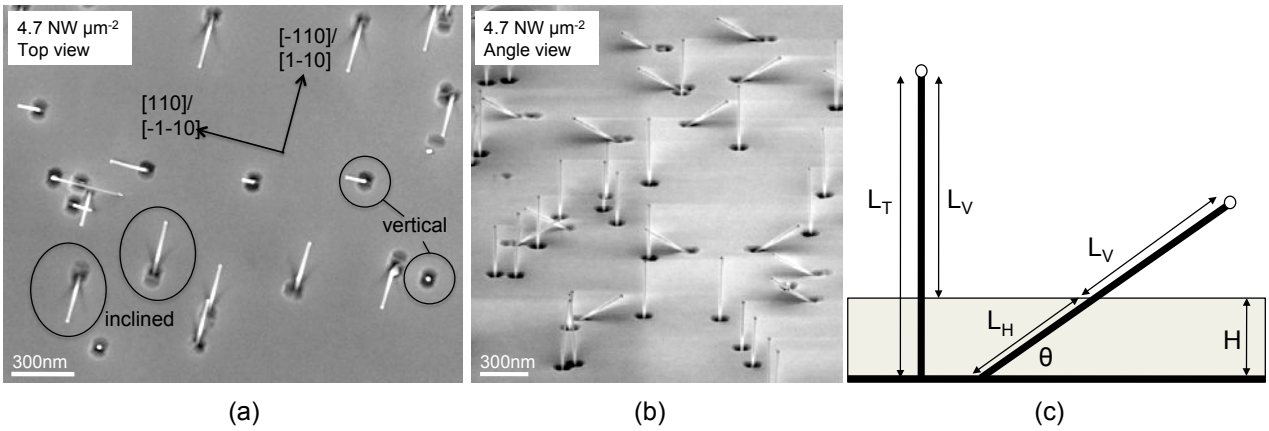

Figure 4.8: (a)Top-view, and (b) inclined view SEM images showing the two general growth orientation of nanowires on (001) substrate. (c) The schematic depicts how part of the nanowires remains buried in the substrate layer of thickness H that concomitantly grew with the nanowires. L_V, L_H and L_T correspond respectively to the visible, buried and total lengths.

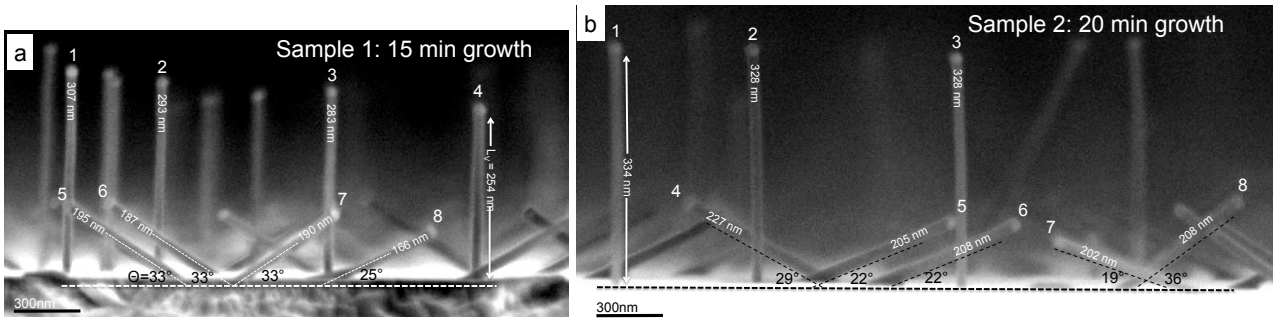

Figure 4.9: Side-vew SEM in the [110]/[-1-10] zone axis. Images of two samples used to obtain statistics on nanowire lengths.

(111) angle of 35.3° with respect to the substrate surface. In figure 4.9a the average tilt is $31 \pm 4°$, whereas in figure 4.9b it is $25 \pm 7°$, which shows that the tilt angle can vary between samples or even maybe between locations on the same sample. The overall average nanowire tilt in these figures is $28 \pm 6°$. Secondly we notice that the inclined nanowires appear shorter than the vertical ones. As depicted in figure 4.8c, as the ZnSe thin film continues to grow at the same time as the nanowires, it buries part of the nanowires, and the fraction buried is more important in the case of tilted nanowires. Based on this consideration we calculated the total length L_T of each nanowires in figure 4.9. We have

$$L_T = L_V + \frac{H}{\sin(\theta)} \tag{4.16}$$

where L_V is the visible portion of the nanowire and H is the height of the ZnSe thin film deposited while the nanowires were grown. The height H is based on the 0.0635 nm/s growth rate of the 2D layer at 410°C measured previously (see figure 3.3). The nanowires growing normal to the substrate have a mean growth rate of 0.36 ± 0.03 nm/s and the inclined nanowires have a 9% lower average growth rate of 0.33 ± 0.02 nm/s. These two growth rates are very close. Based on these numbers we also determine the ratio of growth rates of nanowires over the 2D layer to be 5.4.

Table 4.1: Growth rate vs tilt angle for observations on figure 4.9. L_T is obtained from eq. 4.16.

Sample 1: 15 min growth					Sample 2: 20 min growth				
NW	θ	L_V (nm)	L_T (nm)	$\dot{L}(t)$ (nm/s)	NW	θ	L_V (nm)	L_T (nm)	$\dot{L}(t)$ (nm/s)
1	90°	307	364	0.405	1	90°	334	410	0.342
2	90°	293	350	0.389	2	90°	328	404	0.337
3	90°	283	340	0.378	3	90°	328	404	0.337
4	90°	254	311	0.346	4	29°	227	384	0.320
5	33°	195	300	0.333	5	22°	205	408	0.340
6	33°	187	292	0.324	6	22°	208	411	0.343
7	33°	190	295	0.328	7	19°	202	436	0.363
8	25°	166	301	0.335	8	36°	208	338	0.281

4.7 Nanowire Length as a Function of Time

The nanowire lengths that we measured, as we did so far, on the images of the completed samples can only inform us on the average growth rate. We cannot know from this information alone how the growth rate evolved over time during the growth process. In order to shed light on this question we synthesized five nanowire samples where each sample differed only by its total growth time. All other conditions were kept constant, with a substrate temperature of 410°C and a flux ratio Se:Zn of 3. The surface density for these samples was contained in the range 1.1 to 21.6 μm^{-2}, so in a surface density regime where the nanowire growth is not competitive. (Although we did our best to reproduce surface densities below 4 μm^{-2}, the mean density we ended up achieving was 9.1 ± 9.1

μm^{-2}; the large error associated with the mean density shows that the process of generating catalytic nanoparticles at a low surface density is delicate and difficult to control)

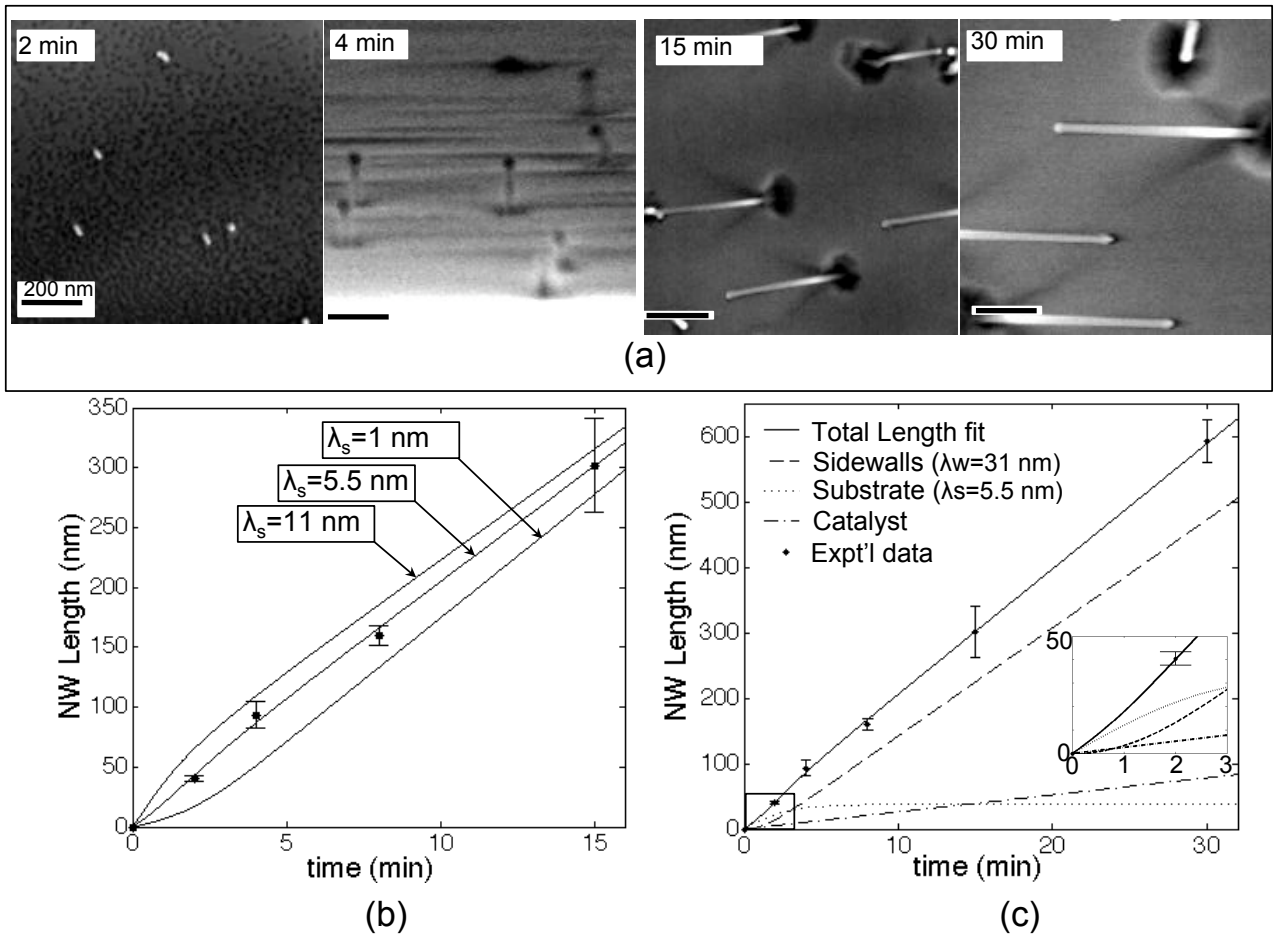

Figure 4.10: Nanowire length vs growth time. (a) SEM images showing samples with growth times from 2 to 30 minutes (scale bars are 200 nm). (b) Nanowire length plotted vs growth time from 0 to 15 minutes, roughly fitted with the mass-transport model of Johansson et al. [67] by varying the diffusion lengths of species on the substrate (λ_s) and nanowire side wall (λ_w). We assume that Zn and Se have the same diffusion lengths. The best fit corresponds to λ_s = 5.5 nm and λ_w = 31 nm. (c) Same data points as in (b) with the solid line showing the best fit, up to 30 minutes of growth. The broken curves show the contribution to the total length from adatoms that impinged on the catalyst, substrate and sidewalls, as a function of time. Inset of (c) shows a zoom of the graph over the 1st 3 minutes of growth.

We synthesized samples with growth times of 2, 4, 8, 15 and 30 minutes. SEM images of these samples are shown in figure 4.10a. The nanowire lengths were measured directly on the SEM images from top-down views (not all shown). We measured only the inclined type of nanowires. It was assumed that their average tilt angle was 28°, as was determined in the previous section. With this assumption and the expected height H of the 2D layer deposited during the different growth times (2D growth rate of 0.0635 nm/s – see figure 3.3), eq. 4.16 was used to find the total length L_T for each growth time (which includes the length portion of the nanowire buried under the 2D layer).

The plots in figure 4.10b-c show the values of L_T as a function of time. The solid curves for the nanowire length are calculated from the mass-transport model presented in section 4.2, by integrating the growth rate eq. 4.13, which we recall here:

$$\frac{dL}{dt} = \frac{2\Omega R \lambda_w f(\theta_B, \theta_w)}{\pi r_w} \tanh(L/\lambda_w) - \frac{2\Omega J_{sw}}{r_w \cosh(L/\lambda_w)} + \Omega R f(\theta_B, \frac{\pi}{2} - \theta_w). \tag{4.17}$$

Only two parameters, diffusion lengths λ_s (substrate) and λ_w (sidewalls), were left free to be adjusted for best fits, whereas the rest of the parameters were set as follows: r_w = 5nm (the nanowire radius), R = 3.64 $\mathrm{nm^{-2}s^{-1}}$ (flux magnitude), Ω = 0.0228 $\mathrm{nm^3}$ (atomic volume in the ZnSe crystal), J_{sw} = −22.50 $\mathrm{nm^{-1}s^{-1}}$ (solution derived from mass-transport model - refer to section 4.2), θ_B = 40° (flux tilt with respect to substrate normal), θ_w = 62° (nanowire tilt with respect to substrate normal), $f(40°, 62°)$ = 0.816 (geometrical factor associated with nanowire tilt) and $f(40°, 28°)$ = 0.663 (geometrical factor associated with catalyst tilt). Note that our fitting routine does not take into account the reduction in the exposed sidewall area as a function of time due to a gradual burying of the nanowire foot in the 2D layer; however this factor is not expected to affect the value of fitted parameters considerably given the fact that the nanowire growth rate is more than five times greater than that of the 2D layer. The diffusion lengths of Zn and Se are assumed to be equal to the those of the slowest diffusing atoms, i.e. Zn in this case [69].

Figure 4.10b shows a close-up of the growth over the first 15 minutes. The beginning of growth is affected by both λ_s and λ_w until the nanowire length L is approximately equal to λ_w. Up to then adatoms originating from both substrate and sidewall impingement contribute to the growth. When $L > \lambda_w$ the adatoms diffusing from the substrate no longer reach the growth front. Since we do not observe tapering of the nanowire, we conclude that there is no radial growth, and that the adatoms that do not reach the growth front simply desorb from the sidewalls. Three model curves are shown in figure 4.10b where the value of λ_s is set at either 1, 5.5 or 11 nm. The value of λ_w was optimized for each of the model curves to obtain a best fit of all data points up to 30 minutes of growth. The value of λ_w for all three curves was contained in the range 29.5 to 33.5 nm. Clearly the best fit is given by λ_s = 5.5 nm with λ_w = 31 nm. Gaines et al. [69] reports an upper value of 4 nm for the diffusion length of Zn on ZnSe (001) during growth temperatures below 460°C and a flux ratio Se:Zn=2. The discrepancy between our value and that of Gaines could be explained by the fact that differently oriented facets grow at the base of the nanowires. These facets grow slower than the (001) surface, causing craters instead of mounds to appear. Therefore these facets exhibit longer diffusion lengths, and this could account for the larger value of λ_s that we obtain from the model fit.

Figure 4.10c shows the best model fit for data up to 30 minutes of growth. The broken curves show the individual contributions to the total nanowire length from adatoms impinging either on the substrate, the nanowire sidewalls or the catalyst. Substrate-diffusing adatoms contribute to the growth only during the first 2 minutes, that is until the nanowire length reaches λ_w. Therefore the contribution from the substrate quickly saturates. Sidewall impingement starts shortly after the beginning of growth and its contribution becomes linear after L becomes longer than λ_w. It also heavily dominates the adatom contributions to the nanowire crystal growth. Contribution from catalyst impingement is linear at all times but accounts for only ~10% of the nanowire length at any

point in time.

4.8 Influence of Growth Temperature and Flux Ratio

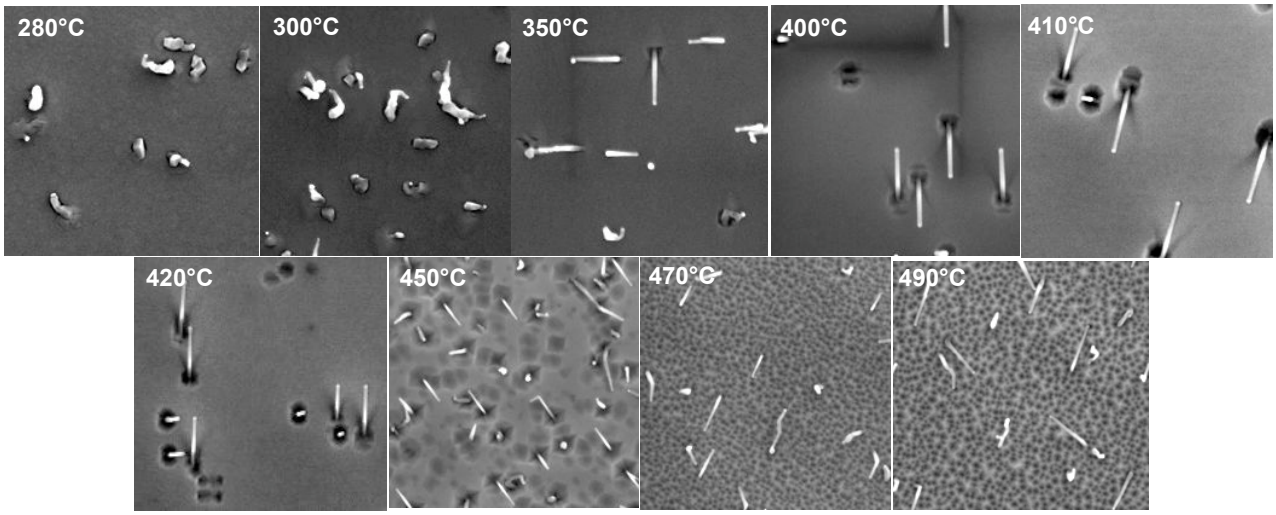

Figure 4.11: SEM top-view images showing nanowires grown at various temperatures.

Here we observe the influence of temperature on nanowire growth. A total of 9 samples were synthesized with temperatures ranging from 280°C (the temperature for optimal 2D layer growth) to 490°C. All other parameters were kept constant, the flux ratio was Se:Zn=4, and the total growth time was 15 minutes. To generate the graph of growth rate ($\frac{dL}{dt}$) vs T in figure 4.12 we measured the nanowires lengths directly on the SEM top views and used eq. 4.16 to obtain the nanowire total lengths L_T, using the 2D layer growth rates as a function of temperature presented in figure 3.3. Again only tilted nanowires were measured on the top view images. The average tilt is taken to be 28° with respect to the substrate surface. This assumption is obviously only accurate for samples between 400°C and 420°C where nanowire grow along regular orientations (see figure 4.11), but it is also a good enough assumption for all other temperatures for the purpose of a qualitative analysis. The growth rate was obtained by dividing the average L_T at each temperature by the total growth time. Error bars indicate one standard deviation.

Nanowires do not show the same characteristics at all growth temperatures. Below 350°C they are tapered with a base diameter around 65 nm and a tip of the same dimension as the catalyst (~10 nm). Tapering is indicative of radial growth at the sidewall. Tapering of ZnSe nanowires is generally observed for low temperature growth by MBE [30]. Craters appear at the base of the nanowires starting at 350°C growth, which is also when the nanowires appear to grow without kinking. Craters could appear therefore following a significant increase of the sidewall diffusion length, which would allow adatoms at the base of the nanowire to be efficiently evacuated by diffusion up the nanowire sides; a longer diffusion length also brings a faster flow of adatoms to the growth front which can explain the notable increase in the growth rate starting at 350°C, as seen in the graph in figure 4.12. The growth rate reaches a maximum at around 410°C. The same type of graph showing a maximum

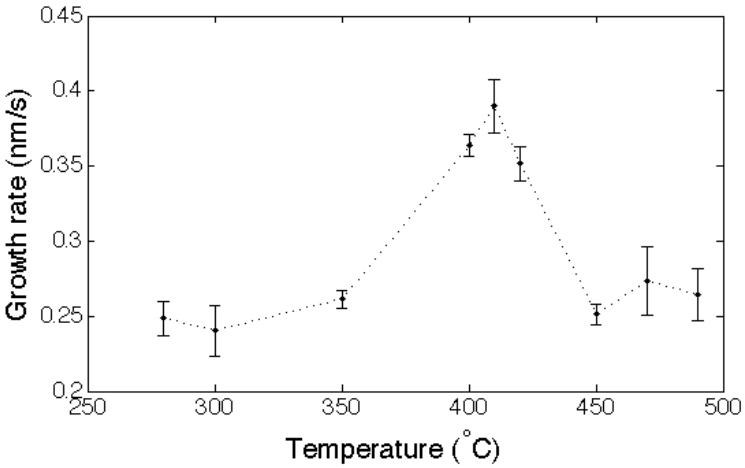

Figure 4.12: Average nanowire growth rate vs growth temperature.

growth rate at a middle temperature was also observed in GaAs, GaP and InAs [71] for growth by MOVPE. Nanowires are specifically oriented along the substrate normal and close to (111)B directions for temperatures ranging from 400°C and 420°C; as we get farther on both sides of this temperature range the nanowire orientations become increasingly random. Nonetheless tapering is only observed for low temperatures - at high temperature the diameter remains homogenous, of the catalyst size, all along the wire lengths.

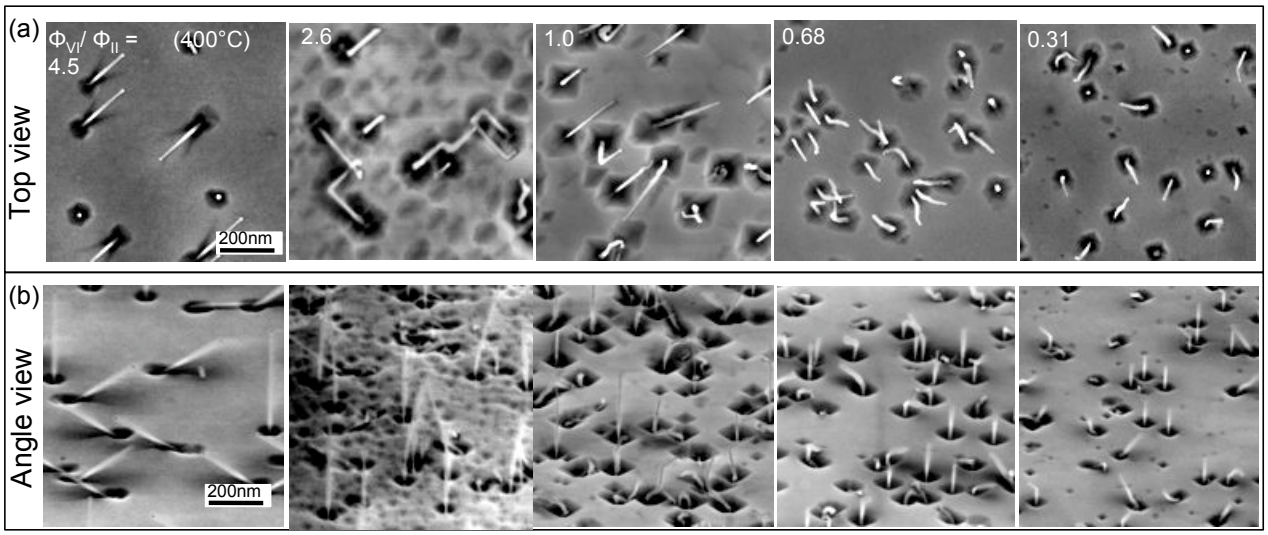

Figure 4.13: SEM images of nanowires grown under different Se:Zn flux ratios. The scale bar is identical for all images.

We knew from studies conducted prior to the beginning of this project that a Se-rich condition was favorable for growing straight and untapered nanowires. In figure 4.13 we show nanowires grown under different flux conditions, for 15 minutes and at 400°C. We observe that the straightest and most regularly oriented nanowire grew when Se:Zn > 3 (we conclude this from observation of many

more samples than just the ones shown in figure 4.13). It looks like the BPR ratio Se:Zn ≤ 0.3 also yields straight and well oriented nanowires (mostly vertically), but with a lower growth rate than in Se-rich conditions. Further investigations would be necessary to fine tune the growth under Zn-rich conitions.

4.9 Growth by Atomic Layer Epitaxy (ALE)

Atomic layer epitaxy, or ALE, is a surface controlled and self-limiting method for deposition of binary thin films from their elemental flux beams. It allows for excellent conformality and subnanometer level accuracy in the control of film thicknesses. The ALE principal of growth consists in alternating the elemental flux beams with an appropriate dead time between the two exposures. A surface is exposed to the flux of one species for as long as it takes to saturate all available surface sites. The ALE self regulated growth rate is related to the surface stoichiometry of the two compound elements. For instance a growth rate of 0.5 ML per cycle was measured for 2D (001) ZnSe ALE growth at 280°C, related to a c(2x2) surface reconstruction under Zn flux with a coverage of half a monolayer of Zn [38].

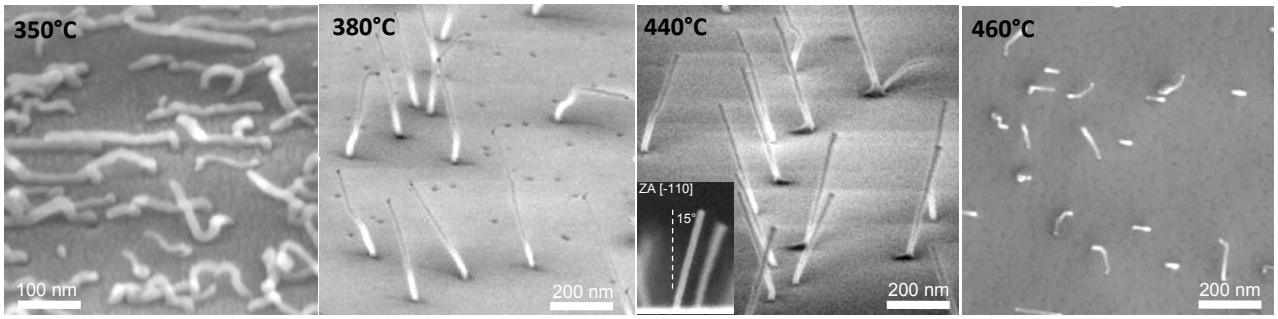

Figure 4.14: SEM images showing nanowires grown in the ALE mode at various temperatures.

In the current experiment we attempted to grow nanowires in ALE mode by alternating the fluxes of Zn and Se on the sample. Four samples were synthesized at four different growth temperatures and are shown in figure 4.14. The flux BPR was Se:Zn=4. Growth was initiated with 30 s of simultaneous exposure to both species (MBE mode), as was done previously. We know from elaboration of a test sample (not shown) that this step is not necessary to initiate the nanowire crystal nucleation, but it gives us a basis for comparison with previous experiments, as will be exposed later. After this initial step, growth followed in the ALE mode with the following beam sequence: 5 s of Zn, 5 s vacuum, 5 s of Se, 5 s vacuum. The flux exposure sequence was repeated 240 times for a total exposure time to the flux of either species of 20 minutes.

As was evidenced in the previous section, temperature plays an important role in determining the general aspect and orientation of the nanowires. At the lowest investigated growth temperature of 350°, the nanowires are not tapered, have a large density of kinks, and show the interesting particularity of growing in a crawling manner along the substrate, always in the [-110]/[1-10] directions. As the temperature is increased up to 440°C the nanowires become free standing, grow straight

and adopt only one specific growth orientation (with two symmetric directions with respect to the substrate, as seen in figure 4.14c. As the temperature is increased to 460°C the nanowire orientation starts to become random, as seen in the top-down SEM image in figure 4.14d.

In figure 4.15 we compare top-down SEM images of two nanowires samples grown either in MBE or ALE modes, and which were synthesized at roughly the same temperature (410°C and 440°C respectively). We notice that each growth mode favors distinct growth orientations. Recall that in MBE mode two nanowire orientation types were observed: in the most abundant type 65% of wires grew roughly in the (111)B direction (seen pointing in the [-110]/[1-10] direction in the top-down SEM), while in the second type 35% of wires grew normal to the substrate with sometimes a slight tilt towards [110]/[-1-10]. In the ALE mode only the latter type of orientation is observed. The tilt away from the substrate normal is observed systematically on all ALE nanowires, unlike the corresponding nanowires synthesized in MBE mode. The wires in ALE mode point roughly in two symmetrical ⟨114⟩ orientations (20° tilt with respect to substrate normal). It is not clear to what extent the specific nanowire orientation can be attributed to the ALE mode, since the base part of the wires was synthesized in MBE mode. On the other hand it is clear that the initial growth orientation does not dictate the final orientation (otherwise both the MBE and ALE growth modes would have displayed the same final observable orientations). Growth mode clearly plays an important role in that matter.

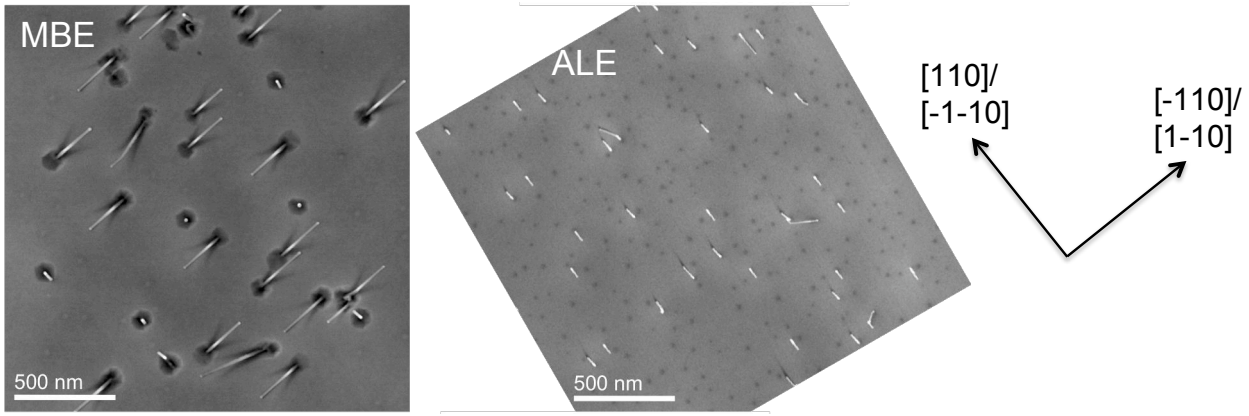

Figure 4.15: SEM top-view images of wires synthesized in MBE and ALE modes. In MBE mode the wires grow in two general orientations, but only one of these orientations is observed in ALE mode.

Figure 4.16 presents an HRTEM image of a nanowire from the sample synthesized at 440°C. As opposed to the (111)B inclined nanowires synthesized in MBE mode which were of the hexagonal wurtzite structure, this nanowire presented here has a crystal structure made up entirely of the cubic zinc blende phase. (Note that it is possible that the wires growing normal to the substrate in the MBE mode samples are also of the ZB phase, although if that were the case they would still represent a minority of the nanowires. Unfortunately we do not have a TEM characterization of those wires for comparison.) The wurtzite structure appears only as stacking fault defects on (111) planes. In the direction of its growth axis the nanowire crystal is mostly ⟨001⟩ cubic and also ⟨112⟩ cubic. The cubic ⟨001⟩ oriented crystal is not commonly observed in ZnSe nanowires and we find only one mention of

it in Wang's review [72] on nanowire crystal growth. The nanowire foot has the ⟨001⟩ orientation which strongly suggest an epitaxial relationship with the substrate.

We note that for all samples synthesized with the ALE mode and presented in figure 4.14, none of them show evidence of craters forming at the nanowire bases. We provide two possible explanations for this observation. Firstly this could be the result of the ALE growth-regulating effect on the 2D layer: upon exposure to the flux of one of the species, the entire 2D layer (including in the vicinity of the nanowires) becomes saturated with that species and it is no longer affected by the evacuation of additional adatoms as they diffuse to the NW base. Secondly, it is possible that the lack of craters stems from an inefficient growth of the 2D layer in the ALE mode at the temperatures that we are probing. To support this expanation, we draw the attention to figure 4.16f where we see a characteristic narrowing of the wire diameter at the foot of the nanowire over the first 5 to 10 nm of growth. A similar nanowire foot shape was observed by Schmidt et al. [73] on Si and was attributed to a reshaping of the catalyst at the onset of nanowire growth. As this reshaping remains visible in our TEM image it is possible therefore that only a negligible portion of the wire was buried under the concomitant growth of a 2D layer.

While we do not know exactly the growth rate of the 2D layer, we nevertheless know that a maximum of 34 nm could have been deposited from the onset of the ALE growth, if we assume that 0.5 ML is synthesized at the end of each ALE cycle. By taking the particular case of the sample synthesized at 440°C where nanowires measure 405±26 nm, we obtain a minmal growth rate ratio of nanowires over 2D layer of 12 (405 nm/34 nm). This is more than double the ratio of growth rates observed in MBE mode (5.4).

From the average wire length in the sample at 440°C we deduce that the equivalent of 6.0±0.4 ML of ZnSe are added at the nanowire growth front at each ALE cycle. (Note that the initial portion of the nanowire grown in MBE mode comprises less than 3% of the total nanowire length, so we neglected to take that portion into account in this analysis.) Because in ALE mode the fluxes are not exposing the sample simultaneously, it is clear that at least one of the species is allowed to accumulate either at the catalyst or at the nanowire sidewalls, although we tend to reject the accumulation of species at the sidewalls because of the absence of radial growth. It is common knowledge that nanowire species accumulate at the catalyst, in cases when the catalyst forms a liquid eutectic with the species (see for instance AuSi [3] or AuGa [74] liquid eutectic catalyst seeds). In those cases the atomic percentage of the species element comprising the catalyst can vary according to growth parameters. Those variations affect the chemical potential of the catalyst which in turn has a direct impact over, for instance, the rate of precipitation of the species into the nanowire crystal (i.e. the growth rate) or even the resulting crystal phase of the nanowire, as is argued by Glas [5]. Accumulation of species at the catalyst is not as evident in the case when the catalyst is solid, which is the case in our system (see chapter 5). According to the AuZn phase diagram, Zn has a maximum 30 at.% solubility in solid Au at around 400°C, whereas AuSe shows no solubility for Se at the same temperature. An AuZn solid alloy is therefore possible.

Let's calculate the quantity of the Zn that would need to be dissolved in the catalyst in order to generate 6 ML of ZnSe crystal per ALE cycle. If we take the ZnSe NW crystal to be a cylinder with 6 ML height and the catalyst to be a hemisphere, and if we assume that both have a radius

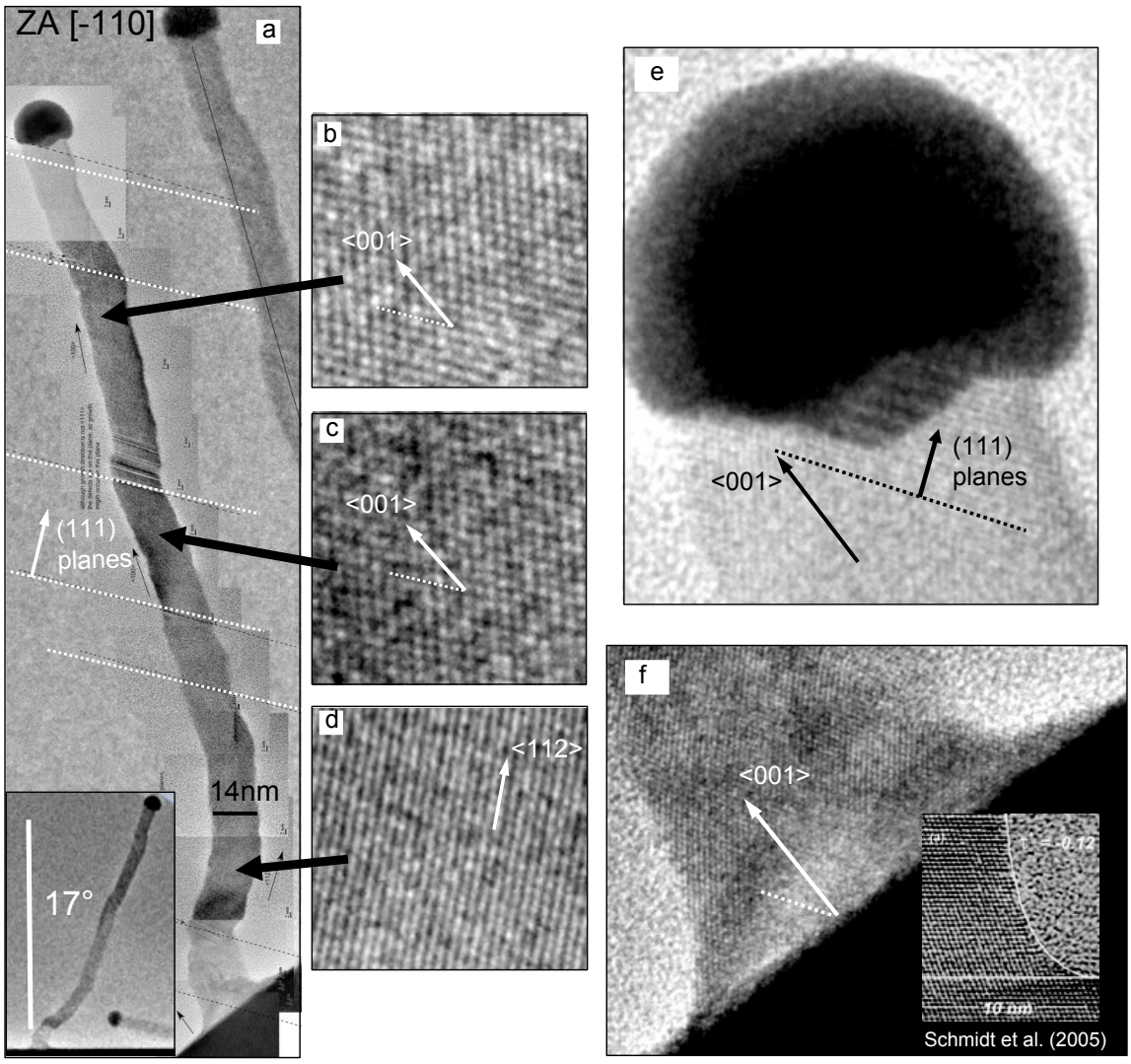

Figure 4.16: HRTEM of typical nanowire synthesized in ALE mode at 440°C. (a) Series of images showing a complete nanowire from the substrate to the catalyst. The inset shows that the wire is inclined by 17° with respect to the substrate. (b), (c) and (d) Close-ups of regions in wire (a) demonstrating that the wire phase is cubic. (e) Close-up of the catalyst with a faceted interface with the nanowire with facets oriented along the (111) direction of the wire crystal. (f) The nanowire foot shape is reminiscent of that caused by reshaping of the liquid catalyst at the onset of growth observed in MOCVD synthesis of Si nanowires (inset image [73]). Dotted lines indicate (111) planes.

of 7 nm like the radius of the wire presented in figure 4.16, then we obtain 13 at.% of Zn in gold. This is within the reported solid solubility range of Zn in Au. It is possible therefore that this much Zn accumulated in the gold catalyst at every Zn flux exposure and then got depleted at the Se flux exposure. It is possible also that more Zn accumulated in the gold seed by that only 13 at.% could be depleted during the Se flux exposure length.

Recall that the total exposure time of the nanowires to either the Zn or Se fluxes is 20 minutes. It is interesting to notice that if we take the total length of wires grown in ALE, i.e. 405 nm, and divide by 20 min, we obtain 0.34 nm/s, which is the same growth rate we found for nanowires grown in MBE mode with the same flux magnitude and BPR. This suggests that the total nanowire length depends only on the total exposure time to the fluxes, and is independant of the growth mode, with an adequate Se exposure capable of depleting the entire Zn content. It is probable that the total length will in fact remain proportional to the total exposure time to fluxes, just like it was demonstrated in section 4.7 for MBE growth, as long as the exposure time to Zn during each ALE cycle corresponds to a Zn content in gold below saturation. In the present case the saturation would occur at ~13 s of Zn (5 s×30 at.%/13 at.%). This is of course only a hypothesis since it is based on the observation of only one sample. Further studies would be interesting to conduct, like for example testing different Zn exposure times that would also reach above the gold saturation level.

4.10 Growth on (111)B Substrate

Growth of nanowires was also investigated on (111)B oriented substrates. This substrate orientation is more widely used by researchers in general because it usually yields vertically growing nanowires. In ZnSe growth this was shown to be the case by Chan et al. [75], but only nanowire over 30 nm in diameter. In our experiment growth occurred under simultaneous fluxes of Zn and Se (MBE mode) in a Se-rich condition. Four samples were synthesized with growth temperatures between 300°C and 450°C. We used a GaAs (111)B substrate to produce the samples. The substrate was first deoxidized in the III-V MBE chamber under As flux at 620°C. An epitaxial layer of GaAs (111)B was first deposited prior to an epitaxial growth of ZnSe in the II-VI chamber.

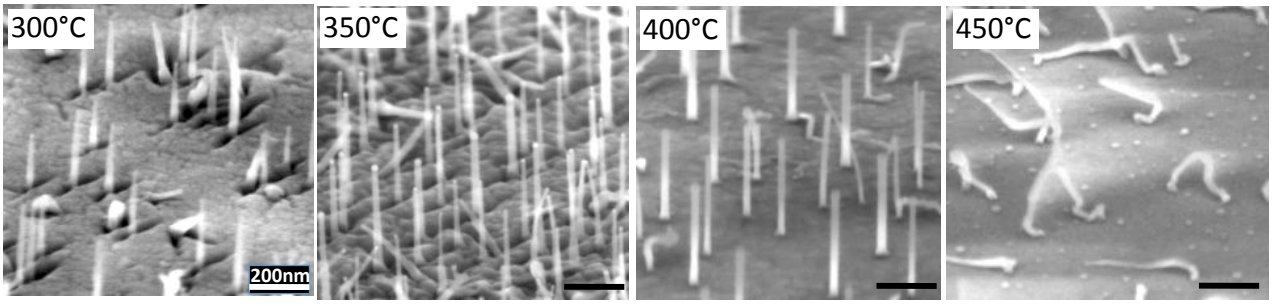

Figure 4.17: SEM images of nanowires grown on (111)B substrate for various temperatures. Scale bars are 200 nm.

Looking at figure 4.17 it appears that a majority of nanowires grow normal to the substrate up to 400°C. At 350°C it turns out that 70% of the nanowires grow normal to the substrate; the other 30%

grow in three other (111)B directions. We see this in figure 4.18a where a 120° angle separation is observable between the projections of the inclined nanowires in the top view SEM image. At 400°C about 60% of the wires grow normal to the substrate, and 40% grow in random directions. At 450°C there is no longer any observable epitaxial relationship. For comparison the vertical wires observed by Chan were grown on GaAs (111)B substrate and at the much higher temperature of 520°C. We should note though that Chan uses a ZnSe compound effusion cell.

We did not investigate the influence of nanowire surface density on (111)B substrate growths, but it does not seem to have the same affect as on the (001) substrate growths. For instance at 350°C, σ_{NW} = 136 µm^{-2} and yet all the nanowires grow perfectly straight without kinks, albeit in four different (111) orientations. On (001) substrate the nanowires only grew without kinks and in well defined crystallographic orientations when the σ_{NW} was lower than about 30 µm^{-2}. Moreover we observe trenches at the wire bases rather than the craters that we observed on (001) substrate.These trenches only appear up to 350°C, but not at the higher temperatures of 400°C and 450°C, indicating perhaps that the base layer growth was either inexistent (because the diffusion length on the (111) substrate was or the order or exceeded the average interwire distance, for instance), or that the growth was conformal to the starting smooth surface.

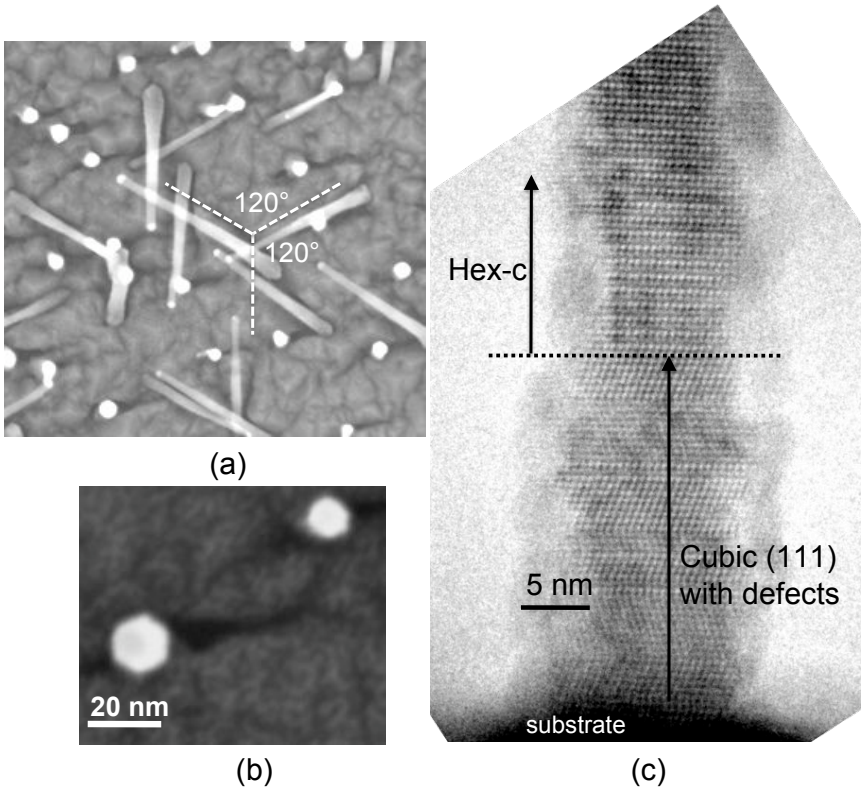

Figure 4.18: Orientation and crystal phase of nanowires grown on (111)B substrate. (a) Top-down SEM image showing that wires grow either normal to the substrate (seen as white spots), or inclined in three equivalent (111)B orientation, which we deduce from their projected angles. (b) Top-down SEM view of a nanowire with a hexagonal cross-section, suggesting six side-wall facets. (c) HRTEM showing that these wires tend to be cubic at the base before transforming to the hexagonal phase. The 3 nm amorphous layer on the nanowire surface is caused by exposure to the TEM beam.

The crystal structure of one of the vertically growing nanowires can be see in the HRTEM image in figure 4.18c. The bottom 22 nm of the wire is composed of segments of cubic (111) crystal separated by twin defect boundaries. At 22 nm away from the substrate the crystal abruptly switches to the hexagonal-c crystal. This sequence of crystallographic phases is consistent with our previous observations of growth on (001) substrate in the MBE mode. Note that the 3 nm thick amourphous layer that coats the nanowire in figure 4.18c results from the degradation of the nanowire crystal under the TEM beam.

4.11 Conclusion

In this chapter we showed a study of ZnSe nanowires growth on ZnSe surface, with a focus on the (001) surface orientation. In this conclusion we will essentially synthesize our findings.

Two conditions have a significant effect on the nanowire growth rate. The first condition is the growth temperature. We find a 60% increase in the growth rate going from 280°C (ideal for 2D growth) to the optimal nanowire temperature of 410°C. The second condition is the nanowires surface density. The growth rate doubles when we reduce the surface density of nanowires from 170 μm^{-2} to 4 μm^{-2}. We find the relationshiop $\frac{dL}{dt} = a - b\sigma_{NW}$ where $a = 0.34$ nm/s is the maximal growth rate reached when the nanowires are infinitly apart and $b = -0.0011$ nm/s/μm^2 is the change in growth rate for every addition of 1 nanowire per μm^2. This appears to evidence that nanowires compete for adatoms impinging on the 2D layer.

When the nanowires are dense ($\gg$30 μm^{-2}) they grow in random orientations, have many kinks and their crystal structure is often CUB closer to the foot and HEX-c towards the catalyst. When the nanowires are sparse (<30 μm^{-2}) the nanowires grow straight without kinking, and in two specific orientations: 65% in the (111)B direction and 35% in the (001) direction sometimes with a slight tilt, up to 20° toward (111)A. The (111)B oriented nanowires are entirely made of the HEX-c crystal phase, with staking faults. We did not observe the crystal structure of the (001) oriented nanowires. It turns out that when nanowires are grown in the ALE mode, then the nanowires grow along only one type of orientations, in the (114) or (-1-14) direction. Furthermore their crystal structure is entirely CUB (112) or CUB (001) with localized areas of stalking faults.

We use a mass-transport model to fit the nanowire length as a function of growth time. From the fit we extract a Zn diffusion length on the (001) substrate surface of 5.5 nm, close to the 4 nm upper limit of the diffusion length predicted in Ref. [69]. From the fit we also obtain a 31 nm Zn diffusion length on the sidewalls. Since we studied length vs time of only (111)B oriented nanowires with a HEX-c phase, this diffusion length corresponds to (0110) type facets.

A growth study on (111)B substrate yields mostly (>70%) vertically growing nanowires for temperatures between 300°C and 400°. The nanowires also grow straight without kinking even for large nanowire surface densities (at least up to 136 NW/μm^{-2}). In comparison, the nanowires grown on (001) substrate grew straight without kinking only when the surface density was < 30 μm^{-2}.

Chapter 5

Evidence of Growth Mechanism for ZnSe Nanowires

Contents

5.1 Chapter Introduction

In this chapter we discuss evidence hinting at the mechanism by which the nanowires are formed. In chapter 4 we presented the mass-flow model to explain to rate of arrival of the species to the nanowire growth-front, and hence the nanowire growth rate. Here we focus on finding hints to explain how these species tend to nucleate at the growth front. This evidence is strongly based on observations, and it was the subject of a publication [76].

First we tackle the debate regarding the VLS (vapour-liquid-solid) vs VSS (vapour-solid-solid) growth modes of the ZnSe nanowires synthesized with a gold catalyst. Indeed certain reports in the literature assume that the growth occurs with a liquid catalyst [27, 29] while others argue that the catalyst is solid [8, 77] based on comparison of the growth temperature with the referenced liquid eutectic temperatures of Au with Zn and Se. We will show evidence of a solid gold catalyst during the process of NW growth based on RHEED in-situ observations.

Secondly we show evidence of layer by layer growth of the nanowire at the wire-catalyst interface, or ledge flow growth. Standard theories of nanowire growth are based on nucleation at the wire-catalyst interface [78, 79] of island nuclei, or ledges, and experiments suggest that they rapidly spread out laterally over the whole interface [80, 1, 81]. At least two reports show in-situ observations on Si nanowires [82, 83] of those partially nucleated layers as well as their progression as they spread along the interface. We will show HRTEM images taken ex-situ of what we believe are partially nucleated layers on our ZnSe nanowires.

Finally we examine the abuptness at single ZnSe/CdSe/ZnSe heterojunctions created along the nanowire by replacing the Zn flux for a Cd flux for a short period of time during nanowire growth, and we explore the possibility of accumulation of Zn in the gold catalyst through TEM observations of these heterostructures.

5.2 Vapor-Liquid-Solid (VLS) vs Vapor-Solid-Solid (VLS) NW Growth

5.2.1 VLS Growth

The VLS mechanism was first proposed in the 1960s to explain the growth process of gold seeded silicon wires [1]. In the VLS growth mode constituents of the growing material in the vapour phase react with a metallic catalyst alloy, thereby forming a liquid eutectic compound with a melting point that needs to lie below the nanowire growth temperature. The crystalline nanowire constitutes the solid phase.

Nanowire growth is a consequence of the minimization of the chemical potential (μ) as mass is transfered from one phase to another. At thermodynamic equilibrium, the chemical potentials of phases in contact with each other are equal and there is no transfer of mass between these phases (assuming uniform pressure an temperature, typical of nanowire growth conditions). Nanowire growth is a non-equilibrium condition where the differences in chemical potential at phase junctions favor mass transfer.

According to Harmand et al. [84], for nanowire growth to occur the non-equilibrium state must

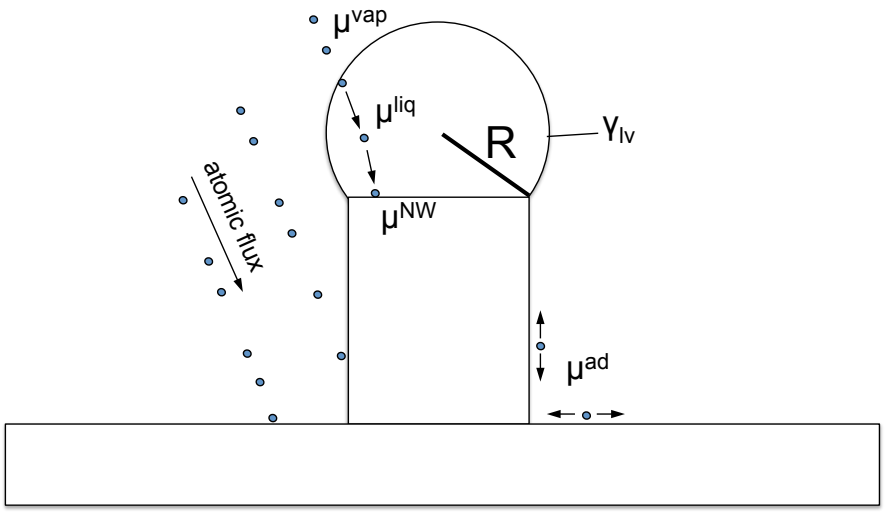

Figure 5.1: Schematic depicting the fundamentals of the vapor-liquid-solid (VLS) mechanism of nanowire growth. The chemical potentials μ of the semiconductor species are different in each phase; γ represents surface tension.

be described by the inequality

$$\mu^{vap} > \mu^{ad} > \mu^{liq} > \mu^{NW} \tag{5.1}$$

where μ^{vap} is the chemical potential of nanowire constituent atoms supplied in the vapor state; μ^{ad} that of adatoms physisorbed onto surfaces (nanowire sidewalls or substrate surface); μ^{liq} that in of the liquid catalyst; and μ^{NW} that in the nanowire crystal.

Upon exposure of the nanowire to the vapor phase, the concentration of constituents in the catalyst will shift from it's thermodynamic equilibrium value, C_{eq}, due to the mass transfer described by the inequality of eq. 5.1. This causes a supersaturated state of the liquid defined by

$$s = C - C_{eq} \tag{5.2}$$

where C is a non-equilibrium local concentration of constituents in the liquid. C is limited by the maximal solubility of constituents in the liquid, which can be obtained from phase diagrams. Because mass flow occurs at phase junctions, a continuous gradient in C (and therefore μ^{liq}) is established in the liquid catalyst. This gradient drives the mass flow from the liquid-vapor surface to the liquid-nanowire interface, following Fick's first law of mass transer $\vec{J} = -D\vec{\nabla}n$, where n is the concentration field and D is the species diffusion coefficient in the liquid phase.

The chemical potential of any given phase is a function of temperature and pressure, i.e. $\mu = \mu(T, P)$. When a phase goes from having a flat outer surface to having a curved surface (of finite radius of curvature R), the surface tension causes a local modification of the pressure inside the liquid catalyst, otherwise known as the Gibbs-Thompson Effect:

$$\Delta P = 2\frac{\gamma_{lv}}{R} \tag{5.3}$$

where γ_{lv} is the surface tension of the liquid at the vapor interface. This causes an increase of the chemical potential by

$$\delta\mu^{liq} = 2\frac{\phi\gamma_{lv}}{R} \tag{5.4}$$

where ϕ is the atomic volume in the liquid. The chemical potential becomes

$$\mu^{liq} = \mu_{\infty}^{liq}(T,P) + 2\frac{\phi\gamma_{lv}}{R} \tag{5.5}$$

where μ_{∞}^{liq} is the chemical potential when the radius of curvature is infinite. The Gibbs Thompson effect becomes increasingly measurable as the system sizes are decreased. For instance this effect was used to explain the decrease in fusion temperature in nanometric size liquid catalysts and, at least in part, can be used to explain why the VLS mechanism can sometimes take place below the catalyst eutectic temperature.

A typical example of VLS growth is given by Si or Ge nanowires, which occurs in the range 300° to 500°C: Au, often the metal of choice for the growth of Si and Ge nanowires, has a melting point at 1064°C in when unalloyed, but it forms a low melting temperature eutectic with Si and Ge with T_{eu} ≈360°C.

When the nanowire being grown is composed of only one species (like Si or Ge) the process of growth can indeed be attributed unambiguously to precipitation of the species at the liquid-solid interface from the supersaturated eutectic compound. It is somewhat less obvious when the nanowire crystal is, say, a binary compound, especially when it is known that one of the species is insoluble in the metal catalyst. This is the case for instance in the synthesis of Au catalysed GaAs nanowires: Ga is known to form a eutectic with Au, AuGa, with 34 at.% Ga at T_{eu} = 339.4°C [74], but the solubility of As in Au is considered to be extremely low [85, 65]. It was suggested that As incorporates the growth front directly from the impinging flux [86]. The growth kinetics based on the VLS mechanism and the related crystal structure have been modelled by Dubrowskii et al. [87] and also by Glas et al. [5] for the case of GaAs NWs.

5.2.2 VSS Growth

VSS stands for the Vapour-Solid-Solid model of nanowire growth. This model assumes that the constituents that make up the nanowire material are dispensed in vapour form and that they are aided by a solid metallic catalyst particle to precipitate in the solid nanowire crystal form. This model contrasts with the more classical VLS mechanism where the catalyst is instead in the liquid form. There are several mentions in the literature of VSS nanowire growth due to diffusion of species through a solid catalyst, including for nanowires of Si [82], Ge [3], GaAs [86] and InP [88].

5.2.3 When Growth can Occur in VLS and VSS Mode with the Same Catalyst

Growth of the same species with the same catalyst can sometimes occur according to both the VLS or the VSS mechanism, depending on growth conditions. A notable experiment showing this phenomenon is presented by Kodambaka et al. [3] who has demonstrated that the the CVD growth

of Ge nanowires can occur with the same Au catalyst either with the catalyst in the liquid state or solid state in the course of the same experiment. In this experiment, key to inducing the catalytic phase transition was the variation of temperature about the AuGe eutectic temperature, but also, interestingly, was the variation of the vapour pressure of the Ge compound, a sufficient reduction of which caused a solidification of the catalyst. Kodambaka's conclusions were drawn from in-situ TEM microscopic observation of the development of facets on the catalyst during growth. So although it can be tempting to attribute the growth mechanism to VLS or VSS based on the comparison of growth temperature to that of the eutectic, Kodambaka's experiment shows that temperature is not necessarily a sufficient criterion. It remains nevertheless a good starting point for analysis.

5.2.4 Phases of Au with Zn and Se

Let's first look at the liquid eutectics in the particular case of ZnSe and Au. According to phase diagrams [65], shown in figure 5.2, the lowest temperature Au-rich eutectic of AuZn occurs at 684°C with 34.5 at.% Zn. In the case of AuSe the lowest temperature eutectic occurs at 760°C with 52 at.% Se. Both these eutectic temperatures are far above our nanowire growth temperature (of around 400°C). At the same time we know that small Au particles tend to exhibit a lowering of their melting temperature due to size effect (Gibbs-Thompson effect). According to Buffat et al. [89] the melting point of Au can be lowered by almost 200°C for small particles of 5 nm in diameter (equal to the radius of semi-spherical Au catalyst seeds in our 10 nm wide ZnSe nanowires). It is unclear how this would translate to gold eutectic compounds with Zn or Se, but in the case where a similar melting point depression would be at work, the modified eutectic temperatures would still remain above the nanowire growth temperature. The magnitude of the melting point depression drops to almost zero as soon as the particle size reaches 10 nm in diameter. These arguments tend to predict a solid state of the Au catalyst during our ZnSe nanowire growth.

From the phase diagrams we also learn that the maximum solid solubility of Zn in FCC Au is ~30 at.% at 403°C, while the solid solubility of Se in FCC Au at that temperature is nearly zero (below detection levels).

The AuZn lattice parameter is graphed as a function of Zn atomic content in figure 5.3 (as per Ref. [64].

5.2.5 RHEED Observation of VSS Growth of ZnSe Nanowires

A characterization technique for real time observation of crystal growth is RHEED, available on MBE systems. This tool is unique to MBE given its requirement of ultra-high vacuum in the growth chamber. RHEED is not used in other chemical deposition systems like CVD or CBE. We use RHEED to monitor nanowire growth and also the phase of the catalyst.

In figure 5.4 we show RHEED diffraction patterns taken at different stages of nanowire synthesis on a (111) oriented substrate. The particular sample corresponding to these RHEED snapshots was grown at 400°C and can be seen in figure 4.17. On (111) substrate the ZnSe nanowires grow mostly normal to the substrate with a crystal which is cubic(111) for the base part of the NW and hexaonal (0001) towards the catalyst.

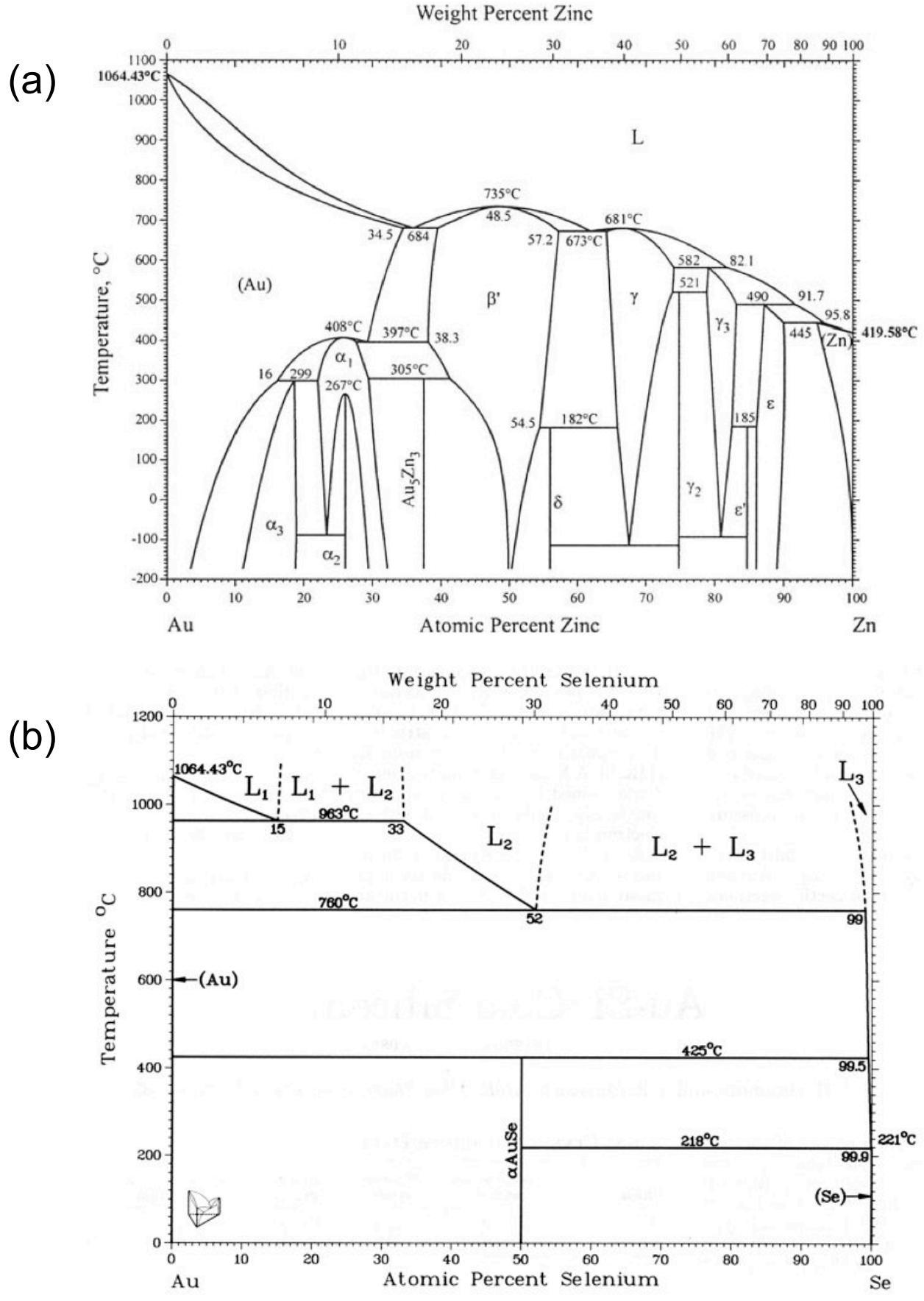

Figure 5.2: Phase diagrams of (a) Au-Zn and (b) Au-Se. Taken from [65].

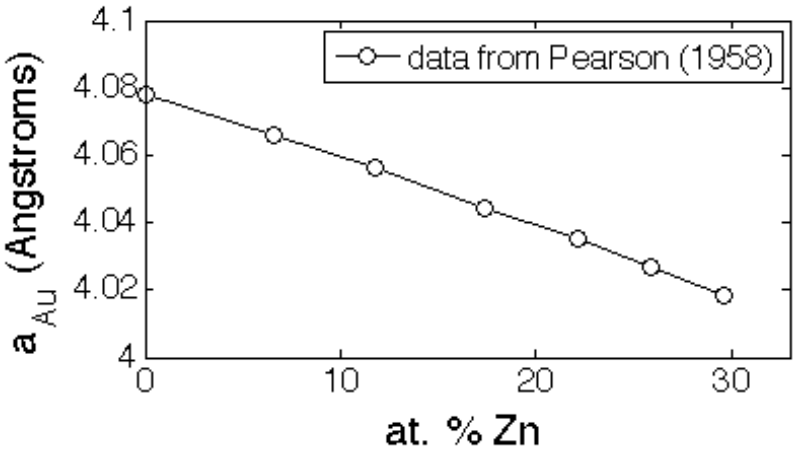

Figure 5.3: Lattice parameter of the FCC AuZn alloy as a function of Zn content. Data reproduced from ref. [64].

We believe that the vertical diffraction streaks seen in figure 5.4 are those of the ZnSe (111) surface probed in the [1-10] azimuth (if we compared them with those presented in Ref. [90]). Upon annealing a gold film on the substrate surface for the generation of Au catalyst nanoparticles, a spotted pattern appears. The spots remain unchanged for the entire process of annealing, from 350°C to 510°C. We attribute the spotted diffraction pattern to Au, since this pattern doesn't show up in the absence of a gold thin film. The presence of the diffraction pattern informs us that the Au nanoparticles are in the solid state, and since the pattern is ordered we know that the Au crystal has a specific orientation with respect to the substrate. Although in the spotted pattern we can recognize an FCC diffraction corresponding to a [110] zone axis and with a c-orientation normal to the substrate, just like it was seen in the RHEED diffraction of Au nanoparticles on (001) substrate in section 3.3, we are less certain of the gold orientation here because some of the spots are unaccounted for and we are also not completely certain of the zone axis in which we are making the observation.

The snapshots figure 5.4b and c show the RHEED diffraction of the sample during nanowire growth at 400°C, while the sample is exposed to Zn and Se fluxes. At 1 minute and at 5 minutes of growth new diffraction spots are seen superimposed onto the ZnSe 2D diffraction streaks. These spots are attributable to the ZnSe nanowire, and their intensity increases with growth time as we would expect from diffraction on crystal volumes of increasing size. Given the good alignment of the nanowire diffraction with that of the 2D layer we know that the nanowires are in perfect epitaxy with the substrate. This alignment is a feature charateristic of growth on (111) substrate and it makes it easy to keep track of the first order Au diffraction because it is clearly separate from the ZnSe features. We note that the Au diffraction spots remain visible at all times, with apparent constant intensity and location. The gold catalyst therefore remains solid under the exposure of the flux beams. It remains this way even at the end of growth, as seen in the figure 5.4d, taken after the beams have been cut off and while the sample temperature is being lowered back down.

Figure 5.4e shows an image intensity profile of the region inside the dotted box on the RHEED of the 5th minute of NW growth. It highlights Au and ZnSe diffraction features. Just like we did in

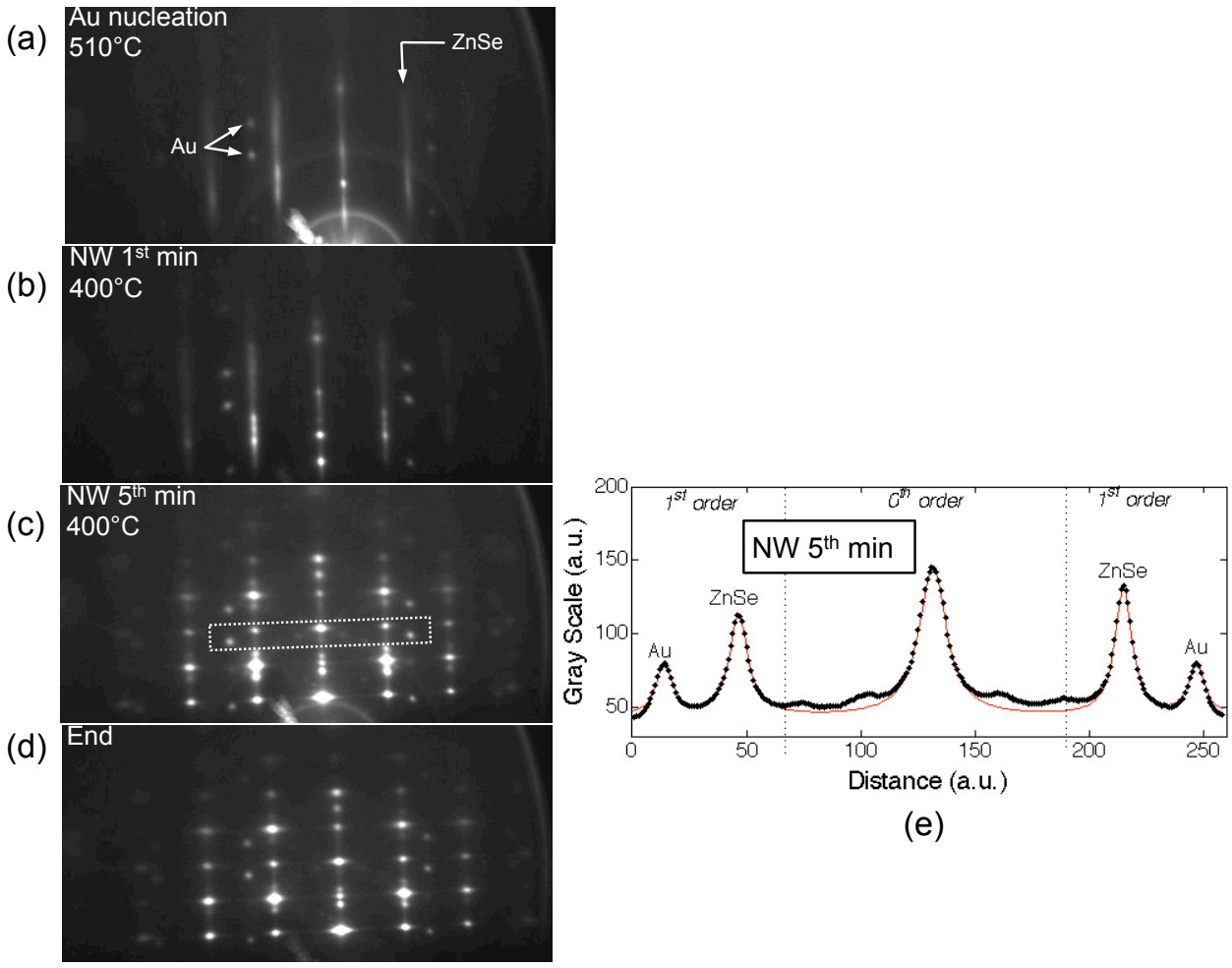

Figure 5.4: RHEED diffraction during ZnSe nanowire growth on (111)B substrate presenting solid Au diffraction spots throughout the growth process. RHEED snap shots show at (a) Au nanoparticle generation, (b) the end of the 1st minute of NW growth, (c) 5th minute of NW growth, (d) end of NW growth when fluxes have been stopped. (e) Image intensity profile from the region in dotted box in (c), and fitted (in red) with five lorentzian curves and a DC intensity shift.

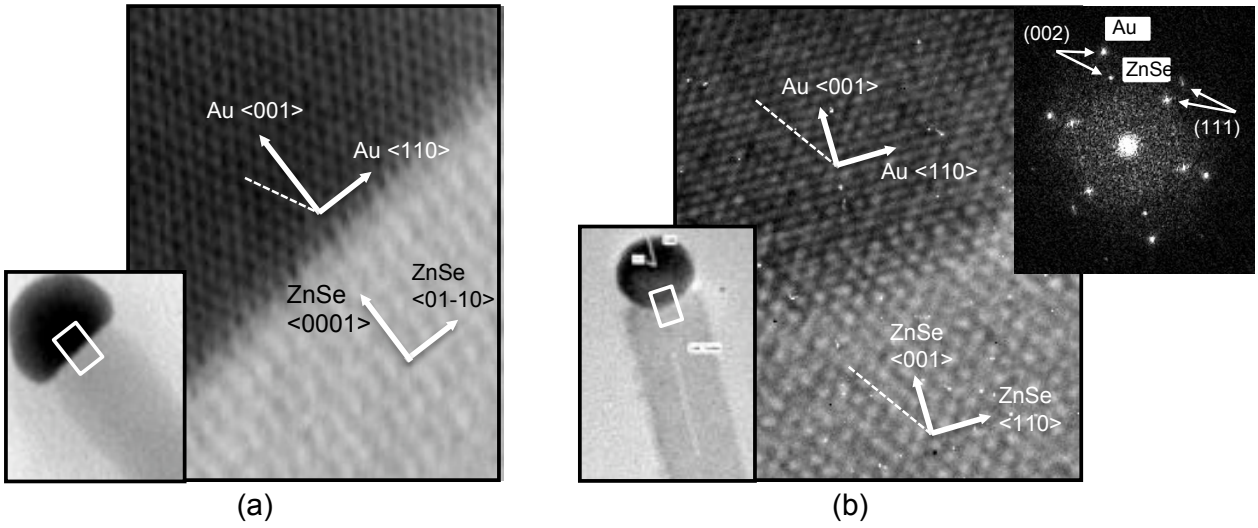

Figure 5.5: Ex-situ observation of orientation and phase of single-crystal Au catalyst by HRTEM. (a) The catalyst is cubic FCC oriented in the (100) direction with respect to the wire axis, and sits on a wurtzite nanowire The ⟨110⟩ planes of the catalyst and the ⟨0110⟩ planes of the wire are similarly oriented. (b) Again the catalyst is FCC in the (100) direction on a ZB (100) nanowire. The GPA power spectrum shown in the top right demonstrates that the Au and ZnSe crystals are identically oriented.

section 3.3 we take the ratio of the separation between the first order diffraction features of ZnSe over that for Au, and multiply by the lattice constant of ZnSe to extract the lattice constant of gold in the plane parallel to the substrate. The intensity profile is fitted with five lorentzian curves (one for the 0th order feature and four for the 1st order features) and with a constant DC shift to account for non-zero background intensity contrast. The ZnSe features in the dotted box are spots originating from NW diffraction. Because the nanowires' phase is mostly wurtzite, we use the ZnSe wurtzite a-parameter, i.e. 3.996 Å [91], which is slightly smaller than that of the zinc blende phase, i.e. 4.007 Å. Also since the RHEED image is recorded at 400°C we take into account the linear thermal expansions of Au (13.99×10^{-6} K^{-1}) and ZnSe (7.5×10^{-6} K^{-1}) to find a room temperature lattice constant for Au. With these considerations we extract an experimental value of a_{Au} = 4.079 ± 0.010 Å. There is a 0.01% difference between our value the value a_{Au} = 4.0786 Å reported for unalloyed gold. Our uncertainty allows for a Zn content in gold between 0 and 6 at.% according to data reported in Ref. [64] and shown in figure 5.3. An analysis conducted on the RHEED image (400°C) of the end of NW growth and using the same diffraction features gives a_{Au} = 4.073 Å, which allows for a slightly larger Zn content between 0 and 9 at.%. These values strongly agree with the lattice constant we found for Au nanoparticles on (001) ZnSe surface in section 3.3, i.e. a_{Au} = 4.074 ± 0.010 Å. We note that for nanoparticles nucleated on the (111) ZnSe surface and shown in figure 5.4a we extract a_{Au} = 4.104 ± 0.15 Å. In the latter case we associate the 2D streaks to the ZnSe zinc blende phase. We do not know if the ZnSe 2D layer remains strained on GaAs at that point. However we know from AFM topography measurements that the 2D ZnSe layer isn't flat, and follows the irregular topography of the GaAs epilayer (consisting of ~ 300 nm terraces–not shown). This could be the

cause of the warps seen on the ZnSe 2D streaks and this could cause our experimental value of a_{Au} to be affected by a systematic error which we do not take into account here. It is also unclear how the surface irregularity affects the rest of experimental values of a_{Au} found on (111) surface.

In figure 5.5 we show HRTEM images of two nanowires with their catalysts, and in these two images the crystal structures of both the nanowire and the catalyst is very well observable. First we notice that in both nanowires the catalyst is cubic and oriented in the [001] direction with respect to the nanowire axis, even if we observe two differently oriented nanowire crystal structures. The wire in figure 5.5a is hexagonal and oriented along the c-axis whereas the wire in figure 5.5b is zinc blende oriented in the (001) direction just like the catalyst. We note that in each case the (110) planes of the Au catalyst are parallel to the (110) planes in the (001) oriented cubic wire, or parallel to the (0110) planes in the hexagonal wire.

5.3 Ex-Situ Observation of Growth Ledges at the Nanowire-Catalyst Interface

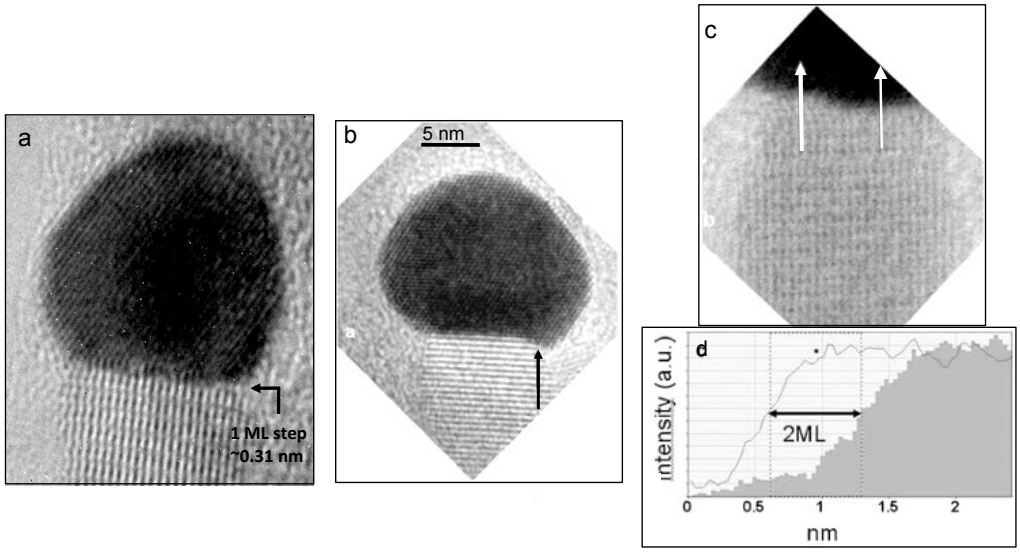

Figure 5.6: HRTEM images of the tip of two nanowires presenting a step at the Au/ZnSe interface. (a) Nanowire ledge near beginning with 1 ML thickness. (b) Nanowire ledge growth near completion. (c) Ledge growth closer to beginning of progression. (d) Intensity profile of the growth interface in (c) showing a 2 ML thickness of the ledge.

When semiconductor atoms reach a critical supersaturation in the metal catalyst (i.e. the nucleation barrier), the semiconductor precipitates at the catalyst-nanowire interface and material is added in a layer-by-layer fashion to the growing crystal [78][83][82]. This growth is sometimes referred to as ledge flow growth or step growth, with a new layer step propagating from one edge to the other at the growth interface. This was demonstrated by in-situ TEM observations on Si nanowires with a Pd_xSi catalyst [83] and also with a Cu_3Si catalyst [92].

According to Wen et al. [82] growth can occur by the same layer-by-layer addition regardless

whether the catalyst is solid (VSS) or liquid (VLS), but these growth modes differ in the kinetic rate of crystallization of the added layers. VLS growth of Si NWs from Au catalyst occurs through abrupt (in the millisecond range) and complete layer formation events separated by long "incubation times" that can last up to 12 seconds. By contrast, VSS growth of Si NWs from Cu_3Si catalyst [92] proceeds by abrupt formation but of only partial layer steps which then propagate slowly (over a few seconds) and with a relatively shorter incubation time. It was suggested that a "reservoir effect" can explain the difference in growth kinetics between the cases with a liquid and solid catalysts. Indeed, a liquid catalyst with a large solubility of the nanowire species that can allow a large supersaturation will cause fast layer growth by immediate emptying of the excess species when critical supersaturation is reached. It turns out in the VLS growth of Si nanowires that at critical supersaturation the excess of Si species in the catalyst is more than the amount needed to nucleate a complete layer, and for that reason no partial layers are ever detected. By contrast solid catalysts usually have a low solubility of the species in the catalyst and may also have lower nucleation barriers: therefore rapid emptying of the reservoir at critical supersaturation results in partial layer formation, and the growth of the rest of the nanowire layer follows the rate of incoming of the species from the supply. For this reason detection of partial layer and their propagation was possible in VSS growth of Si.

In figure 5.3 we show ex-situ TEM observations of what appears to be partially nucleated layers in three separate ZnSe nanowires. In figure 5.3a there is evidence of an incomplete layer of 1 ML in height, whereas figures 5.3b and c show nanowires with uncompleted layers of 2 ML in height. The images show different stages of propagation of the layers along the growth interfaces, and we suppose that the layer propagations were interrupted when the flux beam supplies were interrupted at the end of growth. We have never observed partially nucleated layers of more than 2 ML in height.

It is difficult to determine what is the absolute progress of each of the observed steps in the ZnSe nanowires in figure 5.3 because what we are really observing is the projection of the steps on the image zone axis. It is also difficult to speculate on what could be the minimum partial layer size that nucleates at critical supersaturation, and therefore what is the critical supersaturation with Zn of the solid Au catalyst. The smallest ledge is seen in figure 5.3, representing ~20% of a step with 1 ML thickness. If we assume that the NW has a cylindrical shape and that the catalyst is a hemisphere, both with a 5 nm radius, then the partial layer in figure 5.3 would indicate a critical supersaturation of the Au catalyst at ~1.3 at.% Zn in the catalyst above the equilibrium concentration. This is small compared to the maximal solid solubility of Zn in Au at 400°C and it would be compatible with the possible Zn content we deduced from the RHEED diffraction measurements in the previous section.

Our observations don't rule out the possibility of a negligible nucleation barrier, and therefore the possibility omnipresent ledges. In this scenario neither of the species need to pass through the catalyst, and the species can contribute to the nanowire growth by diffusing inwards from the rim of the nanowire-catalyst interface, like it was proposed in ref. [8].

Partially completed layers were observed on nanowires having a flat interface with the catalyst, just like it was done in Ref. [82] and [83]. In our case this always corresponds to wires which are cubic (111) or hexagonal (0001), and therefore the growth occurs by addition of (111) or (0001) planes. Differently oriented nanowires, like for instance in the cubic (001) direction, have displayed a faceted wire-catalyst interface. We have some evidence that these facets are also oriented in the

(111) directions (see figure 4.16) and step growth could also potentially occur on these planes. We have not sought to find ledges in these cases but we believe that the task would not be trivial given the necessity to properly orient the nanowire under a TEM beam, and also potentially the necessity to differentiate a ledge step structure from the already existing roughness due to facets.

5.4 Study of ZnSe/CdSe/ZnSe Heterostructures for Hints of Growth Mode

5.4.1 Hints of Growth Mode from Heterojunctions in Nanowires

The presence of interface diffuseness at a heterojunction along catalyzed nanowires was suggested to again be due to a "reservoir effect" of constituent atoms present in the catalyst [93]. Given that accumulation in the catalyst of a growth species is necessary to achieve nucleation, it is natural to expect that switching the vapour reactants to a second species will not result immediately in the nucleation at the growth interface of the second species, but rather that a lag time will be recorded during which the catalyst will be depleted of the first species. Also because the two species present simultaneously in the catalyst can have different solubilities, different diffusion rates through the catalyst, and also given that species landing on different areas of the catalyst will reach the growth front at uneven rates [86], it is likely that the desired heterojunctions result in an alloying of both species over a certain height portion of the nanowire. The magnitude of this effect can follow the magnitude of solubility of the species in the catalyst. For instance, a large interface diffuseness was reported by Clark et al. [94], in the VLS growth of Au-catalyzed Si nanowires with SiGe heterostructures. Clark observed that the height of the region with a compositional gradient at the heterojunctions scaled with the nanowire diameters, with a nearly 1:1 ratio for diameters larger than 20 nm. For the particular case of 10 nm diameter wires, the interfacial compositional gradient extended over roughly 5 nm, or 18 ML of Si. Note that the AuSi eutectic used for VLS growth has a Si solubility of nearly 20 at.%. In contrast, SiGe heterostructures in Si nanowires synthesized by VSS growth using an $AlAu_2$ catalyst showed abrupt heterojunction with a compositional gradient extending over 1.3 nm, or less than 3 ML for 17 nm diameter nanowires [93]. In this case the solid $AlAu_2$ catalyst has a nearly negligeable Si solubility.

The outcomes of these experiments appear to illustrate a link between interface diffuseness and the VLS growth mode. It is not always the case though, so we mention here a counter example to this notion, provided by the work of M.T. Bjork et al. [95] in the synthesis of Au-catalyzed InAs nanowires with InP heterostructures. In this experiment, the growth mechanism is attributed to the VLS mechanism, but the heterojunctions are reported to exhibit an interface abruptness on the level of only a few monolayers, in 40 nm diameter wires. So on the basis the examples provided, it actually seems that the magnitude of interface diffuseness in VLS growth is rather likely to be material-specific.

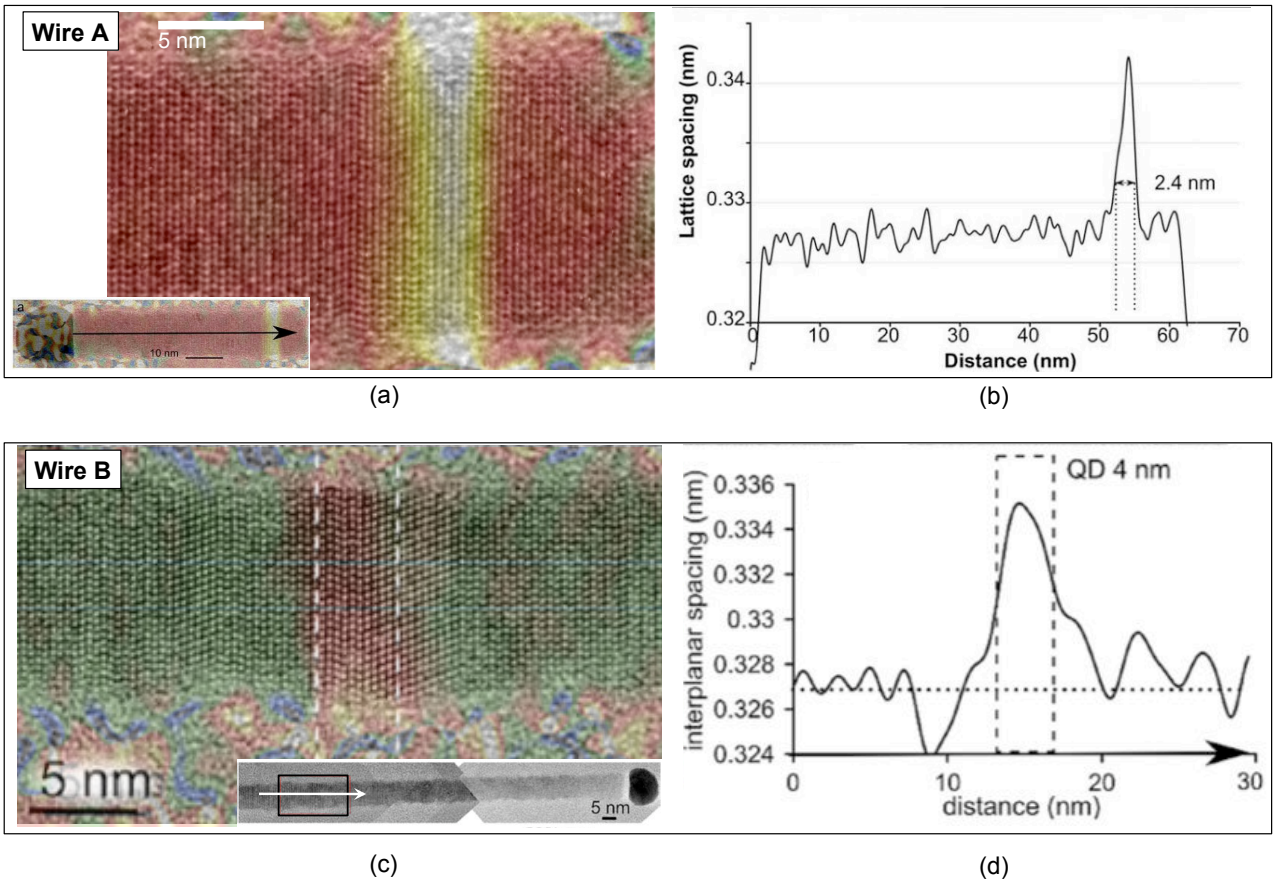

Figure 5.7: Analysis of two ZnSe nanowires with CdSe insertions. In (a) and (c) are HRTEM of wires A and B grown at temperatures of 450°C and 410°C respectively. GPA along the (0002) nanowire axis and in the direction of the arrows, is superposed on the TEM images and also graphed for each wires in (b) and (d).

5.4.2 Observation of ZnSe/CdSe/ZnSe Heterostructures by HRTEM and GPA

Let's now present our observations. We synthesized single ZnSe/CdSe heterostructures in ZnSe nanowires by switching the Zn flux for the Cd flux for 30 s. The growth flux sequence at the heterostructure went as follows: simultaneous interruption of Zn and Se fluxes; 1 minute dead time to allow the Cd cell to outburst; simultaneous introduction of Cd and Se fluxes for 30 s; followed by immediate replacement of the Cd flux with Zn flux to resume ZnSe nanowire growth. The heterostructures were grown after the ZnSe nanowire lengths reached over 100 nm. In figure 5.7 we show two nanowires with heterostructures from two separate samples that were produced in identical conditions except for the growth temperatures: wires A and B were synthesized respectively at 450°C and 410°C. HRTEM images indicate that the crystal structure of both wires is hexagonal (0001) with some cubic (111) portions or stacking faults.

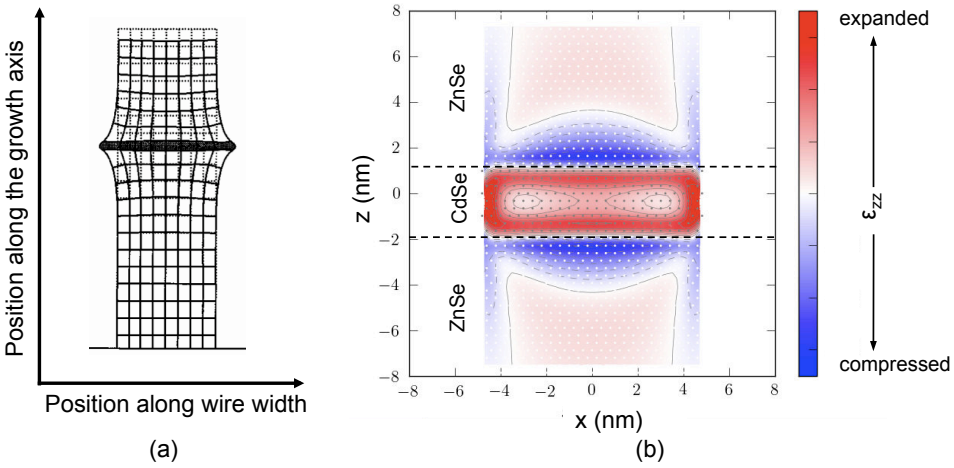

Figure 5.8: (a) Schematic of nanowire lattice planes without (dashed lines) and with (solid lines) heterostructure of larger lattice parameter (modified from Niquet et al. [96]). (b) Axial strain ϵ_{zz} expected in a nanowire at a ZnSe/CdSe/ZnSe heterostructure, allowing for only elastic relaxation of the crystal, including at the sidewalls (image provided by Y. M. Niquet).

We use Geometrical Phase Analysis (GPA) to clearly locate the position of the heterostructures on the HRTEM images. GPA results graphed in figures 5.7b and d show the variation in interplanar spacing in the nanowire axial directions along the midpoint of the wires. From the graphs we obtain maximum lattice parameter variations between the heterostructure and the ZnSe nanowire of 4.8±1.2% for wire A and 4.0±1.2% for wire B. The uncertainties were inferred from the rms variation of the lattice interplanar spacings of the ZnSe nanowires at locations away from the heterostructures. We note that within the uncertainties those variations are less than the percent lattice parameter difference of 6.35% expected between pure and fully relaxed ZnSe and CdSe. In fact, given that the a CdSe layer is expected to be under compressive stress (in the radial direction) in a ZnSe due to the larger lattice constant of CdSe, we would expect the axial parameter variation to exceed 6.35% for synthesis of pure binary compounds (see figure 5.8. Based on this argument we conclude that the CdSe heterostructure segments must rather be $Zn_xCd_{1-x}Se$ alloy. One reason to explain this apparent alloying would be that the Zn content wasn't completely depleted when the CdSe growth

started. Another reason could be a strain driven exchange of Zn and Cd atoms at the heterojuntions. Cd redistribution was observed for CdSe self-assembled QDs grown on ZnSe during the capping with ZnSe by TEM and high resolution x-ray diffraction. The highest Cd concentration in those self-assembled QDs was estimated to be 50% for capping at 240°C [61].

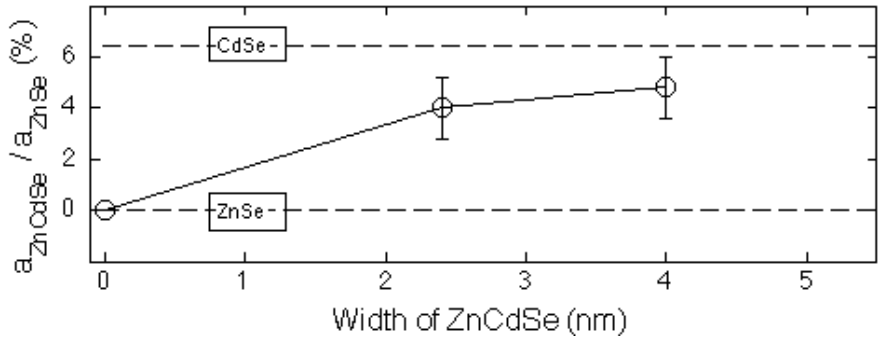

Figure 5.9: Lattice constant variation compared with ZnSe standard recorded at ZnCdSe heterostructure segments shown in figure 5.7. A 0% variation corresponds to pure relaxed ZnSe and a 6.35% variation corresponds to pure relaxed CdSe .

Figure 5.9 shows the maximal lattice constant variation at the heterostructures observed in wires A and B as a function of heterostructure length. The graph tends to indicate that longer $Zn_xCd_{1-x}Se$ segments will have higher Cd contents. It would be interesting to conduct a GPA analysis on heterostructures segments of different lengths to expose the evolution of Cd composition as a function of growth time CdSe growth time.

The analysis of wire A suggests that the heterostructure is confined to a 2.4 nm region, with compositional abruptness of around 1 nm on the leading edge and around 2 nm on the trailing edge. In wire B the heterostructure is confined to a region more or less 6 nm wide with a 4 nm range where most of the change in lattice parameter is concentrated. On wire B we estimate that the heterojunction abruptness on the leading edge is between 2 and 3 nm, and again slightly longer on the trailing edge with a spread over around 4 nm. Cd accumulation could explain why we see a compositional gradient over a longer distance on the trailing edge of both heterostructures. Here, 1ML corresponds to the distance between two (111) planes, or ~ 3.4 Å.

Note that the growth temperature has a direct impact on the ZnSe nanowire growth rates, with a growth rate ratio $\frac{dL}{dt}|_{410°C} : \frac{dL}{dt}|_{450°C} = \frac{0.4 \text{ nm s}^{-1}}{0.25 \text{ nm s}^{-1}} = 1.6$ (see figure 4.11). The ratio of growth rates between the two CdSe segments follows closely what's observed for ZnSe: ($\frac{4 \text{ nm}}{30 \text{ s}}$ (410°C) : $\frac{2.4 \text{ nm}}{30 \text{ s}}$ (450°C) = 1.7). Here, CdSe appears to grow overall 3 times slower than ZnSe.

5.4.3 Observation of ZnSe/CdSe/ZnSe Heterostructure by EFTEM

For a better idea of the distribution of Zn in the ZnCdSe heterostructures we would like to present the analysis we made on a third nanowire from a third sample synthesized in the same conditions as the two previously presented samples, at a growth temperature of 400°C. This heterostructure shown in figure 5.10 causes a slight elbowing of the nanowire and therefore a slight change in growth

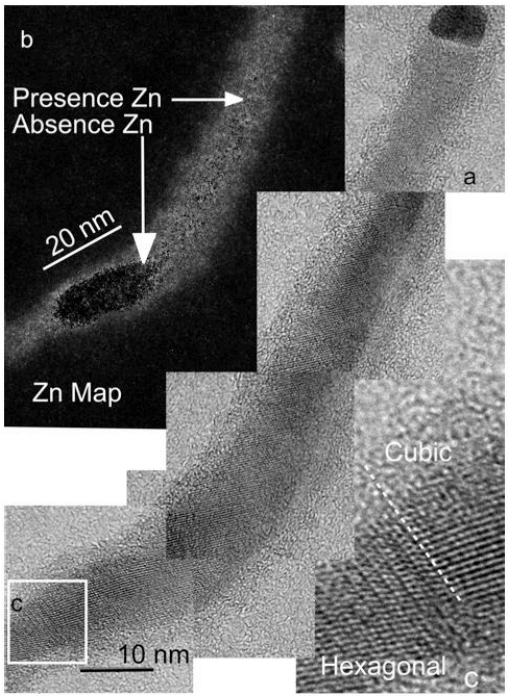

Figure 5.10: ZnSe nanowire with ZnCdSe heterostructure. (a) HRTEM images of a NW with an oval shaped heterostructure. (b) Zn map of the wire in (a) obtained using EFTEM (using the Zn L edge at 1020 eV). (c) Zoom of the region marked in (a). Taken from Ref. [97].

direction. Additionally we observe a temporary increase in the nanowire diameter at and following the elbow. These features were commonly observed in nanowires from large surface density samples, indicating an uneven growth rate and/or anisotropic supply of the growth species. HRTEM maps at the heterostructures could be obtained, but given the presence of important crystal defects GPA was deemed to be a rather less reliable indicator of the heterostructure composition. For the particular case of the wire in figure 5.10 we used EFTEM analysis to produce a map of Zn locations in the nanowire. The heterostructure location is clearly visible as the dark Zn-poor oval-shaped region. The entire outline of the dark Zn-poor region is very sharp, indicative of an abrupt transition between Zn-rich and Zn-poor regions, and hence the heterojunction interface. The EFTEM Zn-map shows only the relative content of Zn with respect to different locations along the nanowire, and therefore we cannot extract from it an absolute concentration of Zn inside the heterostructure. Interestingly the Zn-poor region is surrounded on the sidewalls by a 1-2 nm thick Zn-rich shell, which could be ZnSe, or even ZnO which could have formed after exposure to ambient air. This was not obviou on the previous GPA maps. It is not certain that this shell appears systematically around all heterostructures. If the shell is composed of ZnSe then it could be indicative of a segregation of Zn and Cd species at the growth front, driven by inhomogeneous strain over the growth plane caused by the heterojunction.

5.5 Conclusion

In this chapter we presented the observations and arguments that help us to better understand the process of ZnSe nucleation at the nanowire growth-front:

(i) The diffraction of the crystalline Au-catalyst is observable in-situ on the RHEED during the entire growth process, which demonstrate that Au remains solid during nanowire growth. The observation of solid Au agrees with the fact that the lowest temperature liquid eutectics of AuZn (653°C) and AuSe(760°C) both occur at temperatures above the nanowire growth temperature. From the RHEED snapshots during nanowire growth we extract a room temperature value a_{Au} = 4.079 ± 0.010 Å, in close agreement with the referenced value of unalloyed gold, a_{Au} =4.0786 Å. However within the uncertainty our experimental value allows for a Zn content in the catalyst from 0 to 6 at.%. The AuSe phase diagram indicates a zero solid solubility of Se in FCC gold, so we rule out the possible presence of Se in the catalyst.

(ii) Partially nucleated ledges of 1 and 2 ML in height of ZnSe were observed ex-situ by HRTEM at the nanowire-catalyst interface, demonstrating that nanowire growth can follow a model of partial-step nucleation and step-flow following the rate of arrival of the species to the growth-front. The smallest step we observe by HRTEM indicates an upper limit of 1.3 at.% critical supersaturation of the catalyst above the equilibrium level with Zn. However since we cannot know the minimal step nucleation, we cannot rule out the possibility of a negligible nucleation barrier, and also the possibility that the species could incorporate the growth-front directly from the rim of the catalyst-nanowire interface without having to pass through the catalyst.

(iii) The study of the axial lattice parameter variation along ZnSe/CdSe/ZnSe heterostructures in the nanowires demonstrates that the CdSe segments are alloyed with Zn; this in turn demonstrates that Zn can accumulate at the nanowire and catalyst and incorporate the nanowire structure even after the Zn flux has been interrupted. During the growth process, a prolonged exposure to only the Se flux prior to switching between the type-II species could deplete the excess accumulated type-II species and create compositionally sharper heterojunctions. Further studies would be necessary to verify this hypothesis.

Chapter 6

CdSe QDs in ZnSe Nanowires

Contents

We started talking about our attempts at growing a heterostructure segment of CdSe in the ZnSe nanowires in the previous chapter. We continue on this subject in this chapter with the optical study of these segments, or quantum dots (QDs). Our attempts at creating the heterostructures were not aimed at studying the growth of the heterostructures but rather to produce luminescent QDs. For this reason all the attempted heterostructures were short, of dimension around the 11 nm Bohr diameter in CdSe, in order to seek confinement of carriers. A previous study conducted in our research team by Tribu et al.[26] on such CdSe heterostrucuture QDs in ZnSe nanowires resulted in the observation of QD luminescence and also of single photon emission up to 220K. In this chapter we will show that our new samples also show QD luminescence and single photon emission up to 300K.

Photoluminescence (PL) studies were performed by S. Bounouar, P. Stepanov and C. Morchutt in our team, and these studies have been the subject of four publications [51][98][97][54]. The studies were conducted at temperatures from 5K to 300K with a variable temperature cryostat operated with liquid helium. All the photoluminescence spectra were obtained by pumping the samples with a 405 nm solid state laser unless otherwise indicated. A microscope objective was used to increase the collection efficiency and reduce the probing spot size to around 1 to 2 µm in diameter.

Note that most of the photoluminescence results shown in this chapter were obtained from the sample presented in section 6.3. In section 6.8.4 we will discuss the photoluminescence energy vs QD size for different samples.

To better follow the discussions in this chapter, we start by explaining what kind of luminescence we expect to get from these QDs.

6.1 CdSe Quantum Dot Luminescence

6.1.1 Exciton and Biexciton

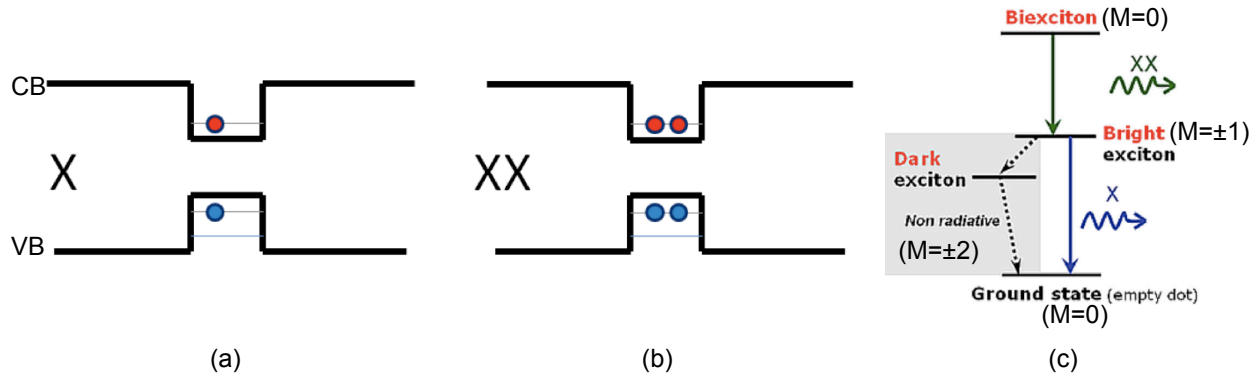

Figure 6.1: Different states of a QD. (a) The exciton, X, level corresponds to one electron and one hole in their lowest excited states. (b) The biexciton, XX, with two excitons filling the lowest excited states. (c) Radiative cascade decay path from XX to the ground state. M is the total angular momentum projection of each state.

A quantum dot consists in a three-dimensional potential box narrow enough to allow a low density

of discrete states through quantum confinement of carriers. These states can be experimentally probed by spectrally analyzing the photons coming from recombinations of excitons. This is what we strived to achieve with the CdSe heterostructures. Since electrons and holes are fermions a maximum of two carriers can be in the lowest excited states at the same time. The exciton, X, which forms when an electron ($J_z = \pm 1/2$) and a hole ($J_z = \pm 3/2$) are located on the first excited states, has a total angular momentum projection of $M = \pm 1$ or ± 2, corresponding respectively to the bright- and dark-excitons. A biexciton, XX, is the presence of two excitons at the lowest excited state with oppositely-spinned carriers, with $M = 0$. Since there is an attractive coulomb interaction between both excitons in the biexiton state, the energy difference between XX and X is lower than the difference between X and the empty state by an amount roughly equal to the exciton interaction energy, E_x. We recall that in bulk CdSe, we have a typical value of $E_x = -20$ meV (defined in chapter 1).

The transition XX leading to the bright-exciton $M = \pm 1$ is always optically allowed. On the other hand the bright-exciton can either recombine radiatively to the ground state, or it can transfer very efficiently (and nonradiatively) to the lower lying dark-exciton state, which typically lies an amount 4-9 meV below the bright-exciton. The optical recombination of the dark-exciton to the ground state is optically forbidden. The X, XX and the XX radiative cascade are depicted schematically in figure 6.1.

Finally, given the very high aspect ratio of the nanowires, the light emitted from QDs in NWs is expected to be highly polarized in the direction of the nanowire [99].

6.1.2 Confinement in a Nanostructure

Three-dimensional confinement of charges in semiconductor quantum dot is especially advantageous in the study of sharp spectroscopic transitions:

(i) the density of states is reduced to a few discrete allowed energy levels inside the quantum dot;

(ii) the wavefunctions of electron and hole carriers are localized at the quantum dot region, which increases the recombination rate;

(iii) there is an increased probability to get a perfect crystal without defects or impurities in a nanometric size quantum dot.

To solve the confinement problem of a quantum dot slice of lower bandgap material in a nanowire of higher bandgap material involves finding carrier wavefunction solutions and therefore energy solutions for the excited states of the electron and hole carriers in the QD slice. Furthermore this needs to be done in a cylindrical geometry, but this problem is not trivial. For a good approximation we can consider the nanowire to be a long thin square beam with a square box slice for the quantum dot. This approach allows us to decouple the x, y and z solutions easily. As the quantum dot sidewalls interface with air or vacuum, we treat the confinement problem in the x and y directions like infinite potential wells. In the z, or axial, direction, we treat the problem like a finite potential well. At the end of these treatments we combine the solutions to find the global energy of the carriers inside the quantum dot.

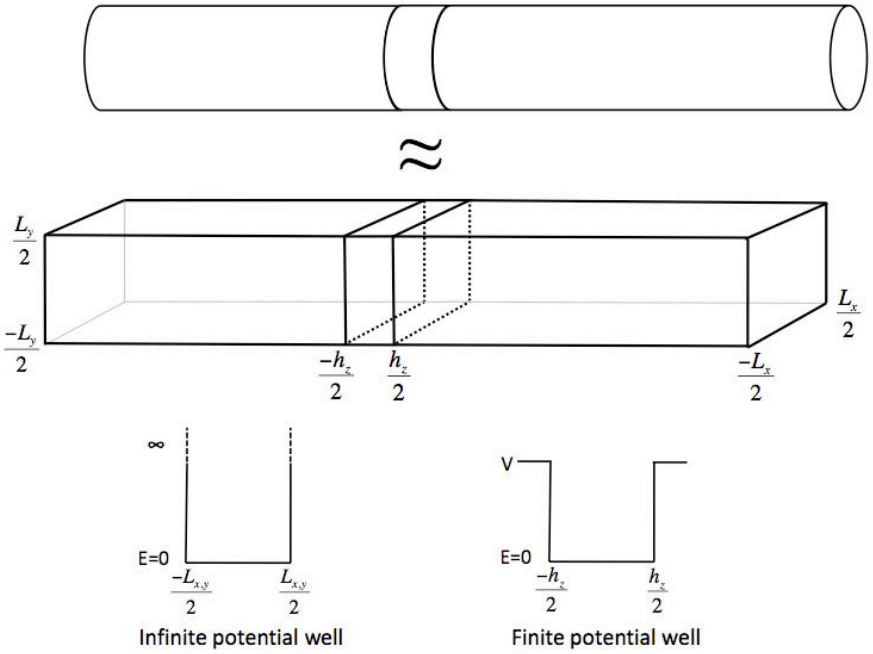

Figure 6.2: The cylindrical QD problem is approximated by a square box in a beam shaped nanowire.

6.1.3 Infinite Quantum Well

Let's start by imagining a region of length L_x. Let the potential energy be equal to zero inside the region and infinite outside. In equation form we have

$$-\frac{\hbar^2}{2m^*}\frac{\partial^2\Psi(x)}{\partial x^2} + V_x\Psi(x) = E\Psi(x) \tag{6.1}$$

$$V_x = 0, |x| < \frac{L_x}{2}, \tag{6.2}$$

$$V_x = \infty, \text{elsewhere.} \tag{6.3}$$

Using the trial solution $\Psi(x) = A\cos(k_x x) + B\sin(k_x x)$ gives the expression for energy:

$$E_x = \frac{\hbar^2 k_x^2}{2m^*}. \tag{6.4}$$

The values for k_x are found by asking that the wavefunction vanish at the box boundaries. Two cases arise:

$$B = 0, \text{symmetric solution, } A\cos\left(k_x|\frac{L_x}{2}|\right) = 0, k_x = \frac{\pi}{L_x}(2n+1) \text{ with } n \geq 0. \tag{6.5}$$

$$A = 0, \text{anti-symmetric solution, } B\sin\left(k_x|\frac{L_x}{2}|\right) = 0, k_x = \frac{2n\pi}{L_x} \text{ with } n > 0; \tag{6.6}$$

The complete set of allowed energies based on the values for k_x are:

$$E_{n_x} = \frac{\hbar^2\pi^2 n_x^2}{2m^* L_x^2}, n_x \geq 1. \tag{6.7}$$

From this expression we can see that the smaller the region size, the higher the confinement energy. We keep the effective mass to acknowledge the dielectric potential inside the confining region.

6.1.4 Finite Potential Well

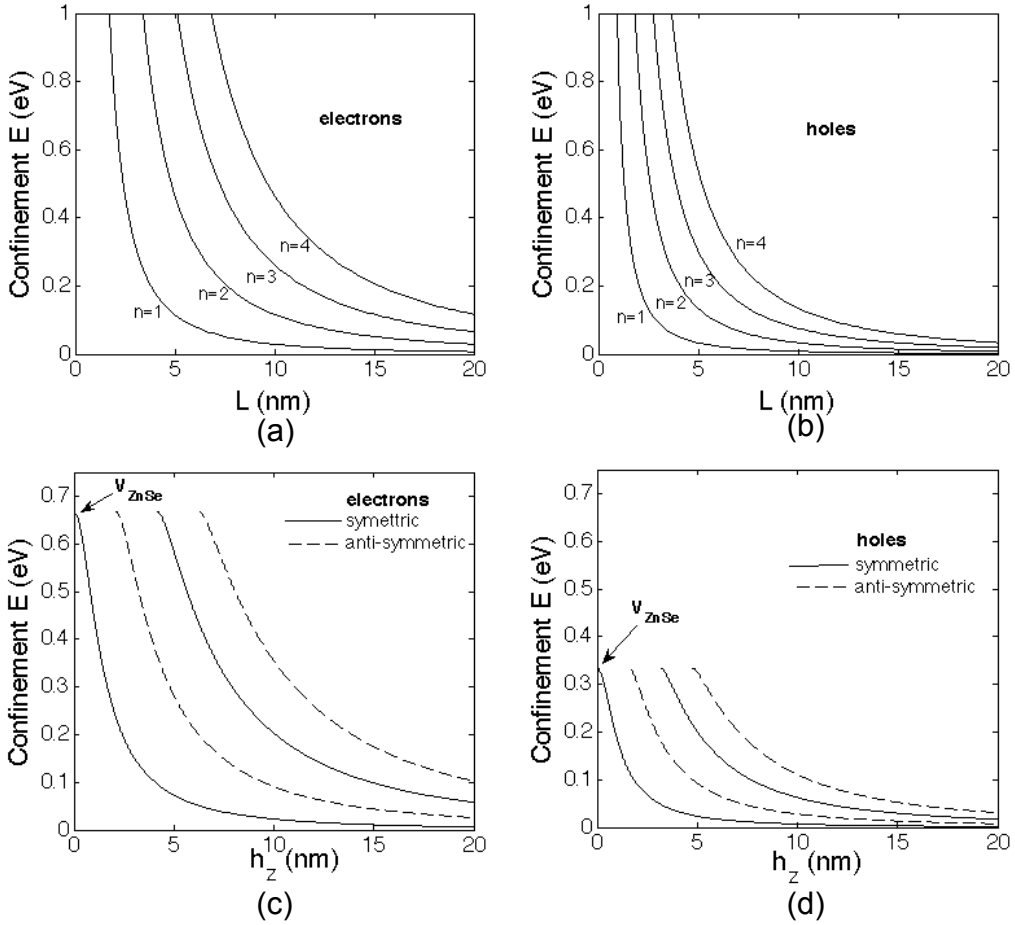

Figure 6.3: One-dimensional confinement energy in a CdSe heterostructure embedded in ZnSe for infinite. (a) and (b) Infinite confinement; (c) and (d) finite confinement. The x-axis variables L and h_z represent the extent of the heterostructure region in one dimension (refer to figure 6.2.

To find the solutions in the z-direction we need to solve Schrodinger's equations by taking into account the constant potential outside the region, i.e. a finite potential problem. The potential is

taken as the difference in conduction (valence) band energies between the nanowire and quantum dot region for the electrons (holes), following the envelope function approximation. The potential barriers amount roughly to $\frac{2}{3}\Delta$ for electrons and $\frac{1}{3}\Delta$ for holes, where $\Delta = E_{gap}^{ZnSe} - E_{gap}^{CdSe}$. We also assume that the effective masses remain unchanged across the regions, which is reasonably true in our case. In this problem the wavefuntion solutions do not need to vanish at the potential barriers: we demand that the wavefunctions be continuous and differentiable at the barriers and that they vanish infinitely far away from the confining region. This means that the wavefunctions extend outside the confining region and into the constant potential region. In figure 6.4 we define regions I, II and III spanned by the wavefunction solutions.

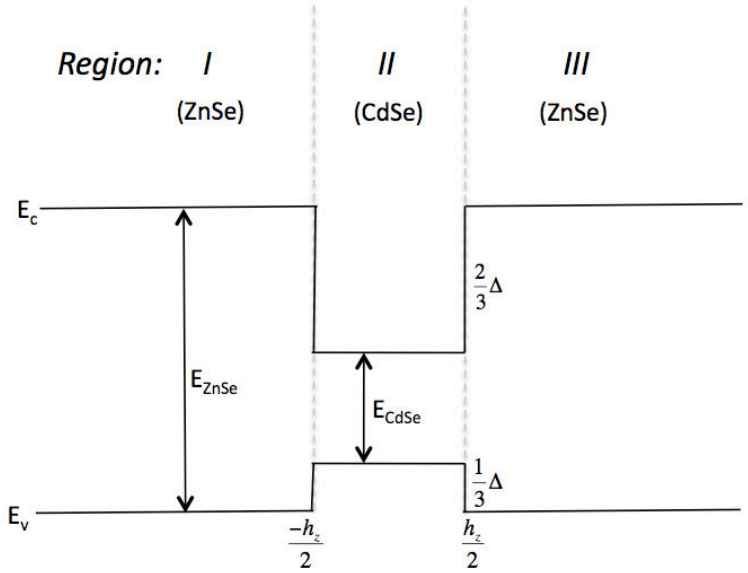

Figure 6.4: One-dimensional band diagram for finite confinement in the CdSe heterostructure region imbedded in ZnSe.

The Schrodinger equation reads

$$-\frac{\hbar^2}{2m^*}\frac{\partial^2}{\partial z^2}\Psi(z) + V\Psi(z) = E_z\Psi(z), V = 0 \text{ for } z < \left|\frac{h_z}{2}\right| \text{ and } V = V_z \text{ elsewhere} \tag{6.8}$$

with

$$\frac{\hbar^2}{2m^*}\frac{\partial^2}{\partial z^2}\Psi(z) = -E_z\Psi(z) \text{ in II} \tag{6.9}$$

$$\frac{\hbar^2}{2m^*}\frac{\partial^2}{\partial z^2}\Psi(z) = (V_z - E_z)\Psi(z) \text{ in I and III.} \tag{6.10}$$

The trial functions again have a periodic form inside the confining region and they are exponentials

outside:

$$\Psi_I = Ae^{\alpha_z z} + Be^{-\alpha_z z}, \qquad \frac{\partial \Psi_I}{\partial z} = \alpha_z Ae^{\alpha_z z} - \alpha_z Be^{-\alpha_z z}, \tag{6.11}$$

$$\Psi_{II} = C\cos(k_z z) + D\sin(k_z z), \qquad \frac{\partial \Psi_{II}}{\partial z} = -k_z C\sin(kz) + kD\cos(k_z z), \tag{6.12}$$

$$\Psi_{III} = Ee^{\alpha_z z} + Fe^{-\alpha_z z}, \qquad \frac{\partial \Psi_{III}}{\partial z} = \alpha_z Ee^{\alpha_z z} - \alpha_z Fe^{-\alpha_z z}. \tag{6.13}$$

To satisfy the condition that Ψ_z approach 0 at $\pm\infty$ we let B=E=0. Plugging the trial functions into the Schrodinger equation 6.9, we obtain that

$$k_z = \sqrt{\frac{2m^* E_z}{\hbar^2}} \qquad \text{and} \qquad \alpha_z = \sqrt{\frac{2m^*(V_z - E_z)}{\hbar^2}}. \tag{6.14}$$

The symmetry of the problem allows us to deal with only one barrier to deduce the energy solutions. Satisfy the continuity conditions by setting $\Psi_I = \Psi_{II}$ and $\frac{\partial \Psi_I}{\partial z} = \frac{\partial \Psi_{II}}{\partial z}$ at $z = -\frac{h_z}{2}$:

$$A\exp(-\frac{\alpha_z h_z}{2}) = C\cos\left(\frac{k_z h_z}{2}\right) - D\sin\left(\frac{k_z h_z}{2}\right), \tag{6.15}$$

$$\alpha A\exp(-\frac{\alpha_z h_z}{2}) = k_z C\sin\left(\frac{k_z h_z}{2}\right) - k_z D\cos\left(\frac{k_z h_z}{2}\right). \tag{6.16}$$

For symmetric solution about z=0 let D=0, and for anti-symmetric solutions let C=0. Taking the ratio of these two equations yields expressions that give the z-confinement energy as a function of h_z, V_z and m^*:

$$\alpha_z = k_z \tan\left(\frac{k_z h_z}{2} + n_z\pi\right) \text{ for } n_z \text{ odd} \tag{6.17}$$

and

$$\alpha_z = -k_z \cot\left(\frac{k_z h_z}{2} + n_z\pi\right) \text{ for } n_z \text{ even} \tag{6.18}$$

and we add $n\pi$ to the arguments to find higher energy solutions.

The plot of the E_z as a function of barrier width h_z in figures 6.2c and d show the first four energy solutions for the case of the electrons and the holes. The confinement energy is lower for the holes, which is consistent with their lower potential barrier. The maximum confinement energy is limited to the barrier height, in contrast with the confinement for the infinite potential (figures 6.2a and b). There always exists at least one confined state, and the number of allowed states increases as the barrier width is increased. Note that in the limit of large h_z the energy solutions become degenerate and comprise subbands quantized by n_x and n_y.

6.2 3D Confinement in the QD-in-NW

If we write the total energy E as the sum of three terms E_x, E_y and E_z and the wavefunction as the product of three separate variable function, such that $\Psi(x,y,z) = \varphi(x)\varphi(y)\varphi(z)$, we can procede to decouple the Schrodinger equation into three one-dimensional equations. We get

$$-\frac{\hbar^2}{2m^*}\nabla^2\varphi(x)\varphi(y)\varphi(z) + (V_x + V_y + V_z)\varphi(x)\Psi(y)\varphi(z) = (E_x + E_y + E_z)\,\varphi(x)\varphi(y)\varphi(z), \quad (6.19)$$

$$-\frac{1}{\Psi(x,y,z)}\frac{\hbar^2}{2m^*}\left(\varphi(y)\varphi(z)\frac{\partial^2}{\partial x^2}\varphi(x) + \varphi(x)\varphi(z)\frac{\partial^2}{\partial y^2}\varphi(y) + \varphi(x)\varphi(y)\frac{\partial^2}{\partial z^2}\varphi(z)\right)+(V_x+V_y+V_z) = E_x+E_y+E_z \quad (6.20)$$

and

$$-\frac{\hbar^2}{2m^*}\frac{\partial^2}{\partial x^2}\varphi(x) + V_x\varphi_(x) = E_x\varphi(x), \qquad \text{and similarly for y and z.} \quad (6.21)$$

The decoupling of the wavefunctions is allowed because the potential V is zero inside the QD, and only the z-component of the wavefuntion subsists outside the QD, according to previous discussions.

We can finally estimate the energy levels of a QD-in-NW in the relevent example of a quantum box region with sides $L_x = L_y = 10$ nm and $h_z = 3$ nm, similar to the CdSe quantum dot size we embed in our nanowires. Taking the exciton states as the true ground states where $n_{electron} = n_{hole} = n$, we have

$$E_n = E_{\text{gap}} + E_n^{\text{electron}} + E_n^{\text{hole}} + Ex, \quad (6.22)$$

where $n = (n_x, n_y, n_z)$, and E_x is the attractive coulomb term with $E_x = -0.02$eV. For the lowest luminescent state $n = (111)$ at a temperature around 4 K we have

$$E_n = 1.85 + (0.029 \times 2 + 0.152) + (0.008 \times 2 + 0.052) - 0.02 \text{ (eV)} \quad (6.23)$$

which yields a total energy of 2.108 eV. For the next degenerate luminescent state n = (121) or (211) we have $E_n = 2.220$ eV.

6.3 Growth of CdSe QDs in ZnSe Nanowires

Here we explain the growth procedure for the QDs that yielded most of the results in this chapter. This growth was performed just like for the low surface density samples presented in Chapter 4, on (001) GaAs with a ZnSe pseudosubstrate and a nanoparticle surface density of 15 μm^{-2}. Growth of the nanowires was performed at a sample temperature of 410°C. For the first 15 minutes the sample was exposed to simultaneous fluxes of Zn and Se (Se:Zn BPR of 4). Then both fluxes were interrupted simultaneously for long enough to allow the Cd effusion cell to outgas. This was followed

by a 30 seconds exposure of the sample to fluxes of Cd and Se (Se:Cd BPR of 3), to produce the CdSe heterostructure. At the end of 30 seconds the Cd flux was stopped and immediately replaced back with the Zn flux for an additional 5 minutes growth of ZnSe wire to cap the heterostructure.

An SEM image of this sample does not reveal hints of the location of the QD in the nanowires, or even that the heterostructures were successfully grown. These nanowires look identical to wires without heterostructures, i.e. with straight stems (without kinks or bulgings) and oriented 65% in (111)B type directions and 35% in a direction close to (001).

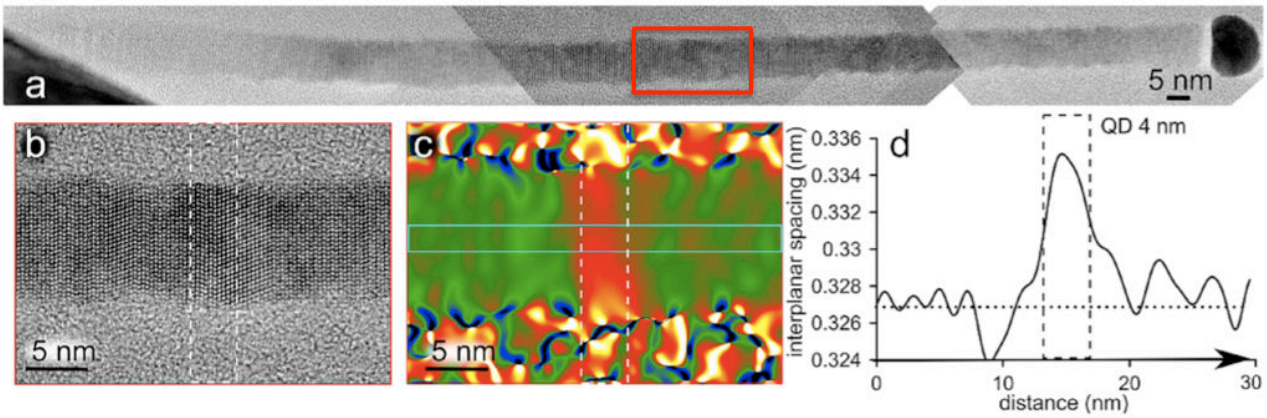

Figure 6.5: Structural analysis by TEM of single ZnSe/CdSe NW-QD. (a) Series of HRTEM images along and entire tilted NW attached to the substrate. The CdSe QD is located in the boxed region about 70 nm from the gold catalyst particle. (b) HRTEM of the boxed region in panel (a): the dashed rectangle in panels (b) to (d) corresponds to the CdSe slice. (c) Geometrical phase analysis of the growth planes along the growth direction. (d) Line profile extracted from the solid boxed region drawn in panel (c). The (0002) interplananar spacing for ZnSe is indicated by the horizontal dashed line. Taken from ref. [51].

The NWs with QDs were studied by HRTEM. Figure 6.5a shows the HRTEM image of a full NW from the ZnSe substrate to the gold particle. Its diameter, constant all along the NW, is of 10 nm. The crystal structure is hexagonal-c with some cubic (111) sections. In order to determine the QD size, geometrical phase analysis (GPA) was used on the HRTEM images to map the interplanar spacing along the wire axis. The GPA analysis of the whole NW reveals no change of lattice spacing all along the wire except in a small region that is attributed to the CdSe insertion (see figure 6.5c). No defects are visible at or near the QD other than stacking faults. On the same sample we have found QD lengths ranging from 2.4 to 4 nm. From figure 6.5d we obtain a lattice parameter variation between the heterostructure and the ZnSe nanowire of 4.0±1.2%. The error is obtained from the uncertainty of the lattice parameter of the ZnSe nanowire at locations away from the heterostructure. The variation even within the error is less than the percent lattice parameter difference of 6.35% expected between pure relaxed ZnSe and CdSe. Since the QD is under compressive stress in the radial direction, a QD of pure CdSe would be expected to produce a parameter variation in the axial direction exceeding 6.35%. Therefore it is likely that the QD is alloyed with Zn.

Since the lateral and longitudinal sizes of the QDs are smaller than the 11 nm Bohr diameter in bulk CdSe we expect full three-dimensional quantum confinement and a strong Coulomb inter-

action between carriers. The next step in the study was to determine if these QDs were capable of luminescence.

6.4 Failure to Determine QD Photoluminescence from Studies on As-Grown Samples due to Emission from Substrate

6.4.1 Control Consisting of an As-Grown Sample with Nanowires Removed

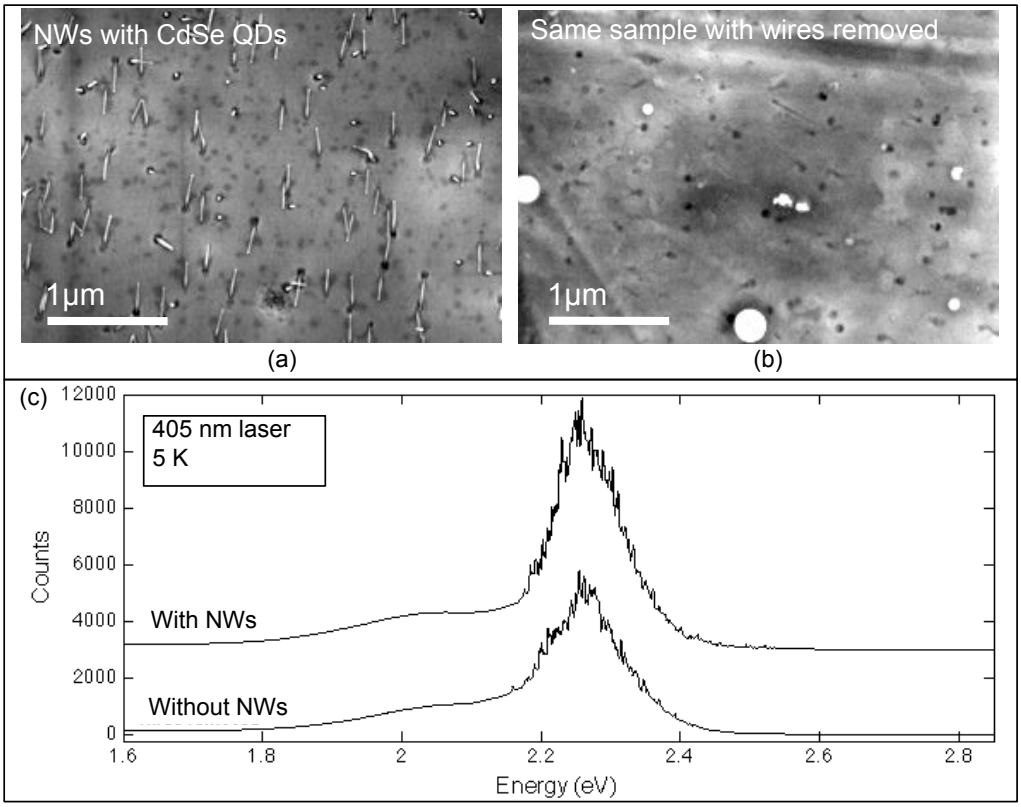

Figure 6.6: Photoluminescence of as-grown sample of NWs with QDs sample demonstrating discrete emission coming from substrate. SEM images of surface before (a) and after (b) NWs were brushed away. Spectra of samples shown in (a) and (b), and measured in in identical conditions of pump power and temperature with a spot size diameter of 1-2 µm.

The first and easiest way to determine if the QD in NWs emit luminescence is to probe the as-grown sample, with the nanowires still attached on the substrate. We conducted this experiment with two pieces of the sample presented in the previous section. The first piece was just the as-grown sample. We delicately removed the wires with a fine brush from the second piece in order to use it as a control to determine the background luminescence due to the substrate. The latter piece was thoroughly investigated by SEM to determine that all nanowires had been removed. Images of both sample pieces are shown in figure 6.6a and b.

It turns out that the spectra from both sample pieces are nearly identical. Both spectra display a similar bell curve topped with discrete emission lines, and the peak of these curves at 2.23 eV is

around where we would expect CdSe QD luminescence to lie if they were doped with Zn (pure CdSe QDs of the size are expected to emit around 2.11 eV). The curve corresponding to the piece without wires reveals that there is confinement of carriers in the sample substrate (at least at the investigation temperature of 5K). Notable differences between the spectra are firstly the number of counts with a minimum of a 30% reduction in counts in the piece without wires (from observation of many data sets), and secondly a different energy range of the discrete emission with a 350 meV span for the sample with wires compared to 250 meV for the samples without wires. Interestingly the sample with wires has a discrete emission extending 100 meV farther into high energies. A polarization study of the spectra did not indicate one prevalent polarization, which could have been expected from QDs in NWs due to the regular orientation of the NWs. It remains therefore impossible from these spectra alone to determine with certainty if the QDs in NWs emit light and where that emission might lie along the spectrum.

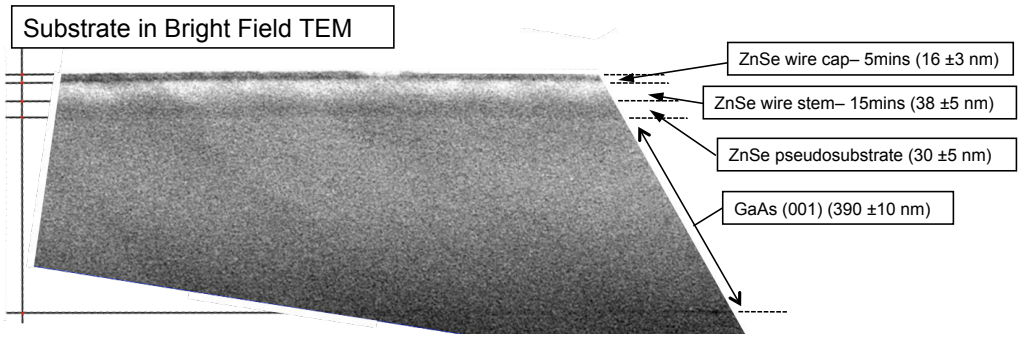

Figure 6.7: Bright field TEM image showing the structure of the NW-QDs substrate. All the layers indicated in this figure were grown by MBE in our laboratory.

A bright field TEM image reveals the composition of the substrate. We clearly note a darker contrast in the top-most layer. We attribute the darker contrast to the presence of Cd, which can more efficiently absorb the electron beam than Zn. The top-most layer, only 16 nm thick, corresponds to the ZnSe growth that occurred at the capping of the QDs. At the bottom of this layer probably lies a layer of CdSe which was deposited at the same time as the QDs were grown. We can almost certainly expect that creation of self-assembled QDs, or at least a roughening of the surface of this CdSe layer could have occured to relax the lattice mismatch. This could very well be the source of the discrete emission we observe from the substrate. There is no report in the literature of CdSe self-assembled QDs growth on ZnSe at a temperature as high as 410°C, but Robin et al. [61] have observed a roughening of a CdSe layer at 280°C after deposition of only 2.5 ML.

The layer thicknesses measured in figure 6.7 correspond closely to what we expect from the known growth rates of ZnSe at different temperatures. The largest relative errors are attributed to the thicknesses of the ZnSe pseudosubstrate and the ZnSe layer deposited during the synthesis of the bottom of nanowires, essentially because it was difficult to pin exactly where the former ended and the latter began. Both of these layers are of different crystalline quality, as is evidence by the difference in their brightness contrast. The ZnSe layer deposited at high temperature during nanowire synthesis is expected to be of lesser quality, and it appears lighter probably because its cross-section

is thinner: this layer was more easily damaged by mechanical polishing and argon milling steps used to produce the thin sample for TEM use. Another contributor to the lighter contrast could be a large presence of vacancies [100].

6.4.2 Control Consisting of Sample Synthesized without Au Catalyst

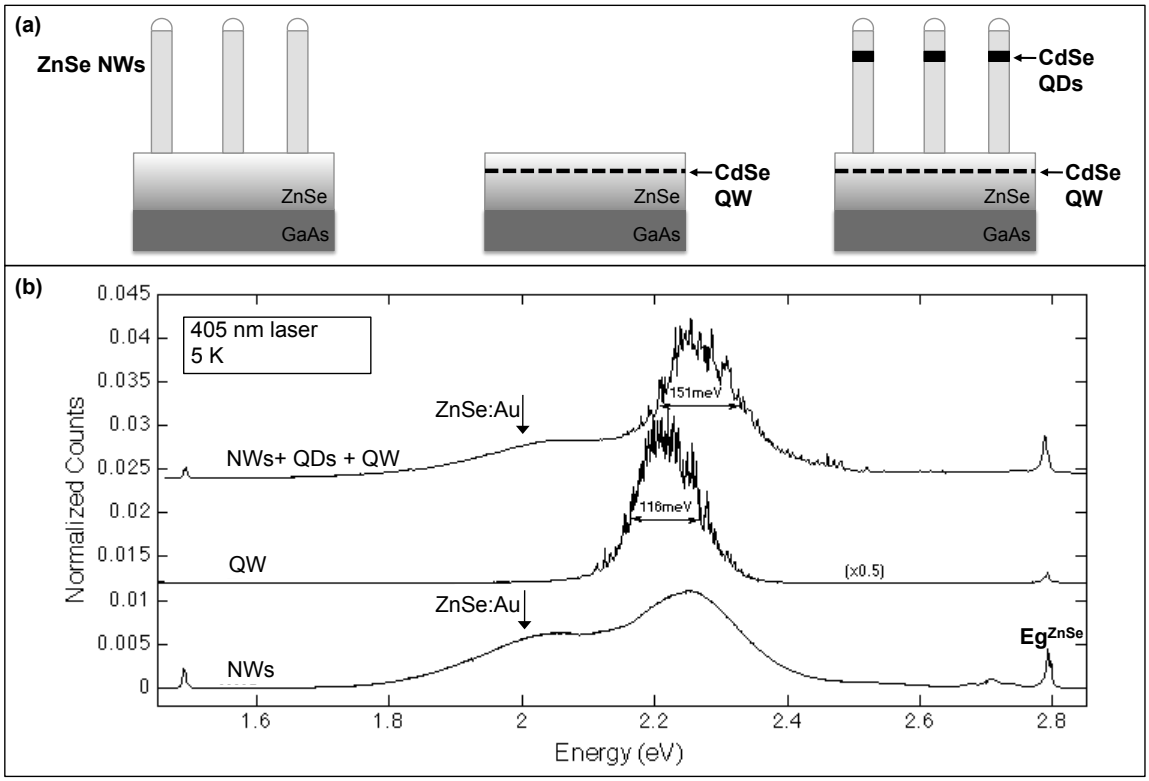

Figure 6.8: Comparison of photoluminescence of NW-QDs sample with two control samples. (a) Schematic of sample structures: NWs sample synthesized without deposition of CdSe; QW sample synthesized without generation of NWs and with deposition of CdSe; NW+QDs+QW with deposition of CdSe and generation of NWs. (b) Spectra for samples in (a). Peaks at 1.5 eV and 2.8 eV corresponds respectively to GaAs and ZnSe bandgaps. Evidence of Au doping is visible in the two samples with nanowires.

We pursued the optical investigation of the luminescence of the CdSe layer imbedded in the substrate by synthesizing a sample in the exact same conditions as the sample of NWs with QDs presented in section 6.3, but without using the gold catalyst. This was meant to produced the exact same substrate layering without the nanowires. We produced this sample to make sure that the emission seen in the previous section from the brushed sample did not in fact come from left over nanowires.

A second control consisted in a nanowire sample grown without CdSe QDs, and produced otherwise in identical conditions to the NWs with QDs sample (but with a nanowire growth limited to 15 minutes, a detail which is not expected to affect luminescence in any significant way). We would like to say immediately that we were not able to obtain photoluminescence from pure ZnSe nanowires.

This result will be shown in the next section. So the optical investigation of the ZnSe nanowire sample provides information solely on 2D ZnSe emission (GaAs only emits at the bandgap, i.e. 1.5 eV). The advantage of also investigating a sample with nanowires is that it can provide information on Au doping.

Figure 6.8b presents the spectra for all three samples. We normalized the spectra for comparison purposes and because they were produced under different pump illumination powers. The spectrum labeled QW (for quantum-well) corresponding to the sample without gold clearly shows that the substrate with the CdSe layer is responsible for discrete emission. The center of its bell curve at around 2.2 eV is red-shifted by around 30 meV with respect to the centre of the NWs with QDs emissions, but this could be attributed to error margins of growth parameters like flux and temperature. Interestingly, just like in the previous section, the discrete emission of the QW sample spans 250 meV.

The spectrum from the nanowire sample without CdSe provides two notable pieces of information. Firstly there exists a large (150 meV wide) red-orange emission located at the same energy as the discrete emission of the other two spectra. More specifically, this emission comes from the lower quality ZnSe layer deposited at high temperature during NW growth (we know this because of comparison with the emission of high quality ZnSe layer - not shown). Secondly the ZnSe shows evidence of emission due to Au doping, at the lower intensity shoulder centered at 2.03 eV. This shoulder shows up on the two samples synthesized with the use of gold, but not on the QW sample which was synthesized without gold. Dean et al. [101] observes a broad bell-shaped red luminescence of ZnSe doped with Au, centered at 2.02-2.05 eV and extending from 1.8 to 2.2 eV which he attributes to donor acceptor pair recombinations. This corresponds precisely to our observations. Based on this information we cannot rule out the possibility of doping of the NWs and QDs in NWs with Au.

6.5 QDs Photoluminescence from NWs Detached from Substrate

In order to verify if the QDs in NWs gave photoluminescence it was necessary to detach them from their original substrate. We transferred nanowires from the sample in section 6.3 onto a patterned silicon substrate by direct contact. This procedure could also produce broken pieces of the sample substrate, and for this reason it was preferable to locate zones of isolated nanowires by the use of SEM. These zones could be located again by using the photoluminescence visualization setup, like shown in figure 6.9a.

The nanowire ensemble with around 30 wires seen in figure 6.9b contained one luminescing QD, with the spectrum shown in figure 6.9c. This QD produced X and XX peaks, separated by 17 meV, as expected for CdSe QDs. Furthermore the X peak shows over 85% linear polarization as seen from the graph in figure 6.9d. On this graph intensity maxima appear every 90° of polarization, but this corresponds to a 180° emission polarization because a $\lambda/2$ plate was used for the measurement.

We would have liked to know the percentage of NWs with QDs that are capable of emission. Unfortunately the QD emission presented in figure 6.9 is the only one we could find during our short optical investigation of the zones images by SEM. Therefore we are only able to provide a crude statistic the yield. Based on three locations with nanowire ensembles investigated on the silicon

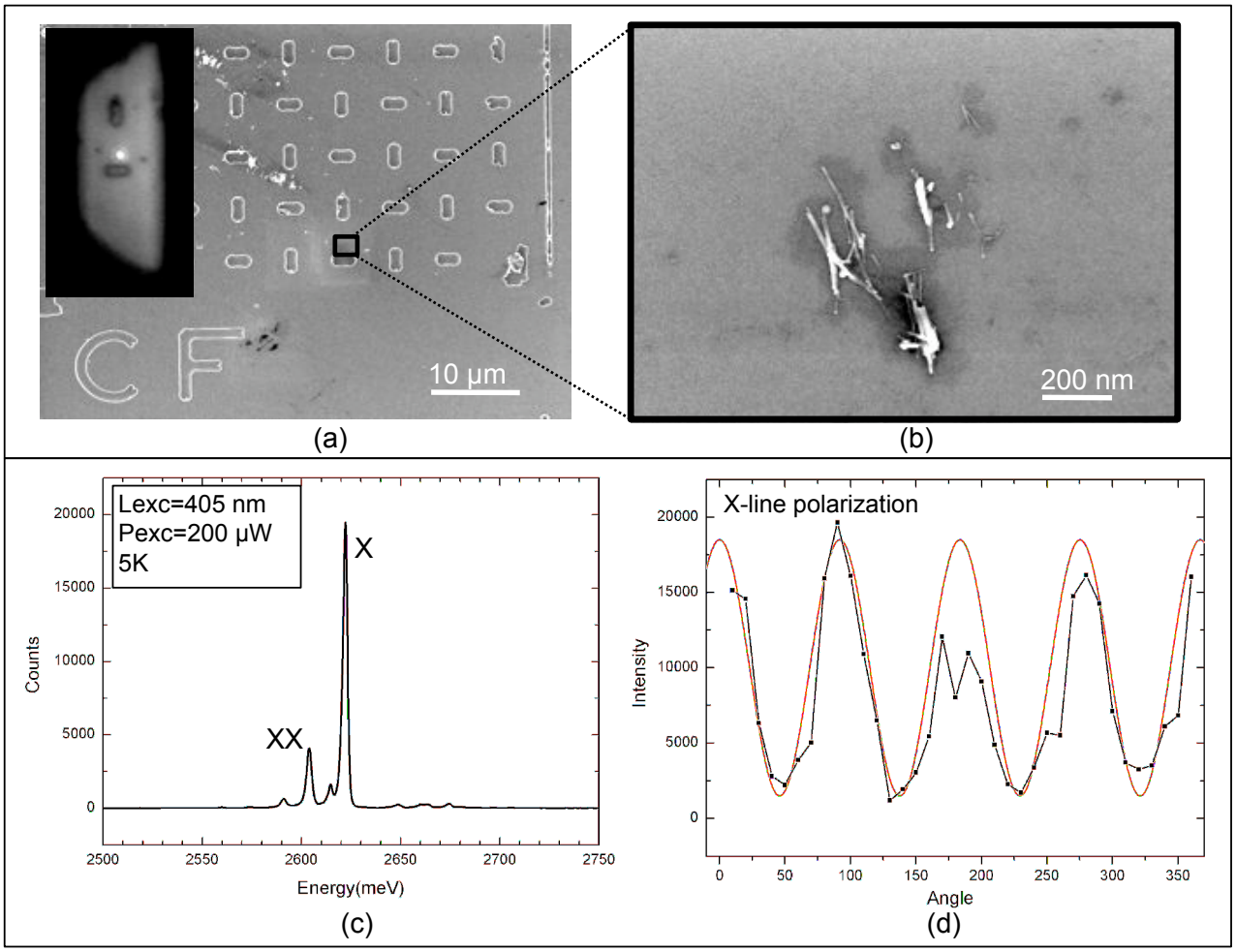

Figure 6.9: SEM image of NWs with QDs detached unto patterned Si substrate and associated photoluminescence. (a) Patterned Si substrate with location of nanowire ensemble - zoom in (b). Inset of (a) shows view from photoluminescence visualization setup. (c) Photoluminescence of ensemble in (b). (d) Emission polarization on X peak of (c), with angle corresponding to $\lambda/2$ plate, showing 180° polarization.

substrate the yield is 1/63. The actual value could be lower. No other luminescence was observed to originate from the ZnSe nanowires.

6.6 Exciton and Biexciton Behaviours

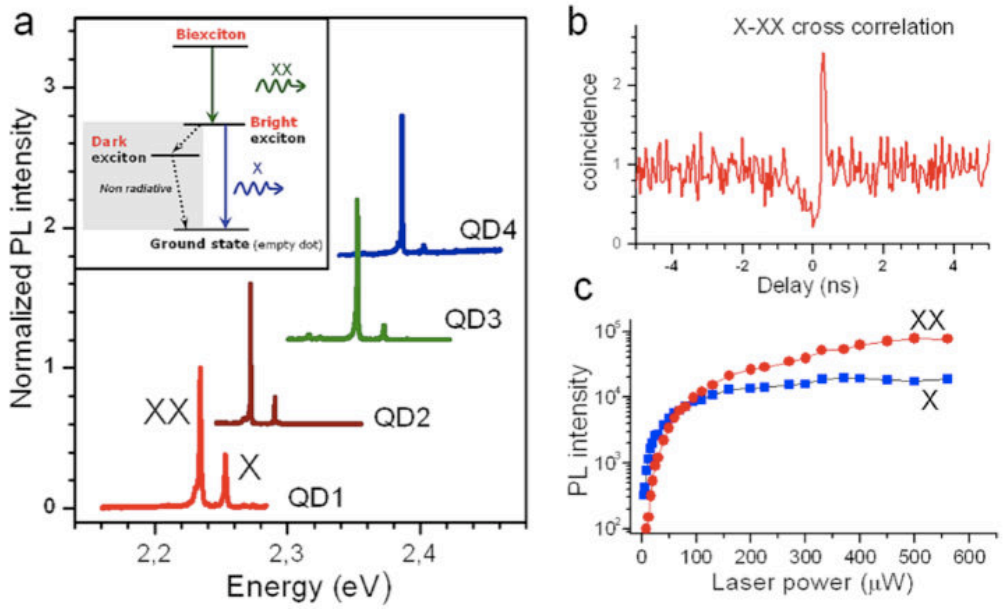

Figure 6.10: Exciton and biexciton in single NW-QDs. (a) Photoluminescence spectra of four selected single ZnSe/CdSe NW-QDs at saturation excitation (see panel c) at 5K. The vertical axes are shifted for clarity. The inset shows the QD energy levels (see section 6.1.1 for description). (b) Exciton-biexciton cross-correlation under continuous-wave excitation for QD1. (c) Exciton and bexciton photoluminescnce intensity as a function of the pulsed laser power. The saturation intensity for XX is higher than for X. Taken from ref. [51].

Many QDs were investigated for their luminescence behavior. We made sure that they were located in NWs by verifying that their emission was linearly polarized. Figure 6.10a presents four selected neutral QDs, each showing two sharp emission lines corresponding to the exciton and biexciton lines, and with a full width at half maximum smaller than 1 meV at 4K, . These transitions are unambiguously identified by recording the cross-correlation histogram (figure 6.10b) whose asymmetric shape is characteristic of the radiative cascade sequence of the biexciton decay to the empty ground state in two steps (XX → X → ground state).

The photoluminescence spectra in figure 6.10a show a striking intensity difference between lines X and XX. The QDs were excited with a 1 ps laser pulses at intensities high enough to fill the QD with at least two excitons, that is, in the biexciton saturation regime. After each laser pulse, one would expect two photons to be emitted: one for the biexciton decay followed by one for the exciton decay. If that were the case then the X and XX lines on the photoluminesence spectra would have equal intensities. In figure 6.10c we show clearly that the biexciton line XX reaches higher saturation intensity than line X. This intensity difference can be explained by the fine structure of the exciton state. Whereas

the biexciton can only decay through one channel– radiative decay to the bright-exciton state – the bright-exciton has two decay channels – radiative decay to the empty state or non-radiative decay to the lower lying dark exciton state. Although increasing the temperature can repopulate the bright-exciton state (endothermic transition from the dark to the bright-exciton), it was observed that line X is significantly weaker than line XX at saturation whatever the temperature [98].

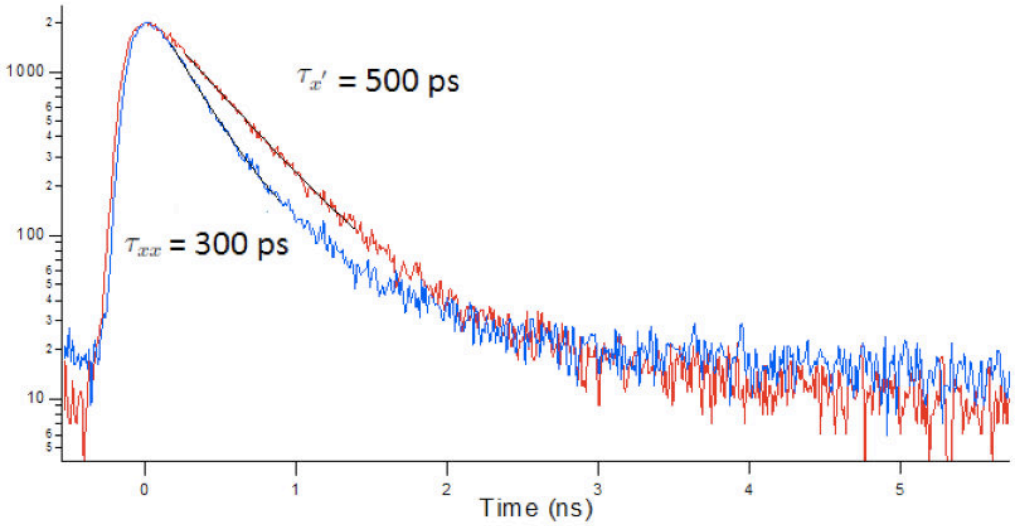

Figure 6.11: Decay of the exciton (blue) and biexciton (red) populations at T=4 K.

Time-resolved photoluminescence shown in figure 6.11 yields lifetimes of 300 ps for the biexciton and 500 ps for the exciton. The measurements were performed at 4K to obtain the radiative lifetimes without having to worry about non-radiative path contributions.

6.7 Single-Photon Generation

We endeavored to determine the suitability of our QDs as single photon generators by studying the autocorrelation of their emission. The study was performed on the XX line since, based on arguments provided in the previous section it is clearly more appropriate as a single-photon source. Figure 6.12b shows the intensity autocorrelation function of the XX line under pulsed excitation for an 80 MHz repetition rate, collected with a numerical aperture 0.4 NA, using a standard HBT [102] optical setup. Photon antibunching can be observed on the XX transition up to 300 K. The raw correlation function at zero is $g^2(0)$ = 0.48 at T = 300 K. The normalized value corrected for the background random coincidences [103] is 0.22. This non-zero value is partly due to contamination from the thermally broadened exciton line.

It should be emphasized that the X and XX lines correspond to single-photons both emitted after each pulse excitation but at slightly different wavelengths. For operation as single-photon source one has to be able to filter out one line from the other because otherwise two photons are detected. The width of the lines must then be smaller than their spectral separation. Increasing the temperature usually leads to an overlap of the two lines due to unavoidable line width broadening [104]. Based

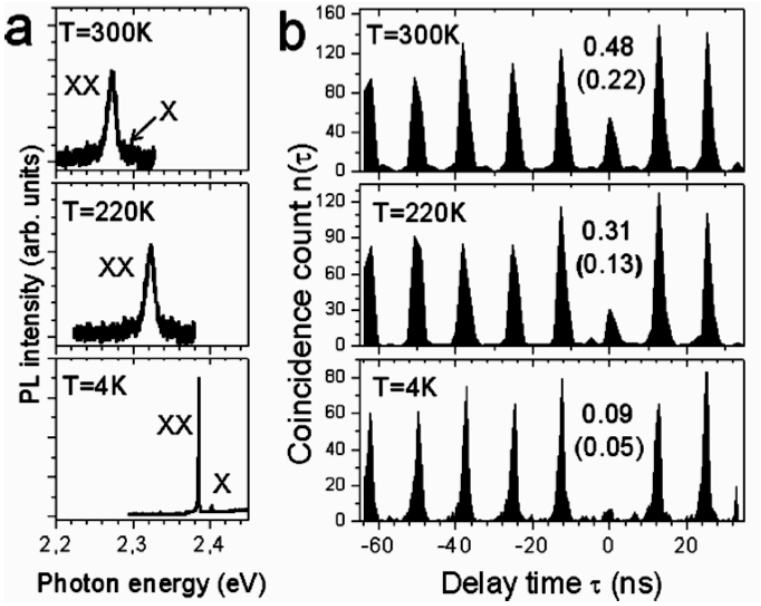

Figure 6.12: Temperature dependent emission properties. (a) Photoluminescence of QD4 at saturation excitation for temperature T=4, 220 and 300 K. The exciton line X is faintly present on the side of the biexciton line XX (the XX-X line separation is 16.4 meV). The biexciton line width increases from 0.9 meV (0.20 nm) at 5 K to 14.3 meV (3.43 nm) at 300 K. (b) Corresponding intensity autocorrelation functions of the biexciton line XX under pulsed excitation. The numbers in the graph are the second-order correlation values $g^{(2)}(0)$ (corresponding to the normalized areas) and the number in brackets are the values corrected for signal to background ratio. The count rate is 10^5 s^{-1} at 4 K and 8×10^3 s^{-1} at 300K with a collection numerical aperture NA = 0.4. The time bin is 0.39 ns for 4 K and 1.6 ns for 220 and 300 K measurements. Taken from ref. [51].

on photoluminescence observations shown in figure 6.12a, in our system the exciton and biexciton lines can still be resolved at room temperature – with a 3.4 nm FWHM line width compared to 3.9 nm X-XX line separation. Additionally, the decay of the bright exciton through the dark-exciton state helps to considerably weaken the exciton line at saturation, further reducing its effect on the degradation of the biexciton antibunchting (as was discussed in section 6.6).

Now for the sake of comparison let's mention other systems which have also provided single photons at room temperature. First we mention the nitrogen-vacancy centres in diamond which are routinely used for room temperature antibunching [105].

An observation of antibunching from solid state quantum dots was provided by Michler et al. [106] as early as 2000, with measurements on core/shell CdSe/ZnS colloidal quantum dots. But the luminescence of these colloidals suffered from severe blinking which degraded their ability to emit single photons on demand. However more recent reports (2008 [107], 2010 [108]) show much improvement on this issue with new colloidal design, while still obtaining excellent photon antibunching at 300 K.

Self-assembled quantum dots for a long time could only provide single-photons up to a temperature of 200K (eg. GaN/AlN [32] at 200K, CdSe/Zn(S,Se) [33]). In a recent report dated 2012, Fedorych et al. [36] finally show room temperature single photon emission from CdSe SK QDs in ZnSSe/MgS barrier.

6.8 Photoluminescence as a Function of QD Size

6.8.1 QD Observed by EDX

Aside from the sample with QD studied so far, other attempts at growing a CdSe segment in the ZnSe nanowires were done, and that's what we'll be exposing in the next few sections before gathering our observations in a graph correlating the QD sizes with their PL emission energies.

We start with the sample seen in figure 6.13 corresponding to a 30 s CdSe QD insertion grown at 400°C. The ZnSe NWs were grown following a two step process: first, a low temperature growth at 300°C was carried out and then a higher temperature was used to growth the part of the NW where the CdSe was inserted.

The SEM image reveals large tapered and randomly oriented base parts of the NWs, as expected for the low temperature part of the NW [25]. On the contrary, the high temperature growth step gives rise to straight NWs of uniform diameter along the wire. Their diameter and length are rather mono-disperse. We observe a diameter of 10 ± 5 nm and a length around 200 nm. The presence of the QD insertion is often marked by the appearance of a thicker part as seen in figure 6.13. The composition of the NW is depicted schematically in figure 6.13c. An EDX line scan was performed along the NW. Because the NWs are thin, the x-ray count is low, giving a low signal to noise ratio. Also, degradation of the NW under the electron beam is observed. The combination of these factors affects the precision of the compositional results (see error bars in figure 6.13d). We did not use standards for EDX analysis, but verified that the Zn and Se composition in the NW were approximately stoichiometric.

A clear Cd rich region is present at the position of the thicker part of the NW. We do not obtain a sharp transition from pure ZnSe to pure CdSe, but rather a gradual alloying on a length of around

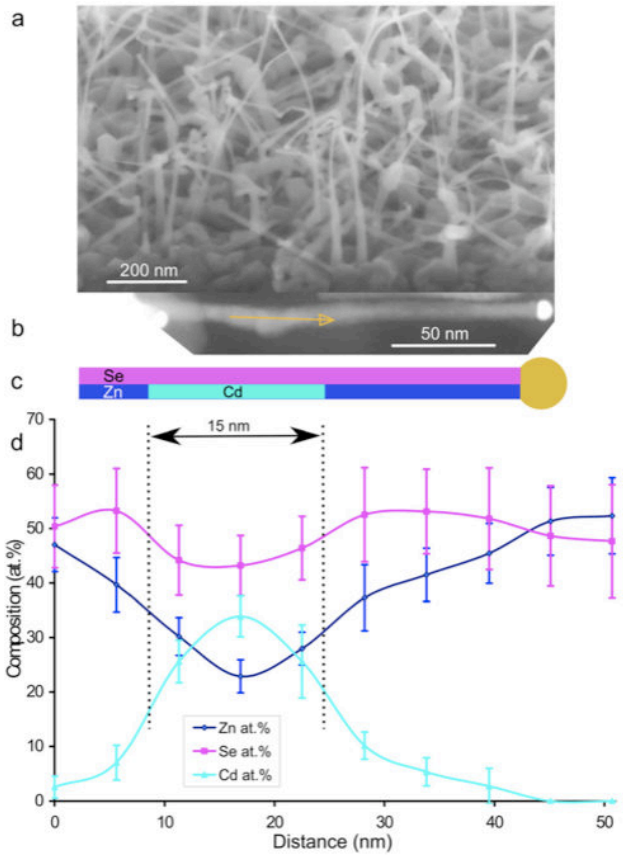

Figure 6.13: Observation of QD by EDX. (a) SEM image of as-grown sample. (b) SEM image of one NW. The arrow indicates the location of the EDX line scan. (c) Schematic of the NW structure and (d) chemical composition profile along the NW, obtained from treatment of EDX spectra. Taken from ref. [97].

5 nm around the QD. That alloying also persists throughout the QD. We then define the length of the insertion as the full width half maximum (FWHM) of the Cd peak, which gives a QD of 15 ± 2 nm long. The decrease of the Se content in the QD region is unexpected. This could be attributed to Se evaporation at the QD region due to the TEM electron beam, Se having the lowest sublimation temperature of all three present elements.

6.8.2 QD Observed by EFTEM

In order to study the crystalline quality of nanowires and to obtain chemical maps rather than chemical profiles along a line like it was done with EDX spectroscopy in the previous section, we performed HRTEM and EFTEM measurements on a different NW from the same sample as in the previous section.

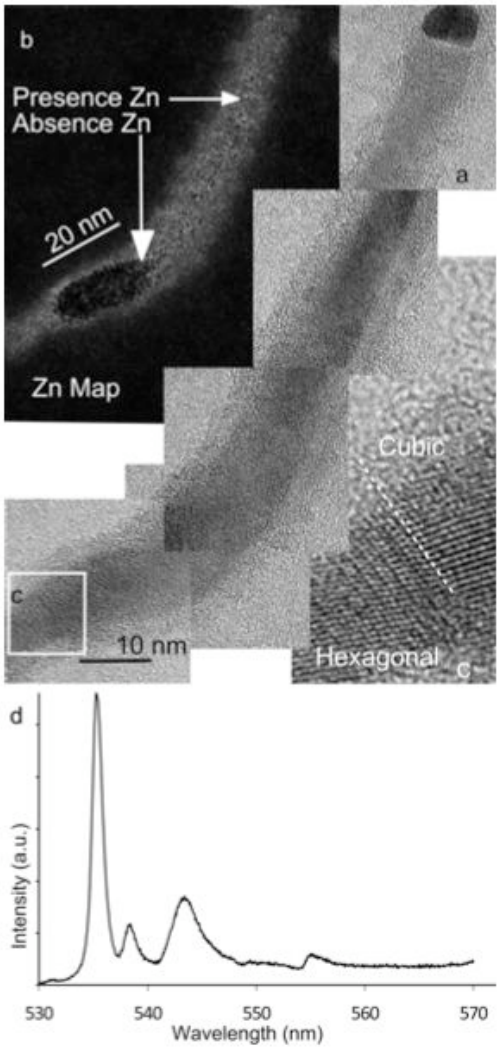

Figure 6.14: Observation of QD by EFTEM. (a) HRTEM images of a NW. (b) Zn map obtained using EFTEM (using the Zn L edge at 1020 eV) on the same NW. (c) Zoom of the region marked in (a). (d) PL spectrum of several NWs from the same sample, at 4K. Taken from ref [97].

A Zn map obtained using EFTEM seen in figure 6.14b displays a strong decrease of the Zn signal at the center of the NW enlargement. In agreement with the previous observation, this droplet shape corresponds to the CdSe QD. The droplet shape of the QD represents an obstacle to line scan measurements of the composition abruptness at the NW interface. It creates a projection of the ZnSe NW region over the CdSe QD region in the images and can explain the apparent Zn-Cd intermixing on the length of 5 nm mentioned earlier on EDX measurements. QD lengths ranging from 12 to 18 nm (±2 nm) were observed on this sample on a total of 4 QDs. A Zn rich shell is present around the QD with a thickness of 1-2 nm. This Zn rich shell is composed of ZnSe (the diameter of the crystalline core is 10 nm, and the diameter of the Zn poor region is only 6-8 nm) and/or possibly an oxide layer.

The HRTEM images in figures 6.14a and b exhibit c good crystalline quality all along the wire. An HRTEM zoom of the enlarged region, which corresponds to the CdSe QD region reveals that the ZnSe NW presents a wurtzite structure along the [0001] direction before the QD, while the QD insertion has the zinc blend structure along the [111] direction. The NW diameter changes from 6 to 10 nm at the QD insertion, and, after the QD insertion, the crystalline structure remains zinc blend. Due to the presence of 4 equivalent [111] directions, the modification in the stacking sequence at the CdSe inclusion level can explain the kinking of some NWs. Interestingly, bulk ZnSe has the zinc blend crystal structure, while bulk CdSe has the wurtzite structure.

The average diameter of the QD is 7 ± 2 nm and smaller than its average full width at half maximum length of 15 ± 3 nm. The presence of the ZnSe shell could improve the optical properties of the QD, as carriers are shielded from local potential of surface defects (including surface oxide states). A PL spectrum obtained from several NWs in figure 6.14d exhibits a sharp peak at 2.32 eV and several smaller peaks. In general, sharp PL peaks with a linewidth around 1.1 nm (5 meV) were observed on this sample in the 2.07–2.34 eV range.

6.8.3 QD Observed by HAADF STEM

Here we present a third NW sample with a QD insertion. The nanowires seen in the SEM image in figure 6.15a were grown at 450°C with a 45 s CdSe QD segment. Most NWs on this sample appear to be vertical. The zinc blende structure and the [001] growth direction of the ZnSe NWs are confirmed by HAADF STEM analysis, as seen in figure 6.15c. The QD insertion with the same crystal structure and orientation is marked by a brighter contrast. The size of the QD, measured from the full width at half maximum of the intensity profile made along the NW (in figure 6.15d), is 3.0 ± 0.5 nm, shorter than in previous samples, although the growth time of the QD insertion is 1.5 times longer. This can be explained by the increase of the growth temperature. No change in the nanowire thickness is observed at the QD location; the diameter is 10 nm. However, in this sample, some Zn-Cd intermixing seems to be present at the interface between NW and QD on a length of 3 nm.

It should be noted that a QD insertion along the [001] direction has the advantage that no change of crystal phase or growth direction is present. A PL spectrum obtained on dispersed NWs is presented in figure 6.15e. Many sharp PL peaks with linewidths between 0.3 and 04 nm (1.5-2 meV) can be observed. The narrow linewidth is an indication of a reduced number of charge traps, which

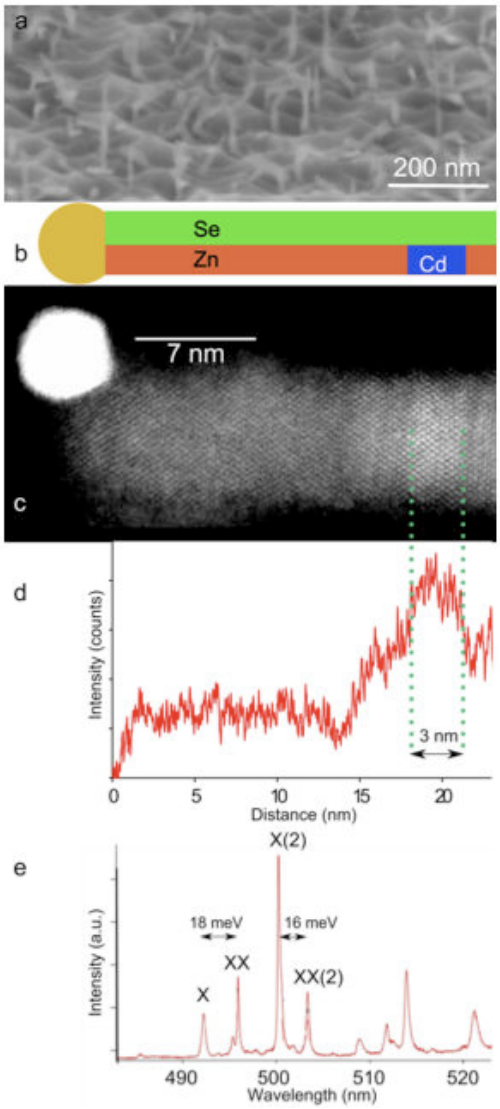

Figure 6.15: Observation of QD by HAADF STEM. (a) SEM image of the as-grown sample. (b) Schematic illustrating the NW composition. (c) HAADF STEM image of one NW from sample seen in (a). (d) Intensity profile made along the NW in (c). (e) PL spectrum obtained on two NWs from the sample, at 4K. Taken from ref. [97].

tend to cause spectral diffusion [109]. The four peaks observed at 493(2.52), 495(2.51), 501(2.48) and 503(2.47) nm(eV) can be attributed to two sets of exciton (X) - biexciton (XX) emissions from QDs in two separate NWs, as confirmed by measuring the PL intensity as a function of excitation laser power (not shown), which are respectively linear and quadratic, and by cross-correlation experiments. PL peaks observed on this NW sample are in the 490–520 nm (2.39–2.53 eV) range.

6.8.4 Photoluminescence as a Function of QD Size

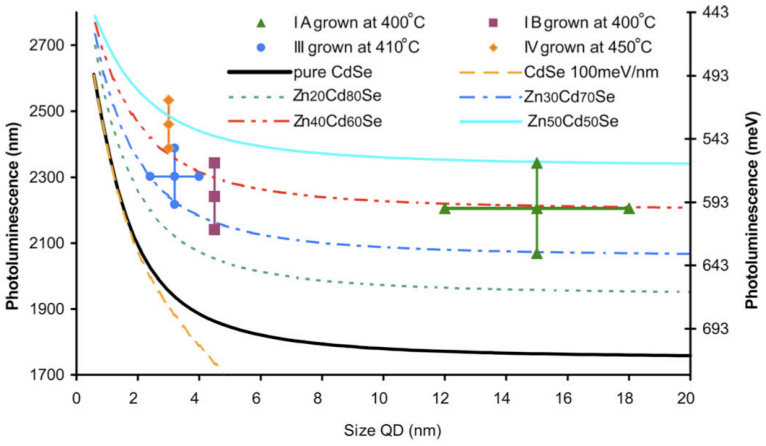

Figure 6.16: Photoluminescence energy vs QD sizes measured by TEM for four different samples. PL performed at 4K with a cw solid state 404 nm pump laser. For comparison a set of calculated curves is provided for different assumptions of Cd-Zn alloying and presence of electric field. Error bar sizes are based on the distribution of values obtained by TEM observations, and energy error bars on PL emission range of given sample. The absence of an error bar indicates the presence of a single data point. Taken from ref. [97].

Figure 6.16 presents the luminescence energy of quantum dots coming from different nanowire samples. There exists a correspondence between these energies and the size of quantum dots determined by TEM techniques. The results of a one-dimensional finite confinement model taking into account a mixed composition of the CdSe quantum dots (as a $Zn_xCd_{1-x}Se$ alloy) and measured quantum dots sizes allow the fitting of the experimental data. For each of the samples in the graph of figure 6.16 only a few QDs could be observed and measured by TEM, demonstrating the difficulty of using this technique on small objects like the nanowires studied here.

The main purpose of this section is to correlate the optical and structural properties of the QDs. Nevertheless, it should be noted, again, that TEM and µPL experiments are not performed on the same unique NWs, but on similar NWs from the same samples. Small wire to wire differences in QD size are therefore possible, as evidenced by the broadening of the PL emission wavelengths for NW ensembles as shown in sections 6.4.1 and 6.4.2.

As expected for semiconductor QDs, the confinement energy increases when decreasing the QD size. Indeed, this tendency is confirmed by the optical spectroscopy results represented graphically in figure 6.16. Two factors can be taken into account to explain the graphical shape:

(i) the confinement associated to the QD size;

(ii) a Cd-Zn alloying, such that the QD material can be described as $Zn_xCd_{1-x}Se$.

The calculated curves shown in figure 6.16 are based on electron and hole confinements in square one dimensional potential wells, or finite quantum wells (QW) of variable widths (associated to the QD length along the NW axis). The barrier bandgap was taken as 2.80 eV (440 nm, corresponding to zinc blende ZnSe at 4K) and the QW bandgap as 1.75 meV (673 nm, corresponding to zinc blende CdSe at 4K [110]). The slightly larger bandgap of wurtzite ZnSe (2.87 eV or 432 nm), was not taken into account in the calculations since it hardly affects the confinement energy. To account for a possible alloying in the QD, calculations were also performed with x values from 0.2 to 0.5. For these calculations the bandgap in the QD material is varied linearly with composition, neglecting a possible slight bowing [111].

The general trend given by the data points tends to rule out the effect of a piezoelectric field. However a strong global shift on the order of 300 meV is observed between data points and calculation for a pure CdSe QD. The comparison between calculation and experimental points provide a clear evidence of a large presence of Zn in the QDs of more than 30% and up to 40%.

The TEM evidence tends to agree with the conclusion of Zn presence in the QD. Indeed, the EDX analysis in section 6.8.1 shows that the Zn concentration decreases but still makes up about 40% of the element II composition. In the EFTEM data of section 6.8.2 it is not possible to rule out the presence of Zn in the QD region because the data is relatively noisy. The HAADF STEM measurements in section 6.8.3 indicate clearly the position along the nanowire where there is a larger concentration of Cd, but they do not inform on the absolute level of Cd and Zn alloying. In fact, a presence of only 2% Cd can already exhibit a contrast large enough to locate the Cd-rich segment, according to the data reported by C. Hsiao et al. [112].

6.9 Conclusion

In summary, let's mention first and foremost that the studies presented in this chapter come from the fact that we were able to successfully grow single Cd-rich segments in ZnSe nanowires for the purpose of creating luminescent QDs. The presence and location of these QDs was confirmed using various TEM techniques (EDX, HRTEM, HAADF-STEM, GPA, EFTEM). For reasons that are still unknown it appears that the growth of these segments produces alloys in the form $Zn_xCd_{1-x}Se$ with x=0.3 to 0.5 rather than pure CdSe.

Photoluminescence studies on the QDs regularly show exciton and biexciton emission lines where the exciton systematically shows lower saturation intensity compared with the biexciton. An explanation for this observation is that the biexciton can only decay radiatively to create the exciton state, whereas the exciton can either decay radiatively to the empty state or non-radiatively through the dark-exciton. Despite a large linewidth broadening from 0.9 to 14.3 meV for temperature increased from 5 to 300 K, the exciton and biexciton remain always resolvable thanks to a large measured exciton binding energy of E_x = 16.3 meV. An auto-correlation function measured on the biexciton under pulsed excitation shows photon anti-bunching up to 300 K with $g^{(2)}(0)$ of 0.22, after correction for random background coincidences.

It should be noted that single nanowires with QDs cannot be investigated optically while they

are still attached on their substrate. That's because a layer of CdSe deposited on the ZnSe base layer at the same time as the CdSe QDs are grown causes a discrete background emission almost identical to the emission of QDs in NWs. This outcome is a general concern for researchers trying to produce luminescent QDs in NWs [49, 47]. The nanowires with QDs in our case imperatively need to be separated from their original substrate by brushing or direct contact onto a non-luminescing substrate. Since in performing this task debris from the original luminescent substrate can be transferred at the same time as the NWs, emission from QDs needs to be tested for linear polarization before it can be attributed as originating from a NW.

The necessity to have to transfer the NWs onto a separate substrate complicates the optical investigations and seriously undermines the original motivation for the work, namely that QDs epitaxially grown in NWs could be produced and easily addressed on the same substrate. So far in this chapter we have presented optical results from growths exclusively on (001) oriented substrates. Growth on (001) substrate results in a non-negligeable deposition of ZnSe 2D layer concomitant with NW growth with a growth rate ratio of 1:5. In Chapter 4 we observed that for growths on (111) substrate above 400°C there was little or no substrate growth. It would therefore be natural to assume that the deposition of a CdSe quantum well on a (111) substrate during growth of QDs in NWs could also be efficiently inhibited.

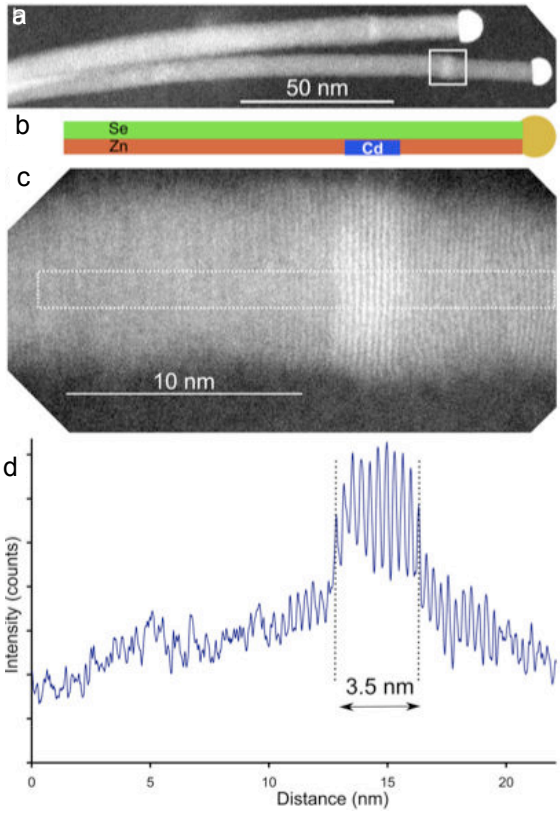

Figure 6.17: TEM observation of QDs in NWs grown on (111) substrate. (a)HAADF STEM image of two NWs side by side; (b) schematic illustrating the NW composition; (d) zoom of the region marked in (a); and (e) intensity profile obtained along the dotted rectangle in (c).

In figure 6.17 we show an HAADF-STEM study of nanowires grown on (111) substrate with a successful insertion of a CdSe segment. Optical investigation have demonstrated that the substrate did not produce any photoluminescence. Unfortunately neither did the the QDs. It is not clear why, since they appear to have the same size and ZB-(111) or WZ-c orientation as most of the QDs observed in luminescent samples. Nevertheless further investigation could yield an explanation and solution to this issue and ultimately allow to circumvent the drawback of having to separate NWs from the substrate. As an added bonus, the NWs on (111) substrate all grow vertically up and QDs can more easily be spotted with TEM by investigating multiple nanowires at similar height from the substrate (like in figure 6.17a).

Conclusion

Growth of Au-catalysed ZnSe NWs has been successfully achieved on ZnSe peudo-substrates grown on GaAs substrate for the first time. ZnSe NWs are in epitaxy with the ZnSe pseudo-substrate and Ga/As diffusion to the NWs is ruled out.

Nucleation of the gold catalyst nanoparticles was studied in details. Formation of nanotrenches in the ZnSe pseudo-substrate can be overcome with the growth of a high quality GaAs epilayer. Au nanoparticles with homogeneous diameters are achieved. When the surface density of nanoparticles is below ~30 μm^{-2} the homogeneity of their diameter is remarkable. The nanowire diameter that results from these nanoparticles is in the range of the Bohr diameter of excitons in ZnSe and CdSe. Moreover the ultralow density achieved for Au nanoparticles makes it possible to grow nanowires in a non-competitive mode, where each growing nanowire benefits from an independent pool of impinging adatoms.

Study of the influence of the growth parameters was done in details. A high Se:Zn~4 flux ratio and a growth temperature in the low 400°C range are found to yield the straightest NWs. Homogeneous NWs with two main orientations are obtained on (001) ZnSe. A third of the NWs are (001) oriented, while two-thirds are (111)B oriented. The nanowire growth rate can be modeled by a kinetic mass-transport model of impinging adatoms flowing to the nanowire growth front. This model has potential in terms of yielding acceptable values for diffusion lengths on the substrate surface and maybe also on the NW sidewalls.

ZnSe NW growth was identified as taking place in the VSS mode, that is, with a solid catalyst, by in-situ RHEED observations. A growth of NWs by ALE, where the fluxes of the binary compound never participate to the growth simultaneously, demonstrates that species can accumulate on the nanowire, probably in the catalyst. Associated variations in catalyst supersaturation could explain why ALE yields only a single NW orientation, in the $\langle 114 \rangle$ direction.

Incorporation of CdSe QDs was studied in details with numerous experimental techniques at different growth temperatures and for different lengths and orientations. It is shown that it is possible in the 410°C range to obtain CdZnSe QDs with a length of a few nanometers with compositionally sharp heterojunctions and a composition in Cd of about 50%. The optical study of such NWs shows sharp excitonic lines with FWHM reaching below 1 meV at 5 K and with over 85% linear polarization. Single photon emission on the biexciton was measured up to room temperature with a raw $g^{(2)}(0) = 0.48$. A limitation comes from the fact that the NWs must be detached from the surface to be studied due to the presence of a discrete background emission originating from the substrate.

In the future, more detailed studies could be conducted in: the ALE NW growth mode to understand the prevalence of certain NW orientations and crystal phases; the growth of CdSe QDs under

different total growth times and flux composition to understand the effect of alloying in the QD; the growth of NWs with luminescent QDs on (111) substrate with the potential suppression of substrate discrete luminescence.

Our demonstration of single photon emission up to room temperature from NW-QDs opens the prospect for a realistic application of QDs as single photon sources thanks to compatibility of epitaxial structures with manufacturing techniques and possibility to be implemented in compact devices. For a practical use as nano-source of light one has to be able to collect efficiently the photons emitted from the QD. In this respect the high aspect ratio of the NW-QD system presents a geometrical advantage: the possibility to form photonic wires for very efficient extraction of photons [113]. Quantum confinement requires growing NWs with very small lateral size (of the order of the Bohr diameter, 11 nm in CdSe). Efficient control of the light outcoupling requires however a photonic wire size of $\sim \lambda/n$ (emission wavelength λ over refractive index n), i.e. typically a few hundreds of nm. Obtaining photonic wires from the thin NW-QD system could be possible by a applying a thick dielectric coating of Al_2O_3 over the NW by atomic layer deposition (ALD).

Finally, study of NW-QDs could be further extended to develop magnetic semiconductor QDs to explore both the intrinsic properties of magnetic polarons and the possibilities and limits of their stabilization in confined geometries. Polarons are the result of a coupling of carriers (electrons, holes, excitons) with localized magnetic ions. Magnetic semiconductor QDs are very promising building blocks for the development of future nanoscale spintronics and spin-photonic devices. An attractive approach to controlling spin effects in these nanostructures is the use of light to generate, manipulate or read out spins. CdSe QDs in ZnSe nanowires could be efficiently doped by Mn substitutional impurities to obtain magnetic QDs, while this is challenging to achieve in (Ga, Mn)As NWs because of the large temperature difference between suitable conditions of GaAs NW growth and efficient Mn doping.

Bibliography

[1] R. S. Wagner and W. C. Ellis. Vapor-Liquid-Solid mechanism of single crystal growth. *Appl. phys. Lett.*, 4(89), 1964.

[2] L. Schubert andP. Werner, N. D. Kakharov, G. Gerth, F. M. Kolb, L. Long, U. Goesele, and T. Y. Tan. *Appl. Phys. Lett.*, 84(4968), 2004.

[3] S. Kodambaka, J. Tersoff, M. C. Reuter, and F. M. Ross. Germanium Nanowire Growth Below the Eutectic Temperature. *Science*, 316:729, May 2007.

[4] O. Landre, R. Songmuang, J. Renard, E. Bellet-Amalric, H. Renvier, and B. Daudin. Plasma-assisted molecular beam epitaxy growth of GaN nanowires using indium-enhenced diffusion. *Appl. Phys. Lett.*, 93(183109), 2008.

[5] F. Glas, J.-C. Harmand, and G. Patriarche. Why Does Wurtzite From in Nanowires of III-V Zinc Blende Semiconductors? *Phys. Rev. Lett.*, 99(146101), OCT 2007.

[6] K. A. Dick, C. Thelander, L. Samuelson, and P. Caroff. Crystal Phase Engineering in Single InAs Nanowires. *Nano Lett.*, 10(9):3494–3499, 2010.

[7] M. S. Gudiksen, J. Wang, and C. M. Lieber. Synthetic Control of the Diameter and Length of Single Crystal Semiconductor Nanowires. *J. Phys. Chem. B*, 105:4062–4064, 2001.

[8] Y. Cai, T. L. Wong, S. K. Chan, I. K. Sou, D. S. Su, and N. Wang. Growth Behavior of Ultrathin ZnSe Nanowires by Au-Catalysed Molecular Beam Epitaxy. *Appl. Phys. Lett.*, 93(233107), 2008.

[9] E. Janik, J. Sadowski, P. Dluzewski, S. Kret, L. T. Baczewski, A. Petroutchik, E. Lusakowska, J. Wrobel, W. Zaleszczyk, G. Karczewski, T. Wojtowicz, and A Resz. *Appl. Phys. Lett.*, 89(133114), 2006.

[10] U. Philipose, T. Xu, S. Yang, P. Sun, and H. E. Ruda. Enhancement of band edge luminescence in ZnSe nanowires. *J. Appl. Phys.*, 100(084316), 2006.

[11] U. Philipose, S. Yang, T. Xu, and H. E. Ruda. Origin of the red luminescence band in photo-luminescence spectra of ZnSe nanowires. *Appl. Phys. Lett.*, 90(063103), 2007.

[12] Q. Li, X. Gong, C. Wang, J. Wang, K. Ip, and S. Hark. Size-Dependent Periodically Twinned ZnSe Nanowires. *Adv. Mater.*, 16(16):1436–1440, 2004.

[13] X. T. Zhang, Z. Liu, K. M. Ip, Y. P. Leung, Q. Li, and S. K. Hark. Luminescence of ZnSe nanowires grown by metalorganic vapor phase deposition under different pressures. *J. Appl. Phys.*, 95(10):5752–5755, 2004.

[14] Y. C. Zhu and Y. Bando. Preparation and photoluminescence of single-crystal zinc selenide nanowires. *Chem. Phys. Lett.*, 377:367–370, 2003.

[15] C. X. Shan, Z. Liu, X. T. Zhang, C. C. Wong, and S. K. Hark. Wurtzite ZnSe nanowires: growth, photoluminescence, and single-wire Raman properties. *Nanotechnology*, 17:5561–5564, 2006.

[16] K. Katayama, H. Yao, F. Nakanishi, H. Doi, A. Saegusa, and T. Shirakawa. *Appl. Phys. Lett.*, 73(102), 1998.

[17] D. B. Eason, Z. Yu, W. C. Hughes, W. H. Roland, C. Boney, J. W. Cook, J. F. Schetzina, G. Cantwell, and W. C. Harsch. *Appl. Phys. Lett.*, 66(115), 1995.

[18] H. Ishikura, T. Abe, N. Kukuda, H. Kasada, and K. Ando. *Appl. Phys. Lett.*, 76(1069), 2000.

[19] T. Shirakawa. *Mater. Sci. Eng. B*, 470:91–92, 2002.

[20] H. Zajicek, P. Juza, E. Abramof, O. Pankrotov, H. Sitter, M. Helm, G. Brunthaler, W. Faschinger, and K. Lischka. Photoluminescence from ultrathin ZnSe/CdSe quantum wells. *Appl. Phys. Lett.*, 62(717), 1993.

[21] I. C. Robin, R. Andre, C. Bougerol, T. Aichele, and S. Tatarenko. Elastic and surface energies: Two key parameters for CdSe quantum dot formation. *Appl. Phys. Lett.*, 88(233103), 2006.

[22] F. Tinjod, I. C. Robin, R. Andre, K. Kheng, and H. Mariette. Key Parameters for the Formation of II-VI Self-Assembled Quantum Dots. *J. Alloys Comp.*, 371:63–66, 2004.

[23] I. C. Robin, R. Andre, and J. M. Gerard. Relation between growth procedure and confinement properties of CdSe/ZnSe quantum dots. *Phys. Rev. B*, 74(155318), 2006.

[24] X. Brokmann, E. Giacobino, M. Dahan, and J. P. Hermier. Highly efficient triggered emission of single photons by colloidals CdSe/ZnS nanocrystals. *Appl. Phys. Lett.*, 85(5), 2004.

[25] T. Aichele, A. Tribu, C. Bougerol, K. Kheng, R. Andre, and S. Tatarenko. Defect-free ZnSe nanowire and nanoneedle nanotructures. *Appl. Phys. Lett.*, 93:143106, 2008.

[26] A. Tribu, G. Sallen, T. Aichele, R. Andre, J.-P. Poizat, C. Bougerol, S. Tatarenko, and K. Kheng. A High-Temperature Single-Photon Source from nanowire Quantum Dots. *Nano Lett.*, 8:4326–4329, 2008.

[27] Y. F. Chan, X. F. Duan, S. K. Chan, I. K. Sou, X. X. Zhang, and N. Wang. ZnSe Nanowires Epitaxially Grown on GaP(111) Substrates by Molecular Beam Epitaxy. *Appl. Phys. Lett.*, 83(13):2665–2667, SEPT 2003.

[28] Y. Cai, S. K. Chan, I. K. Sou, Y. F. Chan, D. S. Su, and N. Wang. *Adv. Mater.*, 18(109), 2006.

[29] Y. Cai, S. K. Chan, I. K. Sou, Y. F. Chan, D. S. Su, and N. Wang. Temperature-Dependent Growth Direction of Ultrathin ZnSe Nanowires. *Small*, (1):111–115, 2007.

[30] A. Colli, S. Hofmann, A. C. Ferrari, C. Ducati, F. Martelli, S. Rubini, S. Cabrini, A Franciosi, and J. Robertson. Low-temperature synthesis of ZnSe nanowires and nanosaws by catalyst-assisted molecular-beam epitaxy. *Appl. Phys. Lett.*, 86(153103), 2005.

[31] Y. Ohno, T. Shirahama, and S. Takeda. Fe-catalytic growth of ZnSe nanowires on a ZnSe(001) surface at low temperatures by molecular-beam epitaxy. *Appl. Phys. Lett.*, 87(043105), 2005.

[32] S. Kako, C. Santori, K. Hoshino, S. Gotzinger, Y. Yamamoto, and Y. Arakawa. A gallium nitride single-photon source operating at 200K. *Nature Mat.*, 5:887–892, NOV 2006.

[33] K. Sebald and P. Michler. Single-photon emission of CdSe quantum dots at temperatures up to 200K. *App. Phys. Lett.*, 81(16):2920–2922, 2002.

[34] B. Legrand, J. P. Nys, B. Grandidier, D. Stievenard, A. Lemaitre, J. M. Gerard, and V. Thierry-Mieg. Quantum box size effect on vertical self-alignment studied using using cross-sectional scanning tunneling microscopy. *Appl. Phys. Lett.*, 74(2608), 1999.

[35] M. Benyoucef, M. Ulrich, P. Michler, and J. Wiersig. Enhanced correlated photon pair emission from a pillar microcavity. *New J. Phys.*, 6, 2004.

[36] O. Fedorych, C. Druse, A. Ruban, D. Hommel, G. Bacher, and T. Kummell. Room temperature single photon emission from an epitaxially grown quantum dot. *Appl. Phys. Lett.*, 100(061114), 2012.

[37] C. Bockler, S. Reitzenstein, C. Kistner, R. Debusmann, A. Loffler, T. Kida, S. Hofling, A. Forchel, L. Grenouillet, J. Claudon, and J. M. Gerard. Electrically driven high-Q quantum dot-micropillar cavities. *Appl. Phys. Lett.*, 92(091107), 2010.

[38] I. C. Robin. *Croissance et controle de l'emission spontanee de boites quantiques semiconductrices CdSe/ZnSe placees en microcavites optiques.* PhD thesis, Universite Joseph Fourier - Grenoble I, 2005.

[39] J. W. Matthews. *J. Vac. Sci. Technol.*, 12(126), 1975.

[40] J. Y. Marzin, J. M. Gerard, A. Izrael, D. Barrier, and G. Bastard. *Phys. Rev. Lett*, 73(716), 1994.

[41] R. Notzel. *Semicond. Sci. Technol.*, 11(1365), 1996.

[42] F. Glas. Critical dimensions for the plastic relaxation of strained axial heterostructures in free-standing nanowires. *Phys. Rev. B*, 74(121302(R)), 2006.

[43] M. Tchernycheva, G. E. Cirlin, G. Patriarche, L. Travers, V. Zwiller, U. Perinetti, and J. C. Harmand. Growth and characterization of InP nanowires with InAsP Insertions. *J. Cryst. Growth*, 7(6):1500–1504, 2007.

[44] P. Wojnar, E. Janik, L. T. Vaczewski, S. Kret, G. Karczewski, To. Wojtowicz, M. Goryca, T. Kazimierczuk, and P. Kossacki. Growth and optical properties of CdTe quantum dots in ZnTe nanowires. *Appl. Phys. Lett.*, 99(113109), 2011.

[45] J. Wang, M. S. Gudksen, X. Duan, Y. Cui, and C. M. Lieber. Highly polarized photoluminescence and photodetection from Single Indium Phosphide nanowires. *Science*, 293:1455–1457, 2001.

[46] I. Friedler, C. Sauvan, J. P. Hugoning, P. Lalanne, J. Claudon, and J. M. Gerard. *Opt. Express*, 17(2095), 2009.

[47] J. Heinrich, A. Huggenberger, T. Heindel, S. Reitzenstein, S. Hofling, L. Worschech, and A. Forchel. Single Photon emission from positioned GaAs/AlGaAs photonic nanowires. *Appl. Phys. Lett.*, 96(211117), 2010.

[48] S. N. Dorenbos, H. Sasakura, M. P. van Kouwen, N Akopian, S. Adachi, N. Namekata, M. Jo, Motohisa, Y. Kobayashi, K. Tomioka dn T. Fukui, S. Inoue, H. Kumano, C. M. Natarajan, R. H. Hadfield, T Zijlstra, T. M. Klapwijk, V. Zwiller, and I. Suemune. Position controlled nanowires for infrared single photon emission. *Appl. Phys. Lett.*, 97(171106), 2012.

[49] N. Panev, A. I. Persson, N. Skold, and L. Samuelson. Sharp exciton emission from single InAs quantum dots in GaAs nanowires. *Appl. Phys. Lett.*, 83(11):2238–2240, SEPT 2003.

[50] M. T. Borgstrom, V. Zwiller, E. Muller, and A. Imamoglu. Optically Bright Quantum Dots in Single Nanowires. *Nano Lett.*, 5(7):1439–1443, 2005.

[51] S. Bounouar, M. Elouneg-Jamroz, M. den Hertog, C. Morchutt, E. Bellet-Amalric, R. Andre, C. Bougerol, Y. Genuist, J.-Ph. Poizat, S. Tatarenko, and K. Kheng. Ultrafast Room Temperature Single-Photon Source from Nanowire Quantum Dots. *Nano Lett.*, 12:2977–2981, 2012.

[52] M. den Hertog, H. Schmid, D. Cooper, J. L. Rouviere, M. T. Bjork, H. Riel, P. Rivallin, S. Karg, and W. Riess. *Nano Lett.*, 9(3837), 2009.

[53] J.-L. Rouviere. The Use of the Geometrical Phase Analysis to Measure Strain in Nearly Periodic Images. *Microscopy of Semiconducting Materials - Springer Proceedings in Physics*, 120:199–202, 2008.

[54] M. den Hertog, M. Elouneg-Jamroz, E. Bellet-Amalric, S. Bounouar, C. Bougerol, R. Andre, Y. Genuist, J.P. Poizat, K. Kheng, and S. Tatarenko. Insertion of CdSe Quantum Dots in ZnSe Nanowires: MBE Growth and Microstructure Analysis. *J. Cryst. Growth*, 323:330–333, 2011.

[55] A. I. Persson, L. E. Froberg, S. Jeppesen, M. T. Bjork, and L. Samuelson. Surface diffusion effects on growth of nanowires by chemical beam epitaxy. *J. Appl. Phys.*, 101(034313), 2007.

[56] M. T. Borgstrom, G. Immink, B. Ketelaars, R. Algra, and E.P.A.M. Bakkers. Synergetic nanowire growth. *Nature Nano.*, 2:541–544, SEPT 2007.

[57] S. K. Chan, S. K. Lok, G. Wang, Y. Cai, Y. J. Wnag, N. Wang, and I. K. Sou. Formation mechanism of nanotrenches induced by mobile catalytic nanoparticles. *App. Phys. Lett.*, 92(183102), 2008.

[58] G. Wang, S. K. Lok, and I. K. Sou. ZnSe nanotrenches: formation mechanism and its role as a 1D template. *Nanoscale Research Lett.*, 6(272), 2011.

[59] J. B. Smathers, E. Kneedler, B. R. Bennett, and B. T. Jonker. Nanometer scale surface clustering on ZnSe epilayers. *App. Phys. Lett.*, 72(10), MAR 1998.

[60] J. Kleiman, R. M. Park, and S. B. Qadri. *J. Appl. Phys.*, 61:2067, 1987.

[61] I. C. Robin, T. Aichele, C. Bougerol, R. Andre, S. Tatarenko, E. Bellet-Amalric, B. Van Daele, and G. Van Tendeloo. CdSe Quantum Dot Formation: Alternative Paths to Relaxation of a Strained CdSe Layer and Influence of the Capping Conditions. *Nanotechnology*, 18(265701), JUNE 2007.

[62] G. Wang, S. K. Lok, S. K. Chang, C. Wang, G. K. L Wong, and I. K Sou. The formation of an aligned 1D nanostructure on annealed Fe/ZnSe bilayers. *Nanotechnology*, 20(215607), 2009.

[63] S. C. Ghosh, P. Kruse, and R. R. LaPierre. The effect of GaAs(001) surface preparation on the growth of nanowires. *Nanotechnology*, 20(115602), 2009.

[64] W. B. Pearson. *A handbook of lattice spacings and structure of metals and alloys.* The Pergamon Press Ltd., Oxford., 1958.

[65] T. B. Massalski. *Binary Alloy Phase Diagrams.* American Society of Metals, Metals Park, Ohio, 1986.

[66] R. Daudin, T. Nogaret, T. U. Schulli, N. Jakse, A. Pasturel, and G. Renaud. Epitaxial orientation changes in a dewetting gold film on Si(111). *Phys. Rev. B*, 86(094103), 2012.

[67] J. Johansson, C. P. T. Svensson, T. Martensson, L. Samuelson, and Werner Seifert. MassTransport Model for Semiconductor Nanowire Growth. *J. Phys. Chem. B*, 109:13567–13571, 2005.

[68] L. E. Jensen, M. T. Bjork, S. Jeppesen, A. I. Persson, B. J. Ohlsson, and L. Samuelson. Role of Surface Diffusion in Chemical Beam Epitaxy of InAs Nanowires. *Nano Lett.*, 4(10):1961–1964, 2004.

[69] J. M. Gains. In-situ characterization of II/VI molecular beam epitaxy growth using using reflection high electron diffraction oscillations. *J. Cryst. Growth*, 137:187–194, 1994.

[70] J. Riley, D. Wolfframm, D. Westwood, and A. Evans. Studies in the growth of ZnSe on GaAs(001). *J. Cryst. Growth*, 160:193–200, 1996.

[71] W. Seifert, M. Borgstrom, K. Deppert, K. A. Dick, J. Johansson, M. W. Larsson, T. Martensson, N. Skold, C. P. T. Svensson, B. A. Wacaser, L. R. Wallenberg, and L. Samuelson. Growth of one-dimensional nanostructures in MOVPE. *J. Cryst. Growth*, 272:211–220, 2004.

[72] N. Wang, Y. Cai, and R. Q. Zhang. Growth of nanowires. *Material Science and Engineering R*, 60:1–51, 2008.

[73] V. Schmidt, S. Senz, and U. Goesele. *Appl. Phys. A*, 80(445), 2005.

[74] M. Tchernycheva, J. C. Harmand, G. Patriarche, L. Travers, and Ge. E. Cirlin. Temperature Conditions for GaAs Nanowire Formation by Au-Assisted Molecular Beam Epitaxy. *Nanotechnology*, 17:4025, 2006.

[75] S. K. Chan, Y. Cai, N. Wang, and I. K. Sou. Control of growth orientation for epitaxially grown ZnSe nanowires. *Appl. Phys. Lett.*, 88(013108), 2006.

[76] E. Bellet-Amalric, M. Elouneg-Jamroz, P. Rueda-Fonseca, S. Bounouar, M. Den Hertog, C. Bougerol, R. Andre, Y. Genuist, J.P. Poizat, K. Kheng, J. Cibert, and S. Tatarenko. Growth of II-VI ZnSe/CdSe Nanowires for Quantum Dot Luminescence. *J. Cryst. Growth*, 2013.

[77] J. Basu, R. Divakar, J. Nowak, S. Hofmann, A. Colli, A. Franciosi, and C. B. Carter. Structure and Growth Mechanism of ZnSe Nanowires. *J. Appl. Phys.*, 104(064302), 2008.

[78] V. G. Dubrovskii and N. V. Sibirev. *Phys. Rev. E*, 70(031604), 2004.

[79] E. I. Givargizov. *J. Cryst. Growth*, 31(20), 1975.

[80] J. Johansson, L. S. Karlsson, C. P. T. Svensson, T. Martensson, B. A. Wacaser, K. Deppert, L. Samuelson, and W. Seifert. *Nature Mat.*, 5(574), 2006.

[81] M. I. McMahon and R. J. Helmes. *Phys. Rev. Lett.*, 95(215505), 2005.

[82] C.-Y. Wen, J. Tersoff, M. C. Reuter, E. A. Stach, and F. M. Ross. Step-Flow Kinetics in Nanowire Growth. *Phys. Rev. Lett.*, 105(10):195502, Nov 2010.

[83] S. Hofmann, R. Sharma, C. T. Wirth, F. Cervantes-Sodi, C. Ducati, T. Dasama, R. E. Dunin-Borkowski, J. Drucker, P. Dennett, and J. Robertson. Ledge-Flow-Controlled Catalyst Interface Dynamics During Si Nanowire Growth. *Nature Mat.*, 7(10):372, MAY 2008.

[84] J. C. Harmand, M. Tcherniycheva, G. Patriarche, L. Travers, F. Glas, and G. Cirlin. GaAs nanowires formed by Au-assisted molecular beam epitaxy: Effect of growth temperature. *J. Cryst. Growth*, 301–302:853–856, 2007.

[85] J. C. Harmand, G. Patriarche, N. Pere-Leperne, M-N. Merat-Combes, L. Travers, and F. Glas. Analysis of vapor-liquid-solid mechanism in Au-assisted GaAs nanowire growth. *App. Phys. Lett*, 87(203101):3, 2005.

[86] A. I. Persson, M. W. Larsson, S. Stenstrom, B. J. Ohlsson, L. Samuelson, and L. R. Wallenberg. Solid-Phase Diffusion Mechanism for GaAs Nanowire Growth. *Nature Mat.*, 3:677–681, OCT 2004.

[87] Dubrowskii. *Phys. Rev. B*, 78(235301), 2008.

[88] K. A. Dick, K. Deppert, L. S. Karlsson, L. R. Wallenberg, L. Samuelson, and W. Seifert. *Adv. Funct. Mater.*, 16(1603), 2005.

[89] P. Buffat and J-P. Borel. Size effect on the melting temperature of gold particles. *Phys. Rev. A*, 13(6):2287, JUNE 1976.

[90] F. S. Gard, J. D. Riley, R. Leckey, and B. F Usher. Reflection High-Energy Electron Diffraction (RHEED) Study of MBE Growth of ZnSe on GaAs(111)B Surfaces. *App. Surf. Sci.*, 181:94–102, JUNE 2001.

[91] I. V. Korneeva. . *Sov. Kristallogr.*, 6:55, 1962.

[92] C.-Y. Wen, M. C. Reuter, J. Tersoff, E. A. Stach, and F. M. Ross. Structure, Growth Kinetics, and Ledge Flow During Vapor-Solid-Solid Growth of Copper-Catalyzed Silicon Nanowires. *Nano Lett.*, 10:514, 2010.

[93] C.-Y. Wen, M. C. Reuter, J. Bruley, J. Tersoff, S. Kodambaka, E. A. Stach, and F. M. Ross. Formation of Compositionally Abrupt Axial Heterojunctions in Silicon-Germanium Nanowires. *Science*, 326:1247, Nov 2009.

[94] T. E. Clark, P. Nimmatoori, K.-K. Lew, L. Pan, J. M. Redwing, and E. C. Dickey. Diameter Dependent Growth Rate and Interfacial Abruptness in Vapor-Liquid-Solid $Si/Si_{1-x}Ge_x$ Heterostructure Nanowires. *Nano Lett.*, 8(4):1246–1252, 2008.

[95] M. T. Bjork, B. J. Olsson, T. Sass, A. I Persson adn C. Thelander, M. H. Magnusson, K. Deppert, L. R. Wallenberg, and L. Samuelson. One-Dimentional Steeplechase for Electrons Realised. *Nano Lett.*, 2(2):87–89, 2002.

[96] Y. M. Niquet, C. Priester, and H. Mariette. influence of the inhomogeneous strain relaxation on the optical properties of etched quantum wires. *Phys. Rev. B*, 55(12):R7387–R7390, MAR 1997.

[97] M. den Hertog, M. Elouneg-Jamroz, E. Bellet-Amalric, S. Bounouar, C. Bougerol, R. Andre, Y. Genuist, J. P. Poizat, K. Kheng, and S. Tatarenko. Insertion of CdSe Quantum Dots in ZnSe Nanowire: Correlation of Structure and Chemical Characterization with Photoluminescence. *J. Appl. Phys.*, 110:034318, 2011.

[98] S. Bounouar, C. Morchutt, M. Elouneg-Jamroz, L. Besombes, R. Andre, E. Bellet-Amalric, C. Bougerol, M. Den Hertog, K. Kheng, S. Tatarenko, and J.-Ph. Poizat. Exciton-Phonon Coupling Efficiency in CdSe Quantum Dots Embedded in ZnSe Nanowires. *Phys. Rev. B*, 85:035428, 2012.

[99] J. Wang, M. S. Gudiksen, X. Duan, Y. Cui, and C. M. Lieber. Highly polarized photoluminesence and photodetection from single indium phosphide nanowires. *Science*, 293:1455–1457, Aug 2001.

[100] F. Rong and G. D. Watkins. *Phys. Rev. Lett.*, 58(1386), 1987.

[101] P. J. Dean, B. J. Fitzpatrick, and R. N. Bhargava. Optical Properties of ZnSe doped with Ag and Au. *Phys. Rev. B*, 26(4):2016–2033, AUG 1982.

[102] R. Hanbury-Brown and R. W. Twiss. Correlation between photons in two coherent beams of light. *Nature*, 177:27–29, JAN 1956.

[103] R. Brouri, A. Beveratos, J.-Ph. Poizat, and Ph. Grangier. Photon antibunching in the Fluorescence of Individual Color Centers in Diamond. *Opt. Lett.*, 25:1294–1296, 2000.

[104] L. Besombes, K. Kheng, L. marsal, and H. Mariette. Acoustic Phonon Broadening Mechanism in Single Quantum Dot Emission. *Phys. Rev. B*, 63:155307, 2001.

[105] T. M. Babinec, B. J. M. Hausmann, M. khan, Y. Zhang, J. R. Maze, P. R. Hemmer, and M. Loncar. A diamond nanowire single-photon source. *Nature Nano.*, 5:195–199, Mar 2010.

[106] P. Michler, A. Imamoglu, M. D. Mason, P. J. Carson, G. F. Strouse, and S. K. Buratto. Quantum correlation among photons from a single quantum dot at room temperature. *Nature*, 406:968–970, Aug 2000.

[107] B. Mahler, P. Spinicelli, S. Buil, X. Quelin, J. P. Hermer, and B. Dubrtret. Towards non-blinking colloidal quantum dots. *Nature Mat.*, 7:659–664, Aug 2008.

[108] F. Pisanello, L. Martiradonna, G. Lemenager, P. Spinicelli, Angela Fiore, L. Manna, J. P. Hermier, R.Cingolani, E. Giacobino, M. De Vittorio, and A. Bramati. Room temperature-dipolelike single photon source with a colloidal dot-in-rod. *Appl. Phys. Lett.*, 96(033101), 2010.

[109] G. Sallen, A. Tribu, T. Aichele, R. Andre, L. Besombes, C. Bougerol, M. Richard, S. Tatarenko, K. Kheng, and J. P. Poizat. Subnanosecond spectral diffusion of a single quantum dot in a nanowire. *Nature Photonics*, 2010.

[110] O. Zakharov, A. Rubio, X. Blase, M. L. Cohen, and S. G. Louie. *Phys. Rev. B*, 50:10780, 1994.

[111] N. Samarth, H. Luo, J. K. Furdyna, R. G. Alonso, Y. R. Lee, A. K. Ramdas, S. B. Qadri, and N. Otsuka. *Appl. Phys. Lett.*, 56:1163, 1990.

[112] C.H. Hsiao, S. J. Chang, S. C. Hung, Y. C. Cheng, B. R. Huang, S. B. Wang, B. W. Lan, and S. H. Chih. ZnSe/ZnCdSe Heterostructure Nanowires. *J. Cryst. Growth*, 312:1670–1675, 2010.

[113] J. Claudon, J. Bleuse, N. S. Malik, M. Bazin, P. Jaffrennou, N. Gregersen, C. Sauvan, P. Lalanne, and J. M. Gerard. A highly efficient single-photon source based on a quantum dot in a photonic nanowire. *Nature Photonics*, 4:174, 2010.

Résumé

Des nanofils de ZnSe catalysés avec de l'or ont été synthétisés pour la première fois sur pseudo-substrats de ZnSe déposé sur GaAs en épitaxie par jets moléculaires. La nucléation de l'or a été étudiée en détails. Des nanoparticules d'or de diamètres homogènes ont été produites. Ces nanoparticules conduisent à la création de nanofils de diamètres de l'ordre des diamètres de Bohr des excitons dans le ZnSe et dans le CdSe, soit 10nm. Les très basses densités de nanoparticules d'or obtenues permettent la croissance de nanofils de ZnSe dans un mode non-compétitif. La croissance a été étudiée en fonction de la variation de différents paramètres tels que les flux de Zn et de Se et la température. Un rapport de flux élevé de Se:Zn~4, ainsi qu'une température aux alentours de 400°C permettent l'obtention de nanofils de faible diamètre (environ 10 nm) et de bonne qualité cristalline. Les nanofils résultant de ces conditions de croissance sur ZnSe (001) s'orientent selon deux axes. La vitesse de croissance des nanofils peut être modélisée par un modèle de transfert de matière, et en particulier la diffusion d'adatomes collectés par le substrat et les facettes du nanofil vers l'interface de croissance or-ZnSe du nanofil. Il est démontré en analysant les images de RHEED que la croissance se déroule dans un mode vapeur-solide-solide (VSS), c'est à dire, avec un catalyseur Au à l'état solide. La croissance de nanofils de ZnSe dans le mode ALE (Atomic Layer Epitaxy) a été explorée et produit des nanofils orientés selon un seul axe de croissance. L'incorporation de boîtes quantiques de CdSe à été étudiée en détails par le biais de plusieurs techniques expérimentales. Il est possible d'obtenir des BQ de CdZnSe de quelques nanomètres de long, avec des hétérojonctions abruptes et contenant aux alentours de 50% de Cd. L'étude optique de ces BQ montre de fines raies excitoniques. L'émission de photons uniques a été mesurée sur la raie biexcitonique jusqu'à la température ambiante. En raison de la présence d'une émission discrète du substrat des nanofils, ceux-ci doivent être transférés sur un substrat non-luminescent pour les études optiques.

Growth of Au-catalyzed ZnSe NWs has been successfully achieved on ZnSe pseudo-substrates for the first time. Nucleation of the gold catalyst nanoparticles was studied in details. Au nanoparticles with homogeneous diameters are achieved. The nanowire diameter that results from these nanoparticles is in the range of the Bohr diameter of excitons in ZnSe and CdSe. Ultralow density achieved for Au nanoparticles makes it possible to grow nanowires in a non-competitive mode. Study of the influence of the growth parameters was done in details. A high Se:Zn~4 flux ratio and a growth temperature in the low 400°C range are found to yield the straightest NWs. Homogeneous NWs with two main orientations are obtained on (001) ZnSe. The nanowire growth rate can be modeled by a kinetic mass-transport model of impinging adatoms flowing to the nanowire growth front. A growth of NWs by ALE yields only a single NW orientation. ZnSe NW growth was identified as taking place in the VSS mode, that is, with a solid catalyst, by in-situ RHEED observations. Incorporation of CdSe QDs was studied in details with numerous experimental techniques. It is possible to obtain CdZnSe QDs with a length of a few nanometers with compositionally sharp heterojunctions and a composition in Cd of about 50%. The optical study of such NWs shows sharp excitonic lines. Single photon emission on the biexciton was measured up to room temperature. A limitation comes from the fact that the NWs must be detached from the surface to be studied due to the presence of a discrete background emission originating from the substrate.